Modeling Buoyancy-Driven Airflow in Ventilation Shafts

by

Stephen Douglas Ray

B.S., Mechanical Engineering, M.I.T. (2008)
S.M., Mechanical Engineering, M.I.T. (2010)

Submitted to the Department of Mechanical Engineering
in partial fulfillment of the requirements for the degree of

Doctor of Philosophy in Mechanical Engineering

at the

MASSACHUSETTS INSTITUTE OF TECHNOLOGY

June 2012

Author .....
Department of Mechanical Engineering
May 15, 2012

Certified by .....
Leon R. Glicksman
Professor of Building Technology and Mechanical Engineering
Thesis Supervisor

Accepted by .....
David E. Hardt
Chairman, Department Committee on Graduate Students

Modeling Buoyancy-Driven Airflow in Ventilation Shafts

by

Stephen Douglas Ray

Submitted to the Department of Mechanical Engineering
on May 21, 2012, in partial fulfillment of the
requirements for the degree of
Doctor of Philosophy in Mechanical Engineering

Abstract

Naturally ventilated buildings can significantly reduce the required energy for cooling and ventilating buildings by drawing in outdoor air using non-mechanical forces. Buoyancy-driven systems are common in naturally ventilated commercial buildings because of their reliable performance in multi-story buildings. Such systems rely on atria or ventilation shafts to provide a pathway for air to rise through the building. Although numerous modeling techniques are used to simulate naturally ventilated buildings, airflow network tools (AFNs) are most commonly used for annual simulations. These AFNs, however, assume minimal momentum within each zone, which is a reasonable approximation in large atria, but is inappropriate in smaller ventilation shafts.

This thesis improves AFNs by accounting for momentum effects within ventilation shafts. These improvements are validated by Computation Fluid Dynamics (CFD) models that haven been validated by small scale and full scale experiments. The full scale experiment provides a detailed data set of an actual atrium that can be used in further validations and demonstrates the first use of a neutrally buoyant bubble generator for flow visualization and particle image velocimetry within a buoyancy driven naturally ventilated space. Small scale experiments and CFD simulations indicate an "ejector effect" within the shaft that uses momentum from lower floors to induce flow through upper floors. In some configurations, upper floors achieve higher flow rates than lower floors.

Existing AFNs do not predict this "ejector effect" and are shown to significantly under predict flow rates through ventilation shafts by 30-40%. Momentum effects are accounted for in AFNs using empirical relationships for discharge coefficients. This approach maintains the current structure of AFNs while enhancing their ability to simulate airflow through ventilation shafts. These improvements are shown to account for the "ejector effect" and predict airflow rates that agree with CFD simulations to within 1-25%.

Thesis Supervisor: Leon R. Glicksman
Title: Professor of Building Technology and Mechanical Engineering

Acknowledgments

I am extremely grateful for the encouragement, challenges, and all other forms of guidance my adviser Professor Leon Glicksman provided me throughout this research. I would like to thank my two other committee members, Professors Les Norford and John Lienhard for their help throughout the project. I could not have completed any of the full scale experiments without the help of Professor Joseph Paradiso, Nan-Wei Gong, Jim Bales and Mike Katz. I greatly appreciate the opportunity to work so closely with an industry partner, architects, and engineers which has been made possible by Masa Fukuda. I am grateful for the funding of this work provided by Hulic Co. Ltd. and the Martin Family Society of Fellows for Sustainability. I would like to thank the Building Technology group for all the support throughout the years, specifically Bruno Bueno, Jennifer Zessin, Alejandra Menchaca-Brandan, Tea Zakula, Nick Gayeski, Stephen Samouhos, and Jaime Gagne. I have relied on the constant support of my family and deeply appreciate and love them. Lastly, my wife Allison receives more gratitude than I can express for her limitless support and encouragement. You truly are a God-given gift.

Contents

List of Figures

List of Tables

Chapter 1

Introduction

1.1 Potential of Natural Ventilation to Reduce Building Energy Use

This thesis improves numerous natural ventilation modeling techniques and uses those improved techniques to suggest design improvements to natural ventilation systems. Why consider natural ventilation? In the United States the operation of buildings accounts for 39% of the nation's energy consumption [2]. Cooling and ventilation systems compose over 30% of the end-use of energy in buildings. Fig. 1-1 shows the end-use of energy across all U.S. buildings, demonstrating that cooling and ventilation systems account for nearly one third of all U.S. building energy use. Therefore, roughly 13% of the primary energy in the United States goes towards cooling and ventilating buildings. Pure natural ventilation, drawing outdoor air into a building without the assistance of mechanical systems, has been shown to substantially reduce cooling and ventilation energy.

1.1.1 Energy Savings from Natural Ventilation

Many buildings throughout the world are cooled using pure natural ventilation. While the majority of these buildings have no other options because of financial constraints, such as homes around the world, numerous buildings in highly developed countries

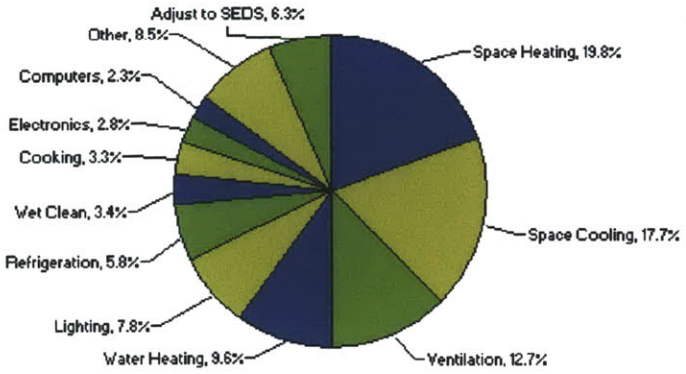

Figure 1-1: 2006 U.S. buildings energy end-use split. Source [1]

where air conditioning is an option still use pure natural ventilation. The San Francisco Federal Building uses pure natural ventilation in 70% of the building, despite U.S. restrictions that prohibit openings on lower floors, precluding the use of natural ventilation on those floors [4].

The Frederick Lanchester library at Coventry University in the United Kingdom uses a series of ventilation towers to naturally ventilate the building [19]. The four story, $10,000\ m^2$ building is on a dense inner city site and shown in Fig. 1-2. Post occupancy surveys indicate most occupants are satisfied with the comfort conditions [54]. The building has also been predicted to consume 86% less energy than similar mechanically ventilated buildings, as shown through the predicted energy use in Fig. 1-3 [19].

The San Diego Children's Museum is another example of a building with a pure natural ventilation system. San Diego's mild climate allows the main exhibition spaces to function without mechanical heating or cooling [16]. A rendering of the museum is shown in Fig. 1-4. Although this study of the museum does not report any energy savings, it can be assumed that no heating or cooling energy is required for the main exhibition spaces, which constitute a large portion of the building [16]. Fortunately, another helpful performance metric is provided - predicted indoor temperatures. Any part of the museum that is not mechanically heated or cooled must be conditioned using outdoor air, solar gains, and internal heat loads, which are more difficult to

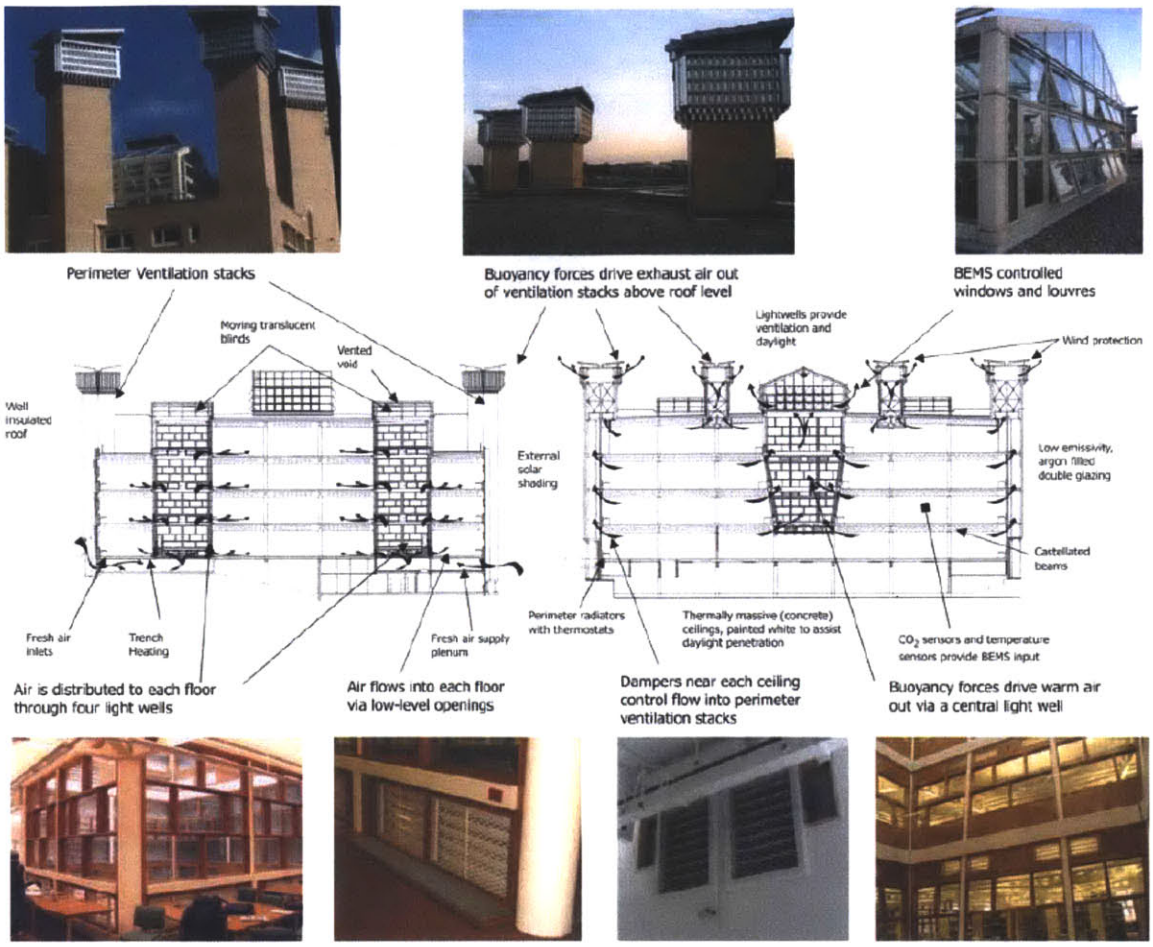

Figure 1-2: Photographs and drawings of the Frederick Lanchester library at Coventry University in the United Kingdom, which uses pure natural ventilation Source [19]

control than a mechanical system. Thus, the indoor air temperature becomes a helpful measure of how well these techniques can maintain a comfortable indoor environment. The predicted indoor temperatures for two control methods are shown in Fig. 1-5, where the BMS and user controlled option is the final recommendation of the authors [16]. Using this control method, the indoor temperature is predicted to remain below 75 $^{\circ}F$ for 72 % of the year, and not rise above 81 $^{\circ}F$ except for 7% of the year [16].

Not only do these three buildings rely on pure natural ventilation for cooling, but they are also located in very temperate climates. A fundamental limitation of pure natural ventilation is the required climate. No building owner will naturally ventilate

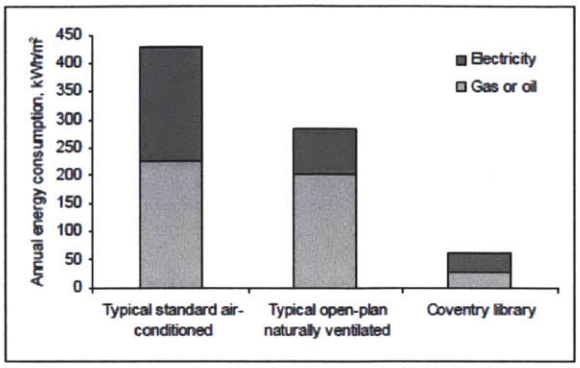

Figure 1-3: Predicted energy use of the Frederick Lanchester library at Coventry University in the United Kingdom, which shows the building saves 86% energy compared to a similar mechanically ventilated building. Source [19]

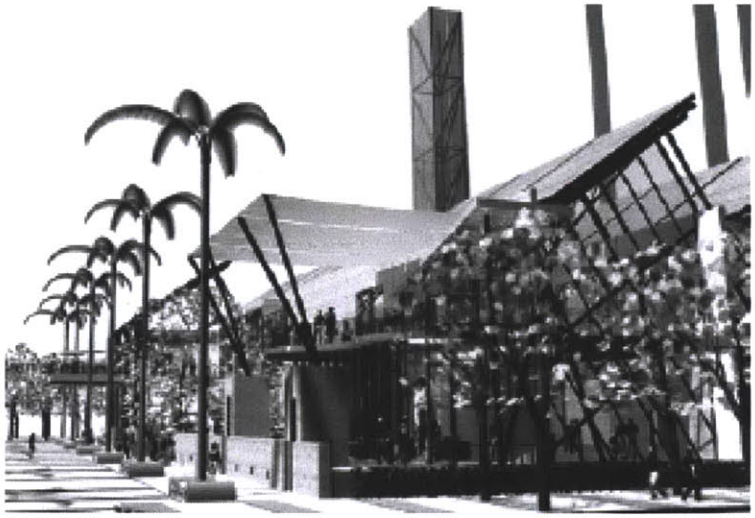

Figure 1-4: Rendering of the naturally ventilated San Diego Children's Museum in San Diego, CA that relies on no mechanical heating or cooling for the main exhibition spaces. Source [16]

Percentage of hours where T_{IN} is:	T_{IN} < 66 (F) *Cold*	66< T_{IN} <75 (F) *Good*	75< T_{IN} <81 (F) *Hot*	81< T_{IN} <86 (F) *Very hot*	T_{IN} > 86 (F) *Too hot*
BMS controlled Stack driven flow	5.8 %	56.5 %	23.7 %	12.1 %	1.9 %
BMS and USER controlled Stack and wind driven flow	6.6 %	66.0 %	20.4 %	5.2 %	1.8 %

Figure 1-5: Predicted indoor temperatures for the naturally ventilated San Diego Children's Museum indicating that temperatures above 81 F will be reached during 7% of the year. Source [16]

his building if outside air temperatures or humidity levels are unacceptable for indoor comfort conditions. Thus, a rare few climates allow for a purely naturally ventilated building. This limitation in pure natural ventilation has led to hybrid ventilation, which is a mix of natural ventilation and more traditional mechanical heating, ventilation, and air conditioning (HVAC) methods. An example of a building with hybrid ventilation is shown in Fig. 1-6. While hybrid ventilation systems predictably require a larger capital investment than either a pure natural ventilation or mechanical HVAC system, the operational cost savings of a hybrid ventilation system over its lifetime could conceivably more than pay back the initial investment. However, very few building owners will choose to invest in a hybrid ventilation system unless they are assured these cost savings will pay off the initial capital investment. Modeling techniques are essential to providing that assurance.

Hybrid ventilation systems offer the same energy saving potential of pure natural ventilation systems if the mechanical system is never used. In practice, however, hybrid systems typically consume more energy by using mechanical cooling to provide comfortable indoor conditions even when outdoor conditions prohibit a pure natural ventilation system from doing so. Some examples of hybrid ventilation buildings are

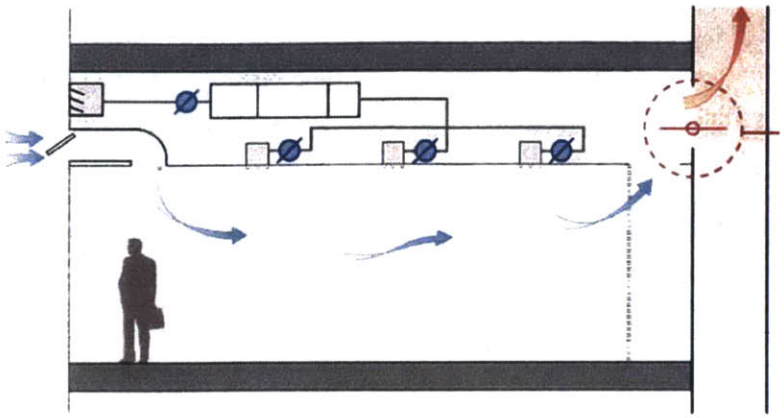

Figure 1-6: Example of a building with hybrid ventilation where the natural ventilation system and mechanical system can be used indepently or in parallel. Source [43]

given below.

A new 88,000 square feet library and faculty building for Judson College near Chicago, Illinois uses a hybrid ventilation system and is shown in Fig. 1-7. A sophisticated building monitoring system, BMS, is used to control numerous dampers, fans, and chillers to optimize the amount of non-mechanical cooling throughout the year. This hybrid ventilation design and BMS decreased the number of months in which mechanical cooling is needed from seven to three months [53]. Fig. 1-7 also shows the annual energy cost for heating, cooling, and ventilation is predicted to be 43% less than a U.S. Standard Building [53]. The extensive use of the hybrid ventilation system is illustrated in Fig. 1-8 where the various modes of operation are shown as a percentage of the total occupied hours.

Another example of a hybrid ventilation building comes from Grong, Norway. The Media School, a small one-story grade school, utilizes an underground culvert with heavy thermal mass and exhaust fans to maintain comfortable indoor conditions. The school and a section of the culvert are shown in Fig. 1-9 [59]. The school consumed a measured energy consumption of 180 kWh/m^2 $year$ compared to the Norwegian average of 198 kWh/m^2 $year$, saving 9% of total energy [59].

The Wilkinson building at the University of Sydney, shown in Fig. 1-10, provides another example of the measured energy savings of a hybrid ventilation building.

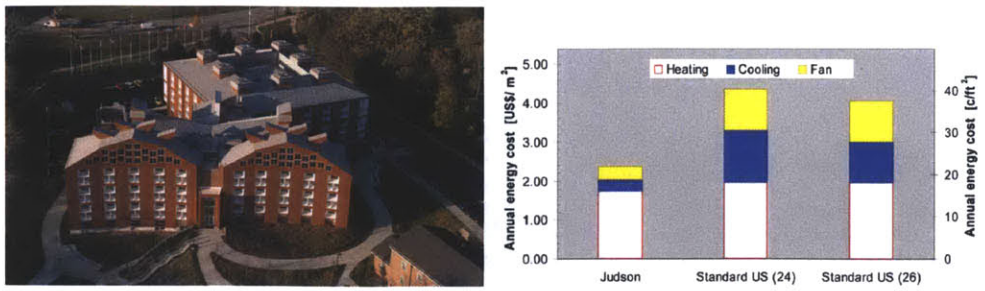

Figure 1-7: The Harm Weber Library and Academic Center at Judson University in Elgin, Illinois uses a hybrid ventilation system to save 43% cooling energy. Simulated energy usage is compared to two identical U.S. standard buildings, with a 24 $°C$ and 26 $°C$ setpoint. Source [53].

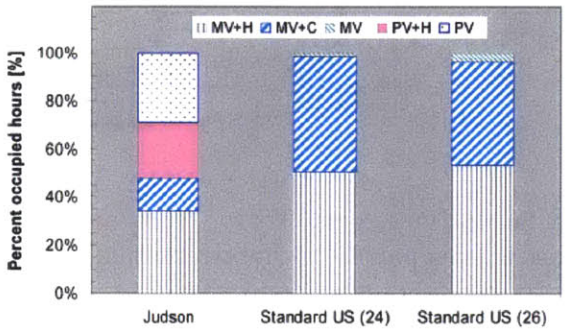

Figure 1-8: Operational modes of the Harm Weber Library and Academic Center at Judson University in Elgin, Illinois as a percentage of total occupied hours. Operational modes of a standard U.S. building with a 24 C and 26 C setpoint are also shown. $MV+H$ - mechanical ventilation and heating; $MV+C$ - mechanical ventilation and cooling; MV - mechcanical ventilaiton only; $PV+H$ passive ventilation and heating; PV - passive (or pure natural) ventilation. Source [53].

This tertiary educational facility rennovated twenty five offices with hybrid ventilation systems that use cross ventilation when appropriate [51]. Annual energy consumption for the hybrid ventilation offices has varied between 49.1 and 52.4 $kWh/yr \cdot m^2$ during four years of operation [51]. The estimated consumption of the conventional air conditioning system for the same space is 226 $kWh/yr \cdot m^2$, which suggests this hybrid ventilation system saves roughly 77% cooling and ventilation energy [51].

Despite the differences in capital investment and use of mechanical equipment, both hybrid and pure natural ventilation systems are designed to maintain comfortable indoor conditions. The enhanced modeling techniques developed in this thesis

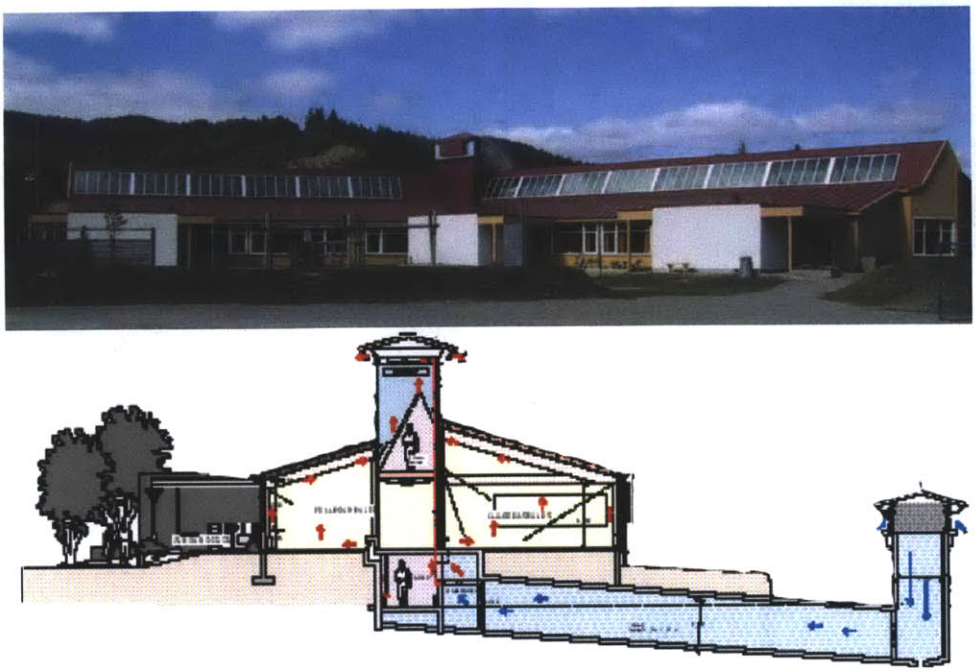

Figure 1-9: The Media School in Grong, Norway uses an underground culvert, heavy thermal mass, and exhaust fans as part of its hybrid ventilation system. Source [59].

Figure 1-10: The hybrid ventilation system in the Wilkinson building at the University of Sydney uses nearly 77% less energy than a conventional air conditiong system. Source [51].

help designers and engineers better predict these comfort conditions. Two broad approaches are typically used to define indoor comfort conditions.

1.1.2 Indoor Comfort Conditions

Quantitatively defining comfortable indoor conditions is extremely challenging. From experience, one recognizes the importance of clothing, activity level, air speed, lighting conditions, and many other factors in determining what environment is comfortable. Even if one is only interested in defining thermal comfort conditions, the task is still difficult. The American Society of Heating, Refrigerating, and Air Conditioning Engineers (ASHRAE) has attempted to define indoor thermal comfort conditions for naturally ventilated buildings with two methods in the ASHRAE Standard 55 [7].

First, ASHRAE specifies allowable indoor operative temperatures and maximum humidity levels based on the amount of occupant clothing, which has the unit *clo*. Higher *clo* values correspond to more clothing [7]. These ranges are often plotted on a pyschrometric chart, as shown in Fig. 1-11

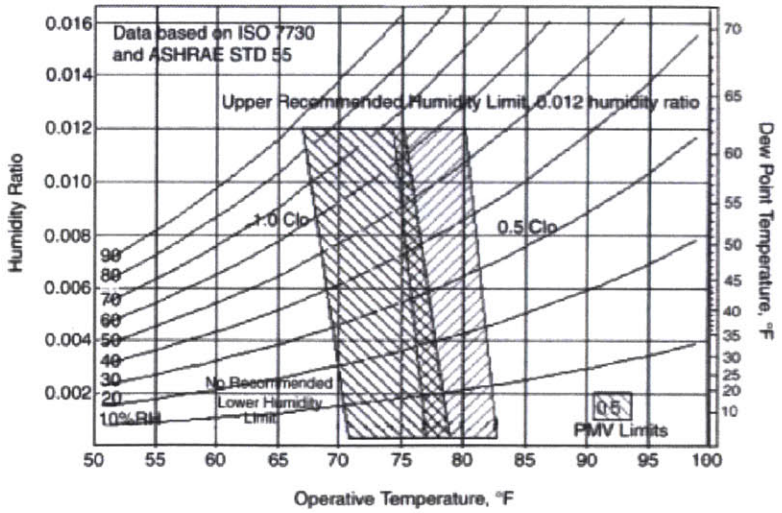

Figure 1-11: One method used by ASHRAE to quantify indoor comfort conditions is to specify a range of acceptable temperature and maximum humidity levels based on the amount of occupant clothing. Source [7]

The second method is called the 'adaptive model' because the acceptable indoor temperature range changes as outdoor conditions change. It is developed based on

the idea that comfort expectations are largely influenced by environmental norms. Someone who has spent his entire life in air conditioned buildings will likely have very high expectations for homogenious indoor conditions and cool temperatures. On the other hand, someone who has spent his entire life in purely naturally ventilated buildings will likely be comfortable in a wider range of indoor air temperatures. In an attempt to quantify this increased range of acceptable air temperatures, Brager analyzed 22,000 sets of data from 160 different buildings on four continents to develop the 'adaptive comfort model' [20]. Her model requires that the building is purely naturally ventilated, occupants can control the openings, occupants are at near sedentary activity levels, and that occupants can freely adapt their clothing throughout the year [7]. Fig. 1-12 shows the adapative range of indoor operative temperatures, or temperatures that also consider the effect of radiation, as a function of mean monthly outdoor air temperature.

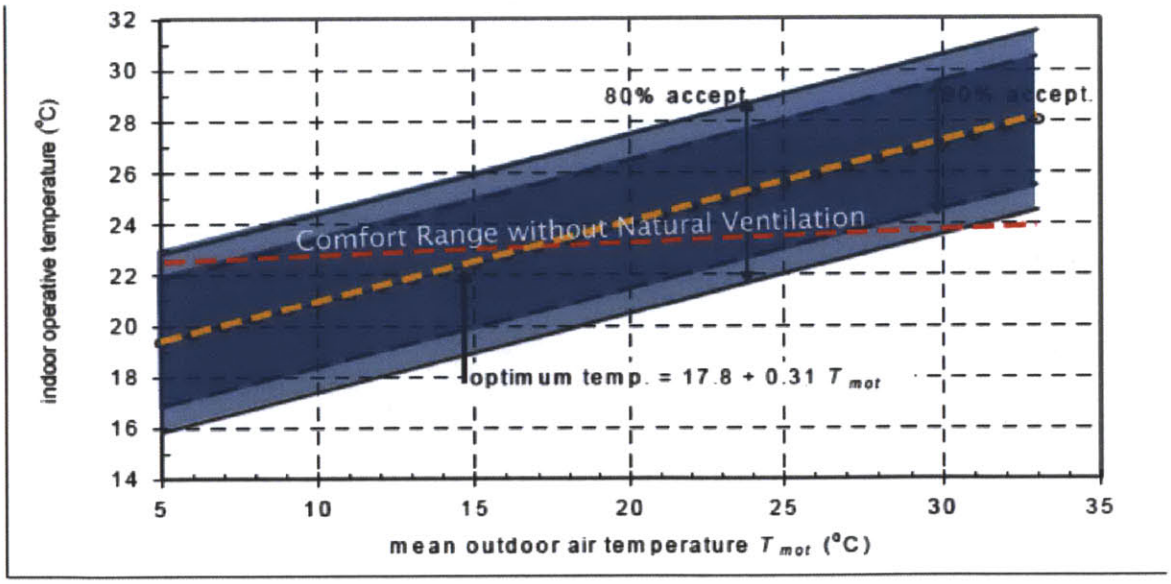

Figure 1-12: Another method used by ASHRAE to quantify indoor comfort conditions by accounting for adapting comfort requirements as outdoor temperatures increase Source [7].

Whether a pure or hybrid natural ventilation system is used, ensuring comfortable indoor conditions is essential. When natural ventilation is used, choosing the 'right' method for defining comfortable conditions can be a contenious exercise. To

provide more background on natural ventilation systems, the two driving forces are now discussed.

1.1.3 Two Driving Forces for Natural Ventilation

Natural ventilation is driven by two physical forces: wind and buoyancy differences. Wind-driven ventilation, often referred to as cross flow, results from a favorable pressure gradient across the exterior of the building that draws air through the interior space. A very common case of wind-driven ventilation is shown in Fig. 1-13 where the opening on the windward side of the building experiences a high pressure from the impingement of the incoming wind and the opening on the leeward side experiences a lower pressure in the wake of the wind. This favorable pressure gradient draws air through the windward opening and out the leeward opening, thus creating wind-driven ventilation. Higher wind speeds lead to larger pressure gradients, which result in larger ventilation rates.

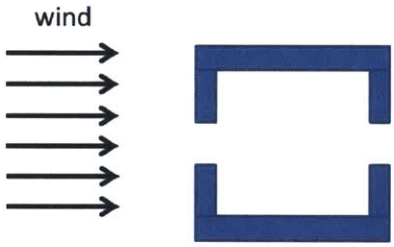

Figure 1-13: Example of wind-driven ventilation.

Wind-driven ventilation has been the subject of extensive research. Etheridge and Sandberg discuss wind-driven ventilation in depth in their book [23]. Zhai et al. reviewed ten field experiments that rely on wind-driven ventilation in addition to some lab experiments [68]. The San Francisco Federal Building, a plan of which is shown in Fig. 1-14, also relies on wind-driven ventilation. Haves et al. have studied the temperature distribution and airflow in the occupied spaces as a function of different combinations of window openings [30].

Although wind-driven ventilation has been extensively researched, a few barriers

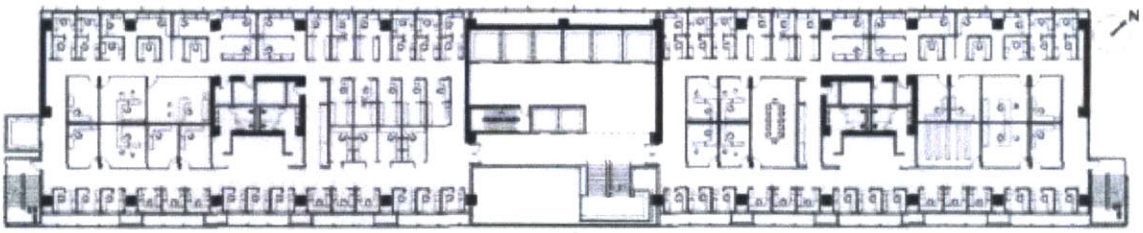

Figure 1-14: Plan view of San Francisco Federal Building. Source [30]

limit its use. First, it is highly dependent on local wind speeds and direction, both of which constantly fluctuate in the actual environment. Wind speed and direction not only fluctuate with time at a specfic location on the building surface, but often vary across the entire building surface. Furthermore, surounding obstructions such as other buildings or trees also affect local wind conditions. This variability in wind speed and direction make wind-driven ventilation extremely difficult to control.

Second, a pure wind-driven system often requires a narrow building floor plate to allow the incoming air to sufficiently offset the heat gains of the entire indoor space. Most wind-driven systems rely on inlet openings along the perimeter of the occupied space, whereas most of the heat sources are generated within the occupied space. Thus, a narrow floorplate increases the ratio of building perimeter to floor area and allows more airflow relative to the heat sources. A deep floorplate decreases this ratio, allowing more heat to be generated than can be offset by the ventilation.

Third, as more buildings are constructed in urban areas, the desireable pressure distribution across the building facade is harder to obtain. Recall Fig. 1-13 where the windward side of the building experiences a higher pressure than the leeward side, which is in the wake of the wind. Consider a building in the middle of a dense urban area, as indicated by the shaded rectangle shown in Fig. 1-15. If all the buildings are approximately the same height, as they often are in urban settings, there is lower impingement of wind on the windward side of the building under consideration and little wake on its leeward side. Thus only a small pressure difference is created resulting in little if any ventilation.

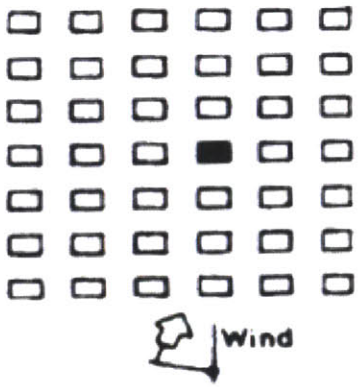

Figure 1-15: The building of interest, shaded black, has a very different wind profile in the middle of a dense urban setting than if it stood by itself. Source [23]

Buoyancy-driven ventilation results from a hydrostatic pressure gradient created by density differences. These density differences result from differing indoor and outdoor temperatures and differing elevations of the inlet and exhaust openings. Fig. 1-16 shows a simplified case of buoyancy-driven ventilation to help explain the phenomena. Assuming the indoor air is warmer than the outdoor air due to internal heat gains, consider the lower inlet and upper exhaust openings separated by a height h and uniform internal temperature. The indoor air column of height h is warmer than the outdoor column of the same height; because warm air is less dense than cool air, a smaller density gradient exists inside the building than outside. The hydrostatic pressure of air depends on the density of air, height of air in the column, and gravitational acceleration. In both indoor and outdoor columns of air, the column height and gravitational acceleration are equal. Thus, the hydrostatic pressure varies only with density. Therefore, the smaller density gradient of the indoor air column results in a smaller pressure gradient and the larger density gradient of the outdoor air column results in a larger pressure gradient. These two pressure gradients are shown next to the simplified building in Fig. 1-17. The lower opening has a higher pressure outside than inside, which draws air into the building while the upper opening has a higher pressure inside than outside, which exhausts air out of the building.

One of the major challenges of using buoyancy-driven ventilation results from the

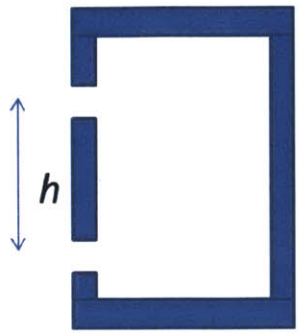

Figure 1-16: Simple example of buoyancy-driven ventilation driven through the lower inlet opening and upper exhaust opening separated by a distance h

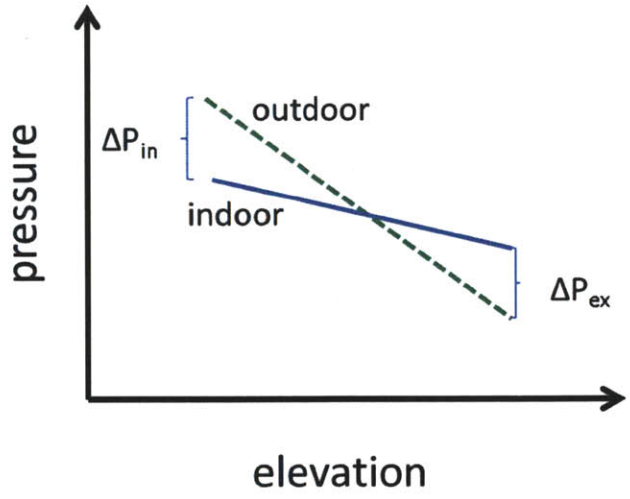

Figure 1-17: Indoor and outdoor pressure gradients as a function of elevation for simplified buoyancy-driven ventilation. The dashed green line corresponds to the outdoor air which is assumed to be warmer than the indoor air, which is represented by the solid blue line.

interplay between wind-driven and buoyancy-driven effects. If not designed properly, these two effects can oppose each other, resulting in little ventilation. Further discussion of the complication presented by both effects acting simultaneously can be found in Etheridge and Sandberg's book or Walker's dissertation [23][61]. In practice this challenge is averted by designing the building such that any wind will only enhance the buoyancy-driven ventilation. Common strategies include careful building orientation to face prevailing winds, favorable pressure gradients at the exhaust openings using walls as shown in Fig. 1-18, and large height differentials between inlet and exhaust openings to increase the stack effect.

Figure 1-18: Wind obstruction (right side) installed near the exhaust openings of a Tokyo office building to ensure any wind-driven ventilation only contributes to the buoyancy-driven ventilation.

Many of the barriers to wind-driven ventilation are avoided with buoyancy-driven ventilation. First, unlike wind-driven ventilation that relies on constantly fluctuating wind speeds and direction, buoyancy-driven ventilation depends on rather predictable temperature differences and measureable height differences. Although outdoor air temperatures fluctuate, their fluctuation is on a daily timescale, whereas wind speed and direction can flucuate by the second. Given an outdoor air temperature, the indoor air temperature can be calculated using known internal heat sources.

Second, the floorplate of a building with buoyancy-driven ventilation can often be deeper than that of a cross-ventilated building because inlet openings can be spread across the entire perimeter of the building. Unlike wind-driven ventilation, the

exhaust openings for buoyancy-driven ventilation are often at the top of the building and connected to the occupied space through an atrium or chimney. Furthermore, the hydrostatic pressure around the perimeter of a given floor is nearly uniform, allowing air to be evenly drawn into the building from all sides and exhausted through a central atrium.

An additional benefit of buoyancy-driven ventilation over wind-driven ventilation is that it only requires a temperature and height difference, whereas wind-driven ventilation requires sufficient wind. Although buoyancy-driven ventilation requires a chimney in the middle of the floor plate, it typically provides a more predictable airflow rates.

Although both wind-driven and buoyancy-driven ventilation can provide cooling and ventilation energy savings, the bulk of this dissertation focuses on buoyancy-driven ventilation because of the aforementioned advantages and application to the concurrent design work of a Tokyo office building [47][40].

1.2 Thesis Objectives

Whether a pure or hybrid natural ventilation system is used, architects and developers will not use natural ventilation unless they can predict that such systems will provide comfortable indoor conditions and pay back the initial capital cost. Pure natural ventilation systems often require less capital than mechanical systems due to their comparatively fewer system components. However, their ability to provide comfortable conditions throughout the year is a key criterion to their use. In order to predict indoor comfort conditions, numerous modeling techniques are required. Additionally, in more advanced pure natural ventilation buildings, the control systems use various modeling techniques to intelligently operate the building.

Hybrid ventilation, on the other hand, ensures the same level of comfort provided by a mechanical system because of its ability to use mechanical cooling when needed. A key criterion to using hybrid ventilation is whether the capital cost of installing both a mechanical and natural system is offset by reduced energy costs and other

incentives. Thus, modeling techniques are required to predict the reduction in energy costs before major design decisions can be made.

Current modeling techniques of naturally ventilated buildings fall into five categories: analytical/empirical, small scale, full scale, airflow network, and computational fluid dynamics (CFD). Each category has its unique advantages and limitations, which are discussed in Chapter 2. These limitations in current modeling techniques provide ample room for improvements. Analytical/empirical models are too simple to use in most real-world situations. Small scale models require careful replication of the full scale building and rely on threshold values of nondimensional numbers that are often vaguely defined and can vary with geometry. Full scale models are resource intensive and often lack sufficient measurements, particularly acurate airflow visualization. Airflow network models make simplifying assumptions that can neglect important phenomena. CFD models have been shown to accurately simulate natural ventilation systems, but generally require long run times and do not provide annual results or the energy use associated with the system.

This thesis enables designers and engineers to make more informed decisions on the expected comfort conditions and energy savings of naturally ventilated buildings by enhancing current modeling techniques. Specific contributions are summarized below. Small scale models relying on buoyancy-driven natural ventilation will more accurately model the full scale building because the threshold value of the nondimensional Grashof number is refined. Greater detail can be extracted from a full scale data set because a full scale experiment has been conducted with more detail than any published work to date. Intricate flow characteristics can now be observed using a novel flow visualization technique for in-situ flow visualization in full scale buildings. Airflow network models will better account for the significant impact of the exhaust pathway cross section. Finally, designers can incorporate natural ventilation into a wider range of buildings because an "ejector effect" has been demonstrated in exhaust shafts that increases the total airflow through naturally ventilated buildings while requiring less space for the system.

1.3 Thesis Outline

Chapter 2 describes current modeling techniques for natural ventilation. Analytical/Empirical, small scale, full scale, airflow network, and CFD models are all explained and multiple examples are provided. Opportunities for improved modeling are highlighted.

Chapter 3 presents the small scale experiments conducted in the present work. The experimental design is described, which uses a novel flow visualization technique that avoids artificial density gradients. Various CFD models are used to simulate the small scale experiment and the results from the k-ϵ model most closely match the measured results, though the k-ω model similarly predicts the measured results well.

Chapter 4 provides a deeper explanation of the theory behind small scale models and presents the current work to refine the Grashof number threshold. This threshold is essential in small scale modeling because designing a small scale model that matches the Grashof number of a full scale building is practically impossible.

Chapter 5 presents the full scale experimental work with specific attention given to the instrumentation. The same novel flow visualization technique used in the small scale experiments is also used for in-situ flow characterization and is shown to provide exceptional flow visualization. CFD simulations are further validated using results from the full scale experiment.

Chapter 6 uses the validated CFD models to explore how buoyancy-driven natural ventilation changes with various geometric parameters, especially the cross sectional area of the exhaust shaft or atrium. Multiple simulations are run and small scale experiments are used to illustrate the strong dependence of the airflow on the cross section of the exhaust shaft. This dependence is refferred to as the "ejector effect." The second half of the chapter describes how an airflow network model developed at MIT, called CoolVent, is improved to account for this ejector effect. Specific changes to the code are described and the improved CoolVent is compared to CFD models to provide validation of the improvements.

Chapter 7 summarizes the dissertation and proposes opportunities for future re-

search.

Chapter 2

Existing Natural Ventilation Modeling Strategies

The aim of this thesis is to enhance current natural ventilation modeling techniques. These enhanced techniques are then used to inform practical design decisions, particularly how smaller ventilation shafts can lead to greater airflow through buildings. Before describing these enhancements and design decisions, the current status of natural ventilation modeling techniques is outlined below. Modeling techniques are traditionally divided into five groups, each of which is discussed in this chapter: analytical and empirical models, small scale models, full scale models, airflow network models, and CFD models.

2.1 Analytical and Empirical Models

Analytical models provide one of the oldest and simplest modeling techniques by using fundamental equations of heat transfer and fluid dynamics with simplified geometries and boundary conditions to obtain a closed-form solution [46] [68]. This solution is particular to the geometry considered, but the methodology and assumptions used to derive the solution may be used for different cases [46]. Key strengths of this method include its simplicity, low cost of computing resources, and richness in physical meaning [46].

Empirical models are models created with the aid of experimentation, observation, and increasingly numerical simulation. They have been heavily used by design engineers in practice and their existence in a given field is "a symbol of maturity" for that engineering practice [46]. Some empirical models are derived from fundamental physical equations and use experimental data to determine the value of a constant. Other empirical models, though, fit a curve to experimental data and may not rely on any fundamental physics. Empirical models can be incorporated into analytical models as shown below.

A very simple analytical model can be obtained for a single-zone building at a uniform temperature with two identical openings, as shown in Fig. 2-1. Assuming indoor air velocities are very small and the absence of wind outside, Bernoulli's equation can be applied to two points outside the building at heights z_1 and z_2 and two points inside at the same elevations to yield

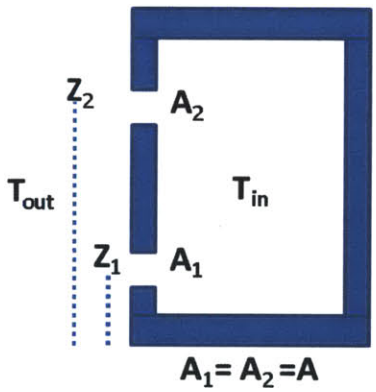

Figure 2-1: Example of simple buoyancy-driven ventilation in a single zone with two equal area windows at elevations z_1 and z_2 and a uniform indoor temperature T_{in}.

$$gz_1 + \frac{P_{1o}}{\rho_{(T_o)}} = gz_2 + \frac{P_{2o}}{\rho_{(T_o)}} \tag{2.1}$$

$$gz_1 + \frac{P_{1in}}{\rho_{(T_{in})}} = gz_2 + \frac{P_{2in}}{\rho_{(T_{in})}} \tag{2.2}$$

where g is the acceleration due to gravity in m/s^2, z is the window elevation in m, P_{in} is the indoor pressure in Pa, P_o is the outdoor pressure in Pa, and $\rho_{(T)}$ is the

density of air at T temperature in kg/m^3.

Using the ideal gas law, these two equations can be combined and solved for the driving pressure

$$(P_1 - P_2)_{out} - (P_1 - P_2)_{in} = \rho_o g(z_2 - z_1)\left(\frac{T_{in} - T_o}{T_{in}}\right) \tag{2.3}$$

This result can be combined with the orifice equation, Eq. 2.4, which is an empirical model based on the conservation of momentum, conservation of mass, and experimentally measured pressure drop through an orfice. An example experimental setup is shown in Fig. 2-2 where the static pressure is measured on both sides of the orifice in addition to the total flowrate [23]. These parameters are then used in Eq. 2.4 to determine the discharge coefficient C_D for an opening with area A.

$$\dot{V}_{orifice} = AC_D\sqrt{\frac{2\Delta P}{\rho}} \tag{2.4}$$

Much work has investigated how the discharge coeffient varies with geometry and flowrate. Fig. 2-3 provides an idea of the variation typically observed. Despite this variation, a value between 0.6 and 0.7 is typically used for sharp-edged openings and values between 0.2 and 0.8 are used for narrow openings [23].

By combining the orifice equation, Eq. 2.4, with Eq. 2.3 one can obtain the flowrate entering the building, $\dot{V}_{buoyant}$ as a function of temperature and height difference

$$\dot{V}_{buoyant} = AC_D\sqrt{\frac{g(z_2 - z_1)(T_{in} - T_o)}{T_{in}}} \tag{2.5}$$

A slightly more complicated model has been developed by Fitzgerald and Woods for a similar geometry with a uniform internal heat flux of Q_h, shown in Fig. 2-4 [24]. They have used the conservation of energy and momentum to calculate the temperature rise in the zone, ΔT_{Fitz}, and the resulting flowrate $\dot{V}_{Fitz}$ [24]. Their results are shown below for the case when the two openings are assumed to have equal areas, A, and discharge coefficients, C_D.

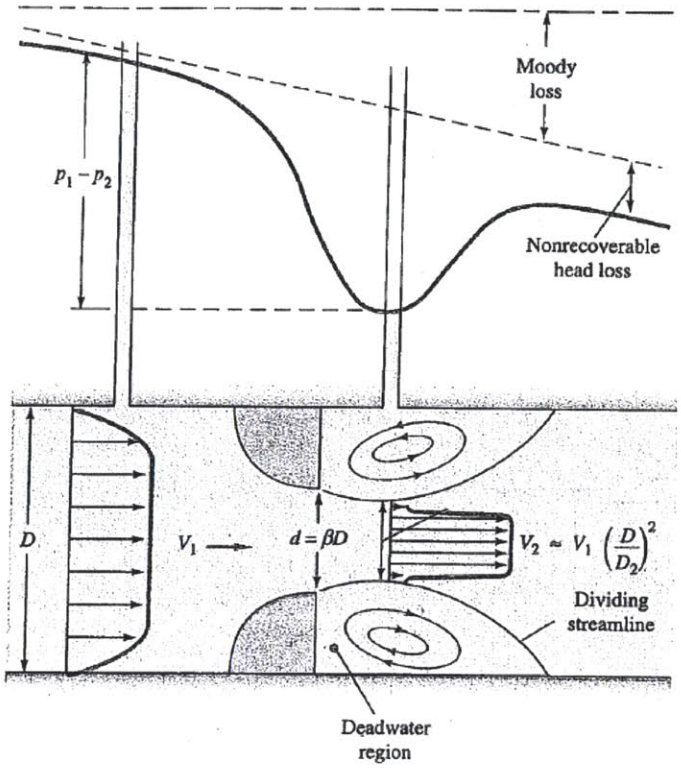

Figure 2-2: Example experimental setup to measure the discharge coeffient C_D. Source [23]

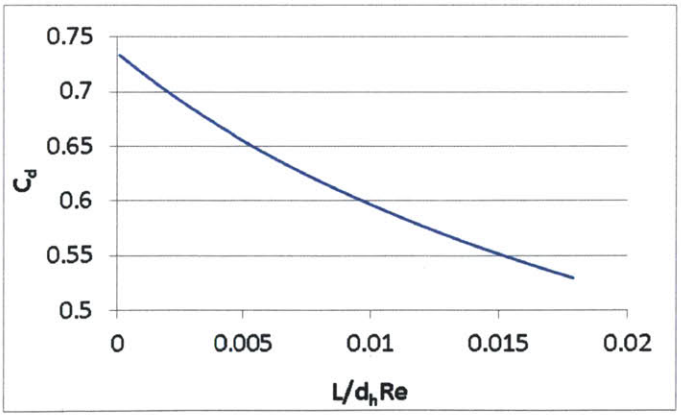

Figure 2-3: Variation in C_D of a sharp-edged inlet [23].

$$\Delta T_{Fitz} = \left[\frac{Q_h^2}{\beta\rho^2 C_p^2 A^2 C_D^2 g(z_2 - z_1)}\right]^{1/3} \tag{2.6}$$

$$\dot{V}_{Fitz} = \left[\frac{A^2 C_D^2 (z_2 - z_1) g\beta Q_h}{\rho C_p}\right]^{1/3} \tag{2.7}$$

where β is the coefficient of thermal expansion in $1/K$ and C_p is the heat capacity of air in J/kgK [24].

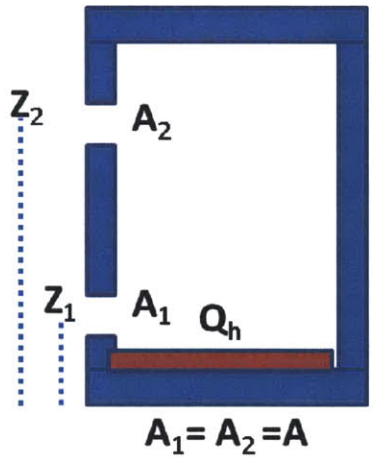

Figure 2-4: Simple geometry used in an analytical model of a single-zone building with two identical openings at elevations z_1 and z_2 with a uniform internal heat flux of Q_h.

As mentioned in the explanation of Eq. 2.4, some empircal models are derived based on underlying physical models and only use experimental data to determine a coefficient. Other empirical models, however, are created by fitting a curve to experimental data and do not rely on fundamental physical equations. A common example of such a model is the modeling of jets. Cho et al. determined jet behavior as described by velocity profiles, jet decay, and the spreading rate of jets on a surface [18]. They determined the following relationship for wall confluent jets to calculate the maximum velocity U_m

$$\left(\frac{U_m}{U_s}\right) = 2.96 l_c^{-0.79} \tag{2.8}$$

where U_s is the supply velocity in m/s, l_c is the characteristic length in m, and

the constants 2.96 and -0.79 are determined from numerical simulations [18]. Such models can provide practical design guidance, but should strictly be used in near replications of the experiments used to determine them.

Although analytical models are simple, require few computing resources, and are rich in physical meaning, they provide little utility unless a simplified geometry sufficiently describes the actual building under consideration and the many assumptions are reasonably met. Thus, while they are a strong candidate for modeling natural ventilation when they can be reasonably applied, they are often not helpful because of their extremely narrow scope of use.

Empirical models can provide a practical approach to solve well known problems within a confined scope, for example a wall confluent jet. However, they can require significant experimental work or simulations to provide a range of parameters within which the model applies. Empirical models based soley on experimental data and no underlying physics should strictly be used in near replications of the experiments used to determine them.

2.2 Small Scale Models

Small scale models have been widely used in the field of natural ventilation as a means to simulate full-scale behavior using significantly fewer resources to construct and measure airflow at a small scale, which through similarity conditions can be used to calculate full-scale behavior. Although it may not be obvious how measurements on a small scale taken from a model on one's desk can be used to calculate the airflow through a ten story building, the consideration of the governing system equations provides insight into why small scale models can be used. Both the model and full-scale building, or prototype, are governed by the same physical equations, in this case the conservation of mass, momentum, and energy. These equations can be arranged such that all variables appear as ratios where all dimensions are cancelled, so called diminsionless variables, which often creates additional dimensionless parameters. An example of a dimensionless equation is provided below. If these ratios of variables, or

dimensionless variables, and the dimensionless parameters are equal in both the model and prototype, then the equations for both cases become identical. Assuming equal boundary conditions, the solution to these equations is equal. Thus, given that the model and prototype are governed by the same physical equations, the dimensionless numbers are equated, and all boundary conditions equal, a small scale model can be used to model a full scale building.

A complete derivation of the dimensionless equations used for various types of natural ventilation can be found in chapter fourteen of Etheridge and Sandberg's book on ventilation [23]. However, to further illustrate that a small scale model can replicate a full scale building, a simple example is provided below. Consider the x-component of the Navier-Stokes equation for a two dimensional flow that neglects the force of gravity.

$$\rho\frac{\partial u}{\partial t}+\rho u\frac{\partial u}{\partial x}+\rho v\frac{\partial u}{\partial y}=-\frac{\partial P}{\partial x}+\mu\left(\frac{\partial^2 u}{\partial x^2}+\frac{\partial^2 u}{\partial y^2}\right) \tag{2.9}$$

Now, the five variables are rearranged such that they become ratios where all dimensions cancel out, i.e., dimensionless variables.

$$\bar{u}=\frac{u}{u_{char}};\bar{v}=\frac{v}{u_{char}};\bar{x}=\frac{x}{L_{char}};\bar{y}=\frac{y}{L};\bar{t}=\frac{tu_{char}}{L_{char}};\bar{P}=\frac{P}{\rho u_{char}^2} \tag{2.10}$$

Plugging these variables into Eq. 2.9 and collecting all the terms yields

$$\frac{\partial\bar{u}}{\partial\bar{t}}+\bar{u}\frac{\partial\bar{u}}{\partial\bar{x}}+\bar{v}\frac{\partial\bar{u}}{\partial\bar{y}}=-\frac{\partial\bar{P}}{\partial\bar{x}}+\frac{\mu}{\rho u_{char}L_{char}}\left(\frac{\partial^2\bar{u}}{\partial\bar{x}^2}+\frac{\partial^2\bar{u}}{\partial\bar{y}^2}\right) \tag{2.11}$$

with a single dimensionless parameter, $\frac{\mu}{\rho u_{char}L_{char}}$, or the inverse of Reynolds number. As long as all boundary conditions remain constant, the solution to Eq. 2.11 will not change provided that the ratios of the variables and dimensionless parameter also remain constant.

This example can be used to model forced flow where no heat transfer is of interest, since only the Navier-Stokes equation is used. As demonstrated, the only relevant dimensionless parameter for this case is the Reynolds number. The derivations of dimensionless equations for other types of ventilation yield additional dimensionless

parameters that, in theory, must be equal between the model and prototype and are summarized in Table 2.1. In practice, however, it will be shown that matching all of these numbers at the same time is practically impossible.

For forced flow with the considersation of heat transfer, both the Reynolds number, Re, and Prandtl number, Pr, should be equal. The Reynolds number provides a ratio of inertial forces to viscous forces. So high Re flows are often approximated as non-viscous because the inertial terms dominate. The Pr provides a ratio of momentum diffusivity to thermal diffusivity. Alternatively the Peclet number, Pe, can be used in place of the Prandtl number. The Prandtl number is defined as

$$Pr = \frac{C_p \mu}{k} \tag{2.12}$$

where k is the thermal conductivity of the fluid in $[W/mk]$. The Peclet number is simply the product of the Reynolds and Prandtl number. For buoyancy dominated flow where wind-driven flow is negligible, the Grashof number, Gr, and Prandtl number should be equal between the model and prototype. Alternatively, the Rayleigh number, Ra, which is the product of both the Grashof and Prandtl numbers, can be used in place of the Prandtl number. The Grashof number is defined as

$$Gr = \frac{g\beta\Delta T L_{char}^3}{\nu^2} \tag{2.13}$$

where ν is the kinematic viscosity $[m^2/s]$. As the Reynolds number compares inertial to viscous terms, the Grashof number compares buoyancy to viscous forces. Consequently, $Re^2 \simeq Gr$ if the buoyant velocity, Eq. 2.14, is used as u_{char} in the Re number [61][62].

$$u_b = \sqrt{g\beta L_{char}\Delta T} \tag{2.14}$$

Lastly, when both buoyancy-driven and wind-driven effects are important, the Archimedes number, Ar, and Prandtl number must be equal between the two cases. The Archimedes number provides a ratio between buoyancy and inertial terms and is defined as

Table 2.1: Dimensionless parameters required for similtude for various types of natural ventilation

Ventilation conditions	Relevant dimensionless parameters
Forced flow without heat transfer	Re
Forced flow with heat transfer	Re and Pr or Pe
Buoyancy dominated	Gr and Pr or Ra
Buoyancy and wind driven	Ar and Pr

$$Ar = \frac{g\beta\Delta T L_{char}}{u_{char}^2} \tag{2.15}$$

A well known method for determining a non-unique set of dimensionless parameters was proposed by Edgar Buckingham in 1914 and is referred to as the Buckingham Pi Theorem [13]. It states that for a physically meaningful equation

$$f(x_1, x_2, ..., x_n) = 0 \tag{2.16}$$

where x_i are n physical varilables expressed in k independent physical units, Eq. 2.16 can be rewritten as

$$F(\pi_1, \pi_2, ..., \pi_p) = 0 \tag{2.17}$$

where π_i are dimensionless parameters constructed from the physical parameters using $p = n - k$ equations of the form

$$\pi_i = q_1^{a_1} q_2^{a_2} ... = q_n^{a_n} \tag{2.18}$$

where the exponents a_i are rational numbers. An enormous limitation of the Buckingham Pi Theorem is that it provids no relationship between dimensionless parameters – it only identifies them. Thus, the previously demonstrated method of non-dimensionalizing the fundamental equations is a more physically meaningful approach.

Selected examples of more contemorary studies that use small scale models in the

design and evaluation of naturally ventilated buildings are presented below. Nyuk Hien Wong used a 1:5 scale model of an apartment in Singapore to validate numerical simulations which are used to investigate the impact of an active stack, or mechanical fans added to the vantilation chimney, on airflow rates and velocity distributions [65]. His physical model is shown in Fig. 2-5.

Figure 2-5: Small scale model of an apartment in Singapore used by Wong et al. to investigate the impact of installing a fan in the ventilation chimney [65].

Nielsen used a 1:10 scale model to aide the design of the 1992 World Exhibition in Seville [44]. He recognizes, "If, for instance, the scale is reduced by a factor of 10, then the velocity has to be increased by a factor of 10 due to the Reynolds number, which will give an increase in the temperature difference by a factor of 1000 in order to keep the Archimedes numbers" [44]. Nielsen's observation is made from simply inspecting the Reynolds and Archimedes numbers.

$$\left[\frac{\rho u_{char} L_{char}}{\mu}\right]_{prototype} = \left[\frac{\rho u_{char} L_{char}}{\mu}\right]_{model} \tag{2.19}$$

If $L_{char,model}$ decreases by a factor of 10, $u_{char,model}$ must increase by a factor of 10 in order for both Reynolds numbers to be equal. If these changes are carried over to the Archimedes number, the ΔT_{model} must increase by 1000 times to maintain

equality. Clearly such a criteria is unreasonable for any realistic prototype ΔT.

$$\left[\frac{g\beta\Delta T L_{char}}{u_{char}^2}\right]_{prototype} = \left[\frac{g\beta\Delta T L_{char}}{u_{char}^2}\right]_{model} \tag{2.20}$$

In order to derive meaningful results from the small scale model, he states the Reynolds number for the prototype and model do not need to be equal "if the Reynolds number is high and the flow pattern is governed mainly by fully developed turbulence. It is possible to ignore the Reynolds number and the Prandtl number at a sufficiently high level of velocity because the structure of the turbulence and the flow pattern will be similar" [44].

This idea of a Reynolds number threshold is commonly used in small scale modeling of ventilation. Etheridge and Sandberg propose a threshold of $2X10^3$, above which the impact of the Reynolds number on the ability of the model to predict the behavior of the prototype is very small [23]. Rolloos also relies on this threshold and references a threshold of $3X10^4$ for a circular air inlet opening [49]. However, he warns "Because of the variety in air supply conditions and geometries, in the author's opinion a fixed value of Re above which the flow will be Re-independent cannot be given" [49]. While Rolloos' point is well taken and a fixed value should not be considered the absolutle transition point between Re-dependence and Re-independence, there is a high probability of similarity between flows with Re greatly exceeding these proposed threshold values. If the flows under consideration are near the treshold values, care should be taken to ensure Re-independence.

This same principle of a dimensionless parameter threshold has been applied to buoyancy-driven flows, where the Gr is the dimensionless parameter under consideration. Given the previously mentioned relationship $Gr \simeq Re^2$, one may expect the Gr threshold in the range of $10^6 - 10^8$, or the square of the Re threshold. If both model and prototype use air as the working fluid, which is preferred to water because it is not opaque to IR radiation, equality of Gr requires

$$\left[\frac{\Delta T_{char}}{T_{char}}\right]_m L_{char,m}^3 = \left[\frac{\Delta T_{char}}{T_{char}}\right]_p L_{char,p}^3 \tag{2.21}$$

thus a relatively large model with a scale factor of three requires $\Delta T_{char,m} = 27 \cdot \Delta T_{char,p}$, which is not only difficult to acheive experimentally, but perhaps more importantly voids the Boussinesq approximation [23].

One approach to solving this dilemma is to use a different working fluid in the model, such as water. Many small scale experiments at the University of Cambridge are performed in this way, an example of which is work by Chenvidyakarn and Woods [17]. A drawback of this approach, however is that water is opaque to infrared radiation, an essential means of energy transfer in buildings. Menchaca has demonstrated this severe limitation of small scale water models more thoroughly [39].

Assuming air is used in the model, a Gr threshold is essentially required for any kind of practical model and is commonly used. Ding et al. used a threshold value to evaluate the natural ventilation performance of an eight story office building with a double facade and solar chimney [21]. A drawing of their prototype and picture of their 1:25 scale model are shown in Fig. 2-6

Ding et al. noted the impossibility of matching Gr numbers for a 1:25 scale model and mention the idea of a Gr number threshold. Unfortunately, their justification that their experiment falls above this threshold is lacking, as they state, "For natural ventilated space, most of the flow region can be regarded as such state [above the Gr threshold]" [21]. Liu et al. offer improved justification in their use of small scale modeling of the buoyancy-driven ventilation in the Center for Education in the Green Building, Taiwan [36]. They similarly use air and note the same challenge of matching Gr numbers between the Center for Education and their 1:20 scale model, both of which are shown in Fig. 2-7 [36].

They do not mention a fixed value for a Gr threshold, but state "... as long as the turbulent intensity of the flow is over some value of the Grashof number, the basic characteristic of the flow becomes independent of the Grashof number" [36]. They do refer to Etheridge and Sandberg's discussion of scale modeling as having influenced their methodology [36]. Although they don't state a specific threshold, they assume their Gr number of $3.23X10^{12}$ is sufficiently large [36].

Walker similarly refers to Etheridge and Sandberg in her modeling the Houghton

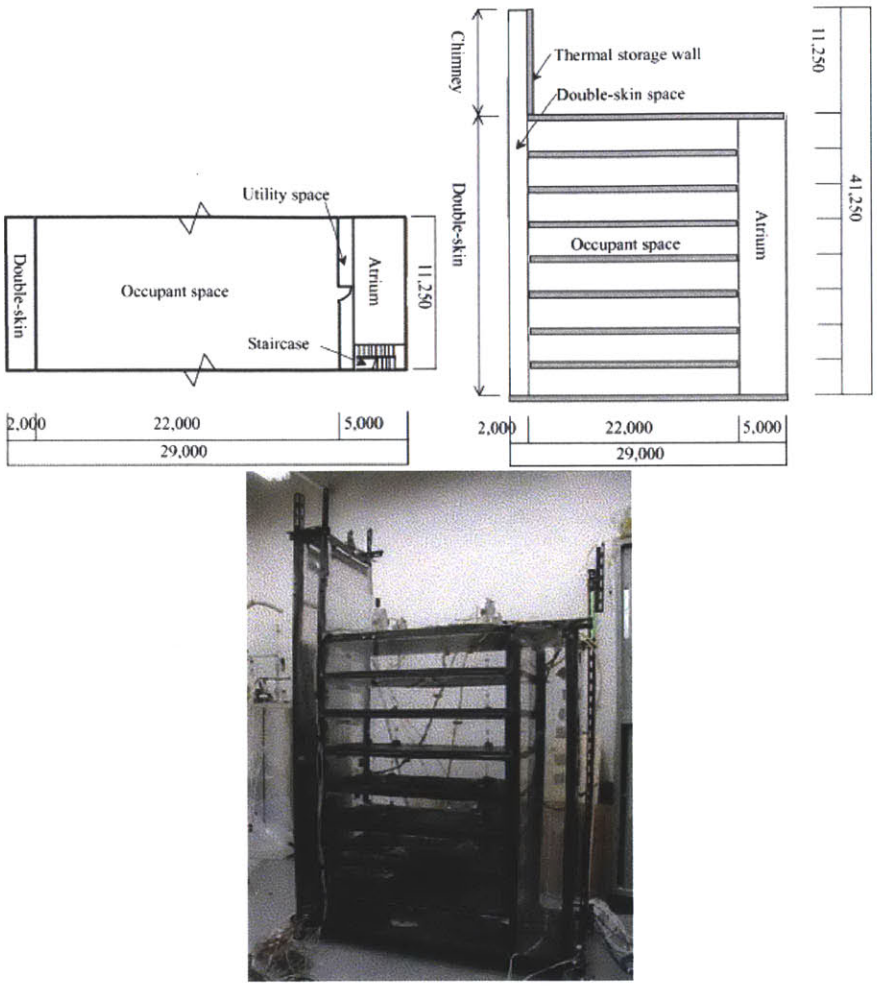

Figure 2-6: Prototype drawing of eight story office building evaluated using a 1:25 scale model, which is also shown. [21]

Building, a three story office building in Luton, UK [61] [62]. A photograph, plan view, and section view of the prototype building are provided in Fig. 2-8.

She used a 1:12 scale model, shown in Fig. 2-9, to investigate numerous aspects of performance including temperature distributions, airflow patterns, flow rates, and how these metrics change with various operating conditions [61]. A chief aim of her work was to develop a methodology for using small-scale models with air as the working fluid to evaluate the natural ventilation potential of a building [61]. Her work is regularly cited, in fact Liu et al. references her work, as an effective evaluation tool [36].

In her dissertation, Walker includes a lengthy discussion of the derivation of sim-

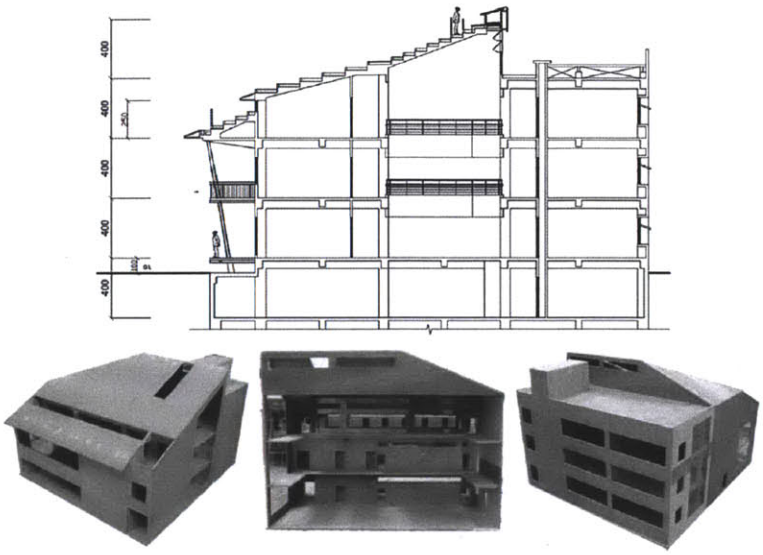

Figure 2-7: Prototype drawing of the Center for Education in the Green Building, Taiwan, which is evaluated using a 1:20 scale model, which is also shown. [36]

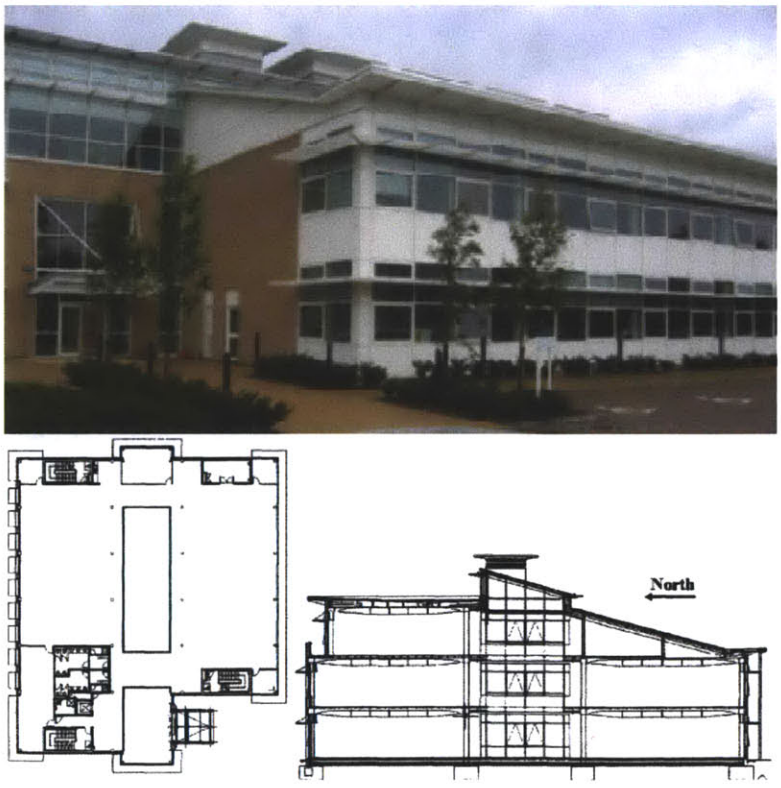

Figure 2-8: Photograph of the Houghton Building, a three story office building in Luton, UK, with plan and section drawings. [61]

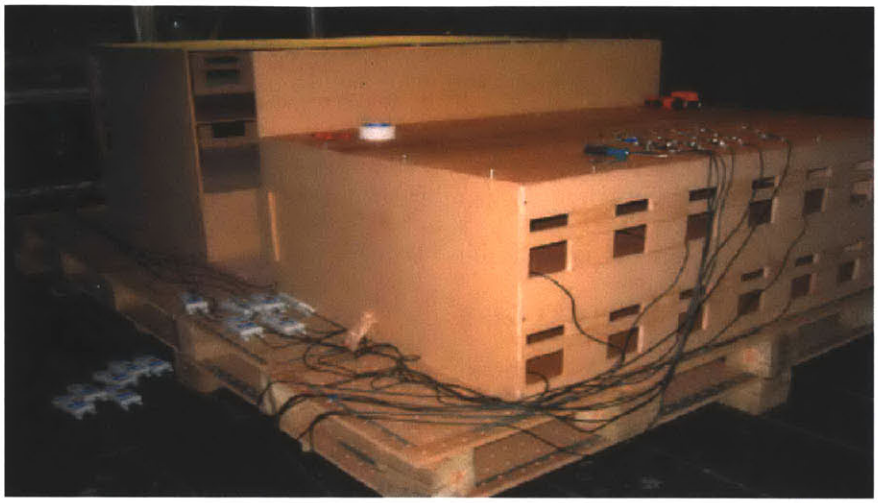

Figure 2-9: Photograph of the 1:12 scale model used by Walker to evaluate the ventilaiton of the Houghton Building, a three story office building in Luton, UK [62].

ilarity conditions, the challenge of equating Gr numbers for prototype and air-based models, and a Gr threshold referenced from Etheridge and Sandberg [61]. Speaking of Etheridge and Sandberg, Walker writes, "They propose a critical value of Grashof number in the range of 10^6 to 10^9 based on some experimental work, and using the height of a room as the characteristic length" [61]. Upon closer investigation, Etheridge and Sandberg appear to propose these values with more caution. Etheridge and Sandberg add the cautionary note to this range by stating "The origins of the above range of values are obscure, and in the absence of experimental data appropriate to the case under consideration it is probably wise to aim for the higher value" [23]. Although this range of values for the Gr threshold has been used as an absolute range, it appears Etheridge and Sandberg join Rollos in their hesitation to make such a generalization.

One of the sources cited by Etheridge and Sandberg as evidence for this range also raises suspicion of an absolute range. In it, Baturin uses a 1/20 scale model and the a full scale forge at the Leningrad Institute of Labor Protection to explore a Gr threshold [11]. The experiment seems poorly controlled given the wide range of heater power supplied to the full scale room, $4.9 - 6.2\ Mkal/hr$, resulting in a temperature rise ranging from $9.9 - 13.7\ ^{\circ}C$, although an average value of $11\ ^{\circ}C$ is used for all

calculations. Furthermore, the temperature rise of the model is maintained at 11.3 $^{\circ}C$ by varying the power input to the model heater. This lack of control of boundary conditions is concerning. Baturin's conclusions seem to further simplify his analysis. "For simulation of natural ventilation arising from density difference between columns of outdoor and internal air, it is sufficient to observe geometrical similarity (of the building and sources of heat), and to work in the range of $2X10^7 < GrPr < 10^{13}$ [or assuming $Pr = 0.7$ for air, $2.8X10^7$ becomes the lower bound], which automatically ensures similarity of the convection pattern" [11]. It is not clear why an upper bound for the Gr threshold is proposed. Furthermore, the statement that these criteria "automatically ensures similarity of the convection pattern" seems to over simplify reality and the complexities observed by many others [11].

These suspicious origins of a Gr threshold between 10^6 to 10^9 and independent proposals by both Etheridge and Sandberg and Rollos to not rely on an absolute Gr threshold suggest more work is necessary in this area. Etheridge and Sandberg propose that the upper limit of their range should be acceptable even in the absence of experimental verification for the particular geometry under consideration [23]. Is a Gr number equal to 10^9 a sufficiently high value to ensure similtude?

2.3 Full Scale Models

Full scale models are actual-size replications of the prototype building or feature of a building, for example a single floor attached to a ventilation chimney. They can provide a rich insight into the phenomena of air flow, particularly to the complexities that arise when very few, if any, simplifying assumptions are imposed. Full scale models avoid many of the issues presented by small scale models because the model is a full scale replication of the prototype, or in some cases the prototype itself. While full scale models are ideal for these reasons, they are rarely used for practical reasons. Namely, they are very resource intensive. Constructing an entire building as a model is usually outside the budget and timeline of almost all investigators. If an existing building can be used, its instrumentation is expensive and any data must be

collected while the building is in use by occupants whose first priority is often not an experimental investigation into the airflow in their building.

Despite these challenges, full scale models have been used to investigate buoyancy-driven natural ventilation. Some of these models are created for a specific feature of the building. Ray et al. used a full scale replication of the inlet assembly, shown in Fig. 2-10, to measure the associated sound attenuation and pressure loss [47].

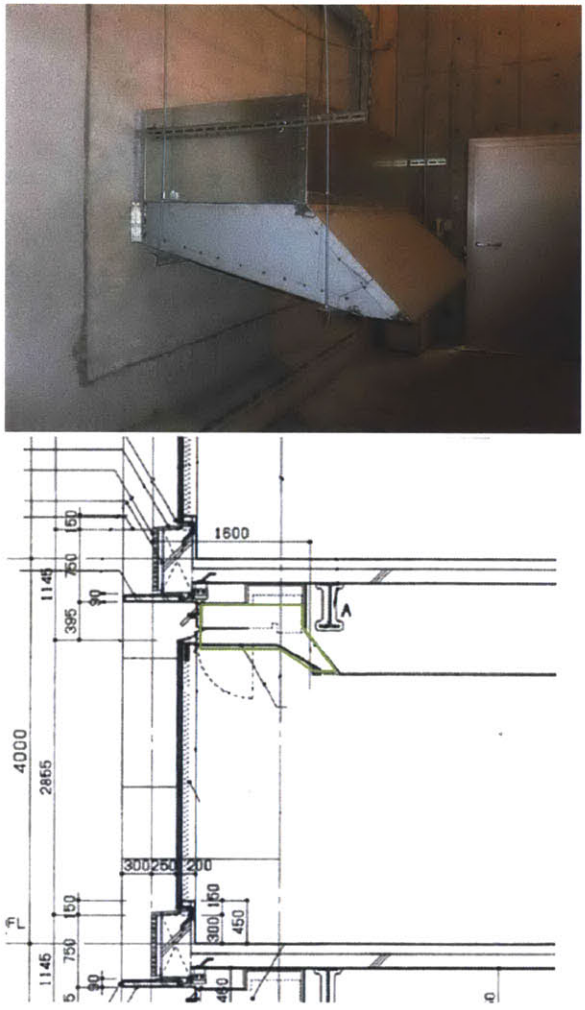

Figure 2-10: Section of inlet assembly modeled with full scale modeling techniques and full scale replication of the assembly [47].

The full scale tests were performed in a testing facility and required minimal capital given the large existing infrastructure. Additionally, the controlled tests provided helpful information that is largely unaffected by the complexities of the actual

building. For example, the sound attentuation of the system is highly dependent on frequency, but very loosely dependent on other uncontrolled parameters in the experiment like humidity or local wind direction. Some results from their testing is shown in Fig. 2-11.

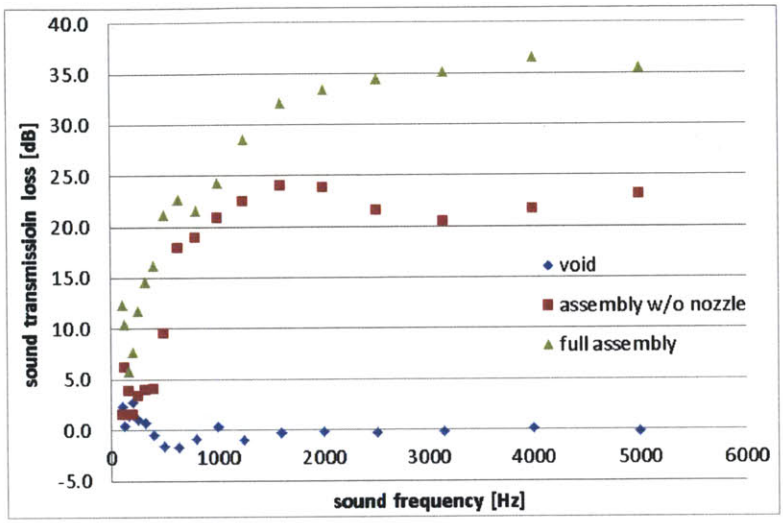

Figure 2-11: Sound attenuation as a function of frequency measured in the full scale testing of an inlet assembly used in a buoyancy-driven natural ventilation building in Tokyo [47].

Rundle et al. observed the airflow through a stairwell in the Engineering Building at Concordia University shown in Fig. 2-12 [52][41]. The stairwell is connected to each floor of the building through a hallway and conditioned using mechanical cooling that relies on inlet and exhaust vents inside the stairwell [52]. To account for the mechanical cooling, the researchers measured the volume flow rate and temperature of air at the vents [52]. Although taken at full scale, this data set is quite limited. Nine thermocouple locations measure the temperature distribution in the entire stairwell and no flow visualization technique is used [52]. Furthermore, boundary conditions are not carefully measured as indicated by their estimation of the incoming solar radiation through glazing and decision to not account for airflow rates from each floor into the stairwell [52].

Takemasa et al. isolated a small area of an entire floor to observe how air enters the building [58]. Specifically, they were interested in observing whether or not incoming air attaches to the ceiling or quickly falls on occupants near the window, shown in

Figure 2-12: Stairwell used for full scale experiment in the Engineering Building at Concordia University [52].

Fig. 2-13.

They used a smoke machine to visualize the airflow at different inlet opening angles, some of which are shown in Fig. 2-14. Based on these observations, they concluded "that outside air entering an open window tends to flow along the ceiling due to the Coanda effect and tends to not generate cold draughts in the occupied zone" [58].

However, Takemasa et al. did not account for the buoyancy differences created by their smoke visualization technique. Thus, one can not be sure if the incoming air attaches to the ceiling purely because of the Coanda effect. The positive buoyancy created by the smoke, which will not exist in the actual case, may have also contributed to the air rising to the ceiling. Walker discussed this limitation in her

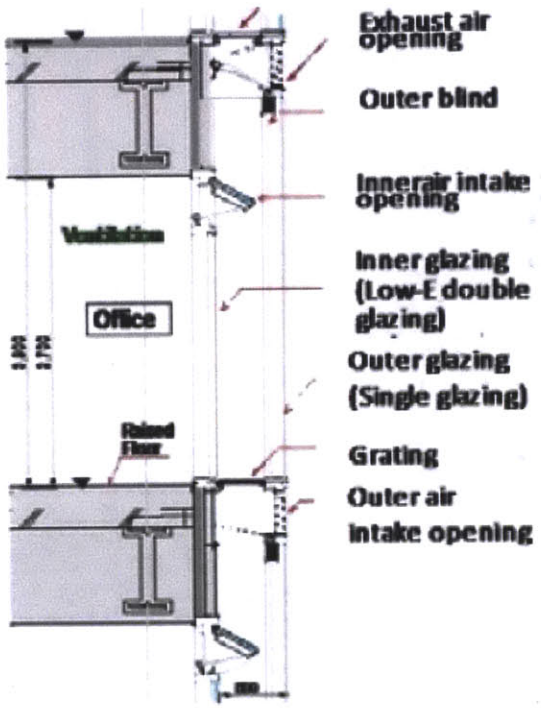

Figure 2-13: Section of facade system modeled with full scale modeling techniques. [58].

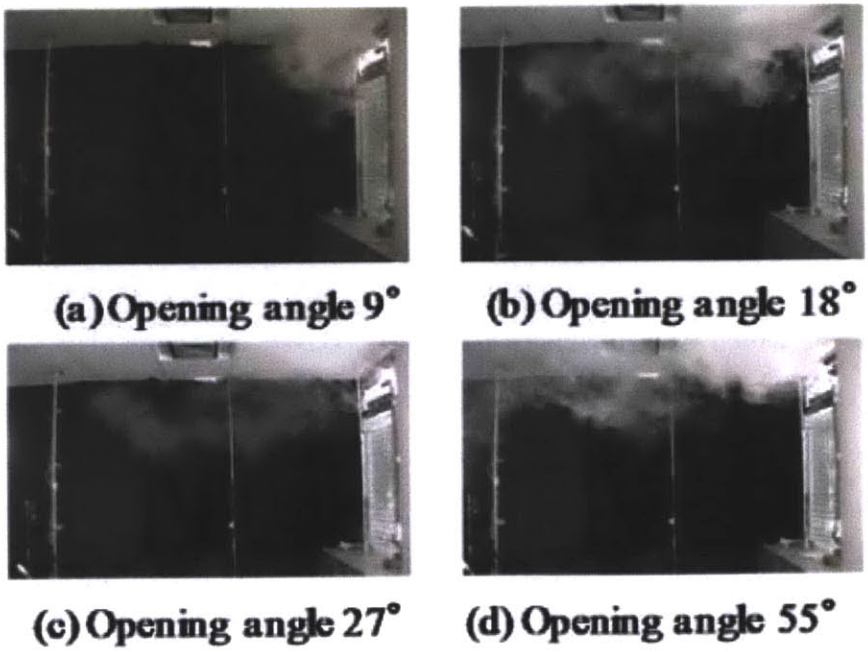

Figure 2-14: Smoke visualization of incoming air through various inlet opening angles. [58].

dissertation and proposed techniques to minimize its impact [61].

Walker also conducts full scale testing using the occupied prototype building in Luton, UK and shown in Fig. 2-8 [61]. The three story, 2,600 m^2 open plan office building relies on a central atrium to promote buoyancy-driven flow and windows on both the north and south facade to promote cross ventilation [61]. The atrium is exhausted by five ventilation stacks that can use low-powered fans to assist if needed.

Walker monitored the building for eighteen months by measuring internal temperature, indoor relative humidity, energy consumption by sub-section, and external weather conditions [61]. An extensive description of her measuring technique is provided in her dissertation. Her work presents some of the most complete full scale measurements in the literature. She also collected various short-term measurements including airflow rates measured with hotwire anemometers, CO_2 concetration, and using a homemade ventilation measurement technique incorporating a large plastic bag [61]. Some of these airflow measurements were fairly inaccurate and led to errors of 25% in the mass balance [61]. She employed a novel method of flow visualization using helium-filled balloons with small weights attached to create approximately neutrally buoyant balloons that would follow airflow patterns [61]. Although this technique provided some visualization of large-scale flow structures within the building, the inertia of the balloons and weights prevented them from tracking smaller flow structures. She also used smoke pencils, but does not mention any control for the positive buoyancy of the smoke [61]. The scale of her observed airflow patterns is shown in Fig. 2-15 where she has sketched the patterns onto a section drawing of the building.

While Walker provides a fairly complete set of full scale measurements, only four temperature sensors were used in the atrium. Such sparse measurements can not provide a detailed temperature distribution within the atrium. Furthermore, her airflow visualization techniques can be improved to more accurately account for the smaller airflow structures without having to introduce artificial density gradients from smoke pencils.

Zhai et al. has conducted an extensive literature review on the published full scale

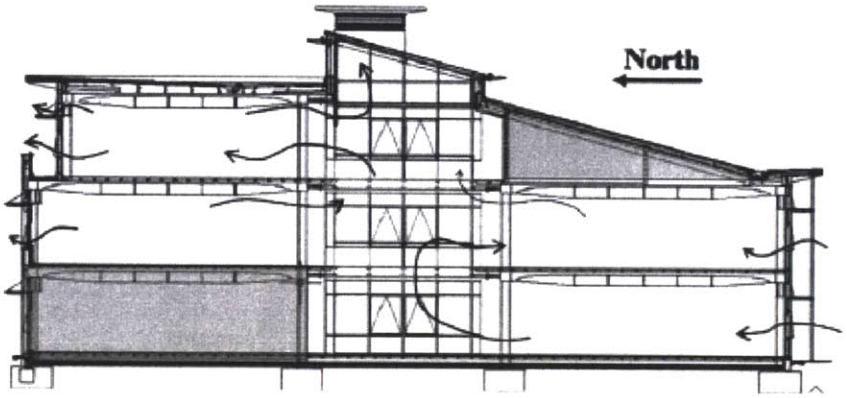

Figure 2-15: Sketches of airflow patterns observed by Walker in Houghton Hall using smoke pencils and helium-filled balloons [61].

data sets for naturally ventilated buildings [68]. His summary of published reports and their accompanying measurements are shown in Fig. 2-16. From this data, he chooses only three data sets that are complete enough to be helpful in the validation of airflow network models: The Renson Building in Belgium, Houghton Hall in the UK, and the Bang and Olufsen Building in Denmark [68]. Apart from the aformentioned flow visualization technique used by Walker at Houghton Hall, no airflow visualization techniques are used in the buildings. Furthermore, Zhai concludes "A more complete dataset including airflow measurement, as described in the final section of this report, is needed in order to eliminate this uncertainty" [68].

Full scale modeling can be advanced by the publication of a more complete data set, which includes a higher resolution of measurements within an atrium and airflow measurements. Furthermore, a new air visualization technique is needed that doesn't introduce artificial density gradients.

Building	Publication	Weather Data Source		Inter zone	Intra zone	Fan-Assisted	Wind-driven	Stack-driven	Single-Sided	Cross	Measurements			
		Weather Station	Measured On-Site								Pressure	Temp	Vel	ACH
Coventry Library, UK	Krauss (2007)	X		X				X				X	X	
Renson Bldg, Belgium	Breesch (2006)	X		X			X	X		X		X		X
Office bldg, Germany	Eicker (2006)		X	X		X	X	X	X			X		X
Houghton Hall, UK	Walker (2006)		X	X			X	X		X		X	X	X
Residence, Greece	Koinakis (2005a)	X		X			X	X	X	X				X
Apartment, Greece	Koinakis (2005b)	?	?									X		
Apartment, Greece	Niachou (2005)	?	?	X		X	X			X				X
DB Netz AG, Germany	Pfafferott (2004)	X		X			X			X		X		X
Fraunhoffer ISE, Germany	Pfafferott (2003)		X									X		X
	HybVent (2002)													
Tanga School, Sweden	Blomsterberg (2005)		X	X		X	X	X				X	X	
Media School, Norway	Wachenfeldt (2003)		X	X		X	X	X				X		
Bang & Olufsen, Denmark	Hendricksen (2002)		X	X		X	X			X		X	X	
	NatVent (1998)		X	X		X	X	X		X	X	X	X	X

Figure 2-16: Summary of full scale natural ventilation field experiments and their configurations as reviewed by Zhai et al. [68].

2.4 Airflow Network Models

Airflow network models have become an increasingly popular method for predicting airflow rates, indoor temperatures, and energy demand in naturally ventilated buildings. A brief description of airflow network models is provided below, with a focus on their limiting assumptions, and a few example models are provided. Axley provides a a more detailed history and discussion of the theory behind airflow network modeling in buildings [10].

The typical model divides a building into various zones or nodes to create a network. Connections between each node are specified based on the building design. Flow rates between connected nodes are typically calculated using a power-law function of the form

$$F_{ij} = C_{ij} A_{ij} \left| \frac{\Delta P_{ij}}{\rho} \right|^{n_{ij}} \tag{2.22}$$

where the flowrate F between zones i and j is a function of the pressure drop ΔP across the zones raised to the flow exponent n, the cross sectional area A connecting

them, and the flow coefficient C of the path. Mass conservation is satisfied for each node such that

$$\sum_j F_{ji} = 0 \tag{2.23}$$

An energy balance is also applied to each node to predict air temperatures such that

$$\sum_j \dot{Q}_{ji} + \dot{Q}_{source} = \rho_i V_i C_p \frac{\partial T_i}{\partial t} \tag{2.24}$$

where $\dot{Q}_{ji}$ is the energy flux from any neighboring node j to the current node i, $\dot{Q}_{source}$ is the total heat source in node i, V_i is the volume of air, and C_p is the heat capacity of air. The right side of the equation accounts for the energy increase in the zone assuming negligible thermal mass. If significant thermal mass exists in the zone, additional terms are correspondingly added.

Airflow network models are limited by a number of key assumptions. First, they neglect any momentum of the air by assuming very small air velocities. This assumption is reasonable in very large, open spaces, but does not apply in confined areas, such as in a narrow ventilation shaft. Another key assumption is that the air is well-mixed in the space and at a uniform temperature. This assumption works well for spaces with moderate to high air exchange rates and even distributions of heat sources and air inlets. However, it is questionable in spaces with an uneven distribution of heat sources or when air exchange rates are too small to sufficiently mix the air. When these assumptions are accurate, airflow network models have been shown to work well.

Numerous airflow network models have been developed for research purposes within the academic community. Takemasa et al. have used an airflow network model that couples airflow and energy calculations to solve for air change rates in a naturally ventilated building with a double facade [58] [57]. Yao et al. have used a simplified model for a single zone with minimal parameters, such as glazing area, internal gains, envelope U values, lighting level, thermostat set point, occupancy level,

and thermal mass type [66]. Their coupled airflow and thermal model integrates the British Standard natural ventilation calculation method for a single zone within a larger network model to predict airflow rates and temperatures [66]. Luo et al. have similarly developed a coupled thermal and airflow model in their airflow network model to predict air exchange rates and indoor temperatures [37]. Rousseau et al. have a similar model [50]. MIT has also developed an airflow network model by linking flow and thermal models called CoolVent, which has been validated by CFD models [67] [38]. While each of these models is slightly different, they all make the two key assumptions mentioned above. They neglect air momentum by assuming very small air velocities and they assume a uniform temperature for each zone. These assumptions break down in some important practical situations, which will be shown later in this dissertation.

Many commercially available airflow network models also exist. COMIS is an extremely modular stand-alone airflow network model developed at the Lawrence Berkeley National Laboratory in the late 1980s [68]. Although it accounts for airflow in the available code, COMIS is commonly coupled with thermal models like EnergyPlus or TRNSYS [68]. IEA Annex 23 performed numerous validation studies on COMIS, though most focussed on wind-driven or single zone systems [27]. Koinakis used COMIS coupled with the thermal model Suncode to model infiltration rates and cross ventilation in a full scale building [33]. He generally found good agreement between the model and experimental measurements, as indicated by Fig. 2-17 that shows zone air temperature over multiple days [33].

CONTAM is another widely used airflow network tool developed by the National Institute of Standards and Technology [63]. Although it can couple thermal and airflow calculations, it relies on prescribed indoor temperatures and does not iterate between airflow and air temperature calculations like many of the research models. One advantage of CONTAM over many other airflow network tools is its ability to model contaminant transport rates. Blomsterberg found favorable agreement between CONTAM predictions and measured flow rates in two Swedish classrooms, although he only considered wind-driven ventilation [12]. Blomsterberg mentions the possibility

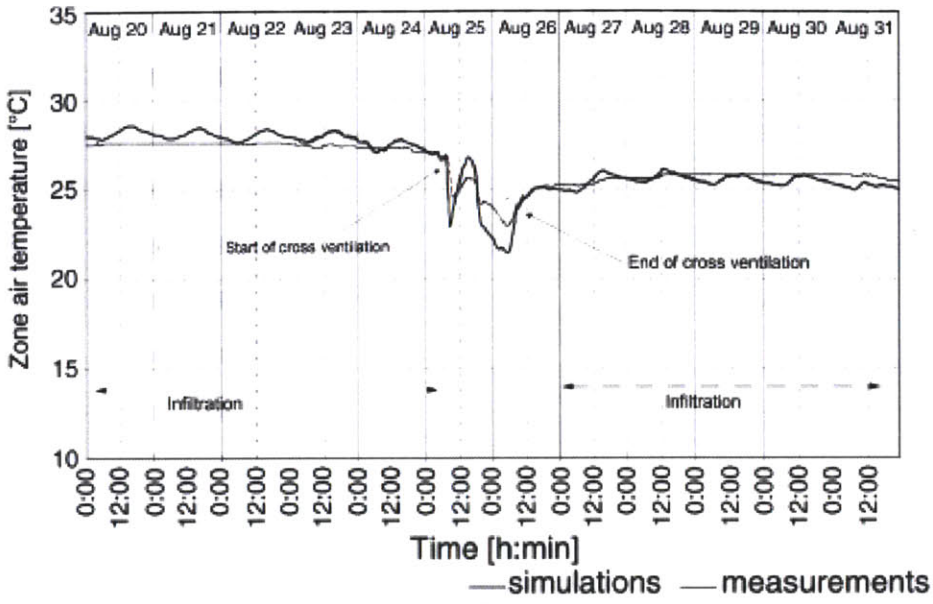

Figure 2-17: Simulated and measured zone air temperature for a cross ventilated building simulated with COMIS and Suncode [33].

of modeling the school's buoyancy-driven ventilation if CONTAM were coupled with a thermal model [12].

Whole-building simulation programs have incorporated airflow network models to simulate building ventilation as part of a larger and more complex building. The U.S. Department of Energy's EnergyPlus uses AIRNET, CONTAM's precursor, as the basis for its AirflowNetwork model. The AirflowNetwork model allows users to create zones within the building that are connected to each other and the outdoors. As with all other airflow network models, momentum effects are neglected and air temperatures are assumed uniform within each zone [22]. Fig. 2-18 shows how this airflow network model fits within the larger EnergyPlus design, illustrating the numerous building systems that can also be considered. This kind of integration of an airflow network model into a whole-building simulation program is essential for predicting the energy savings of a hybrid ventilation system. EnergyPlus uses an iterative process to apply an energy balance to each zone to solve for temperatures, and then uses those temperatures in the airflow network model to solve for flow rates, as illustrated by Fig. 2-19. Zhai et al. provides a simple high level explanation of

the airflow network model in EnergyPlus and the EnergyPlus Engineering Reference provides more detailed documentation [68] [22].

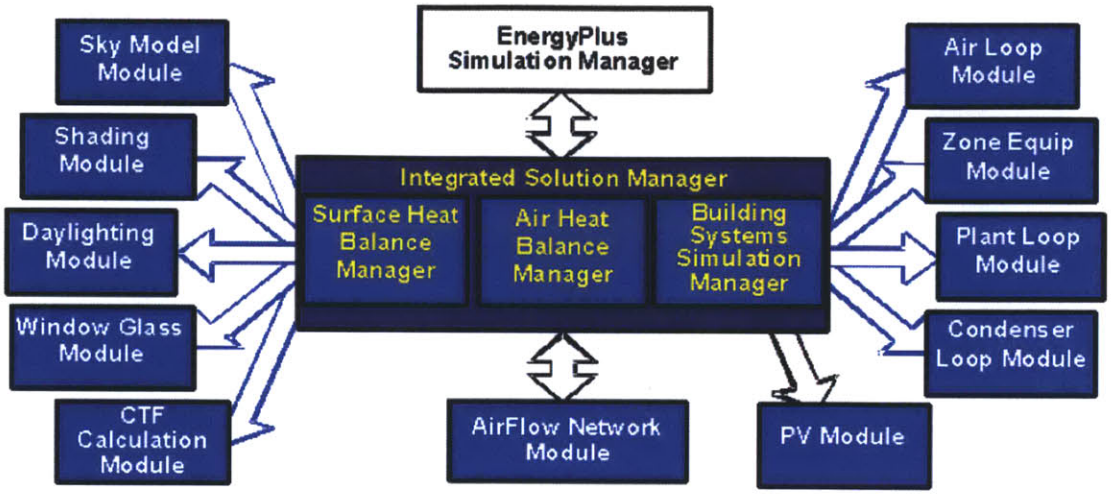

Figure 2-18: Program structure of EnergyPlus, a whole-building simulation program that has incorporated an airflow network model to account for airflow between zones [22]

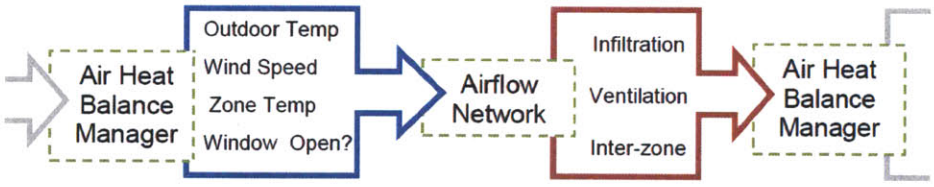

Figure 2-19: Iterative solving process in EnergyPlus that couples an energy balance with airflow calculations [68].

Airflow network models can predict the performance of an arbitrary natural ventilation system because of their modularity. However, their applicability is limited when momentum effects of the air are important or uneven temperature distributions are expected in each zone. When coupled with a whole-building simulation program, airflow network models can be used to predict annual building performance, including indoor temperatures and building energy use. These annual predictions are essential to the consideration of natural ventilation systems to ensure they can provide comfortable conditions all year and save energy over traditional mechanical systems.

2.5 Computational Fluid Dynamics

Computational fluid dynamics (CFD) models solve a series of partial differential equations for the conservation of momentum, mass, energy, containment concentrations, and turbulence quantities. The solution to these equations provides detailed predictions and distributions of dozens of variables. The geometry under consideration is divided into thousands if not millions of elements, which eliminates the need for the two major simplifying assumptions used in airflow network models. Consequentially, CFD models are very computationally intense and can take a long time to set up and solve the equations. Despite this time demand, uncertainties in the various turbulence models, and the significant knowledge of fluid mechanics required of its users, CFD models have grown in popularity for modeling natural ventilation. A recent review of building ventilation modeling techniques produced the chart in Fig. 2-20 to show the increase in the use of CFD modeling [46]. The same review surveyed the various modeling techniques used to predict ventilation performance in buildings published in 2007 in major English language journals and produced Fig. 2-21 to show that CFD models represented nearly 75% of the total number of models used to predict building ventilation performance.

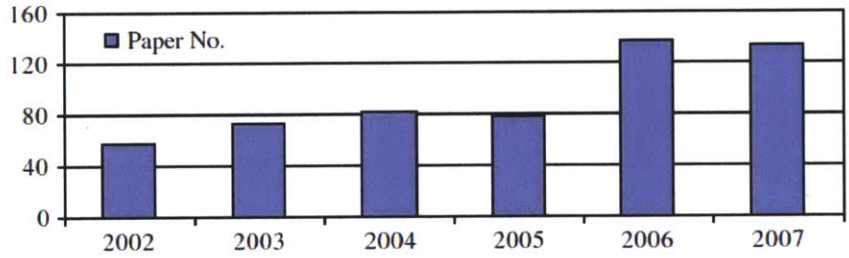

Figure 2-20: Total number of papers published between 2002-2007 in major English language journals using CFD to predict ventilation performance in buildings occupied by humans [46].

CFD models are well suited to predict detailed ventilation performance for a particular geometry under a very specific set of boundary conditions. Thus, they are commonly used in analyzing a few specific conditions of a final building design. They are not well suited for early design work when the building geometry is still un-

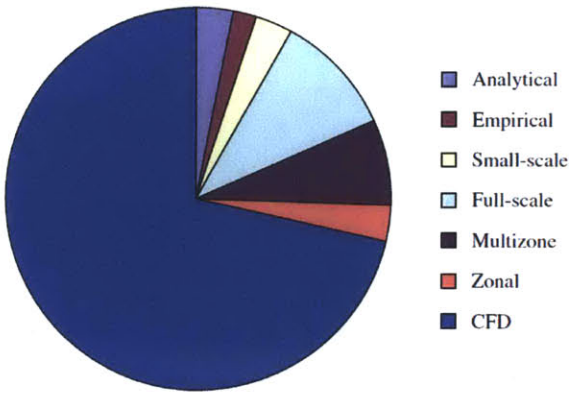

Figure 2-21: The use of various modeling techniques to predict ventilation performance in buildings published in 2007 in major English language journals [46].

known or when trying to evaluate annual performance when boundary conditions are constantly changing over a long period of time. An example of the typical analysis performed with CFD models is taken from Cook and Short's analysis of an auditorium in The Lichfield Garrick in Staffordshire, UK [19]. After the auditorium had been designed, they wanted to investigate where the air became stratified to ensure comfortable temperatures in the occupied zone [19]. Such analysis requires the exact geometry of the space and specific boundary conditions. While these boundary conditions will constantly change, typical values are used for this one-time analysis. The authors decided the results from these representative values provided enough information about the stratification to make the required design decisions [19]. Their simulated air stratification is shown in Fig. 2-22 for an outdoor temperature of 18 $^{\circ}C$.

While CFD modeling has been extensively validated and can accurately model arbitrary geometries [46], it does not provide annual performance information. Theoretically a simulation could be run for every hour of the year to obtain annual performance predictions, but would require too many resources to be practically viable. Thus, a major limitation to CFD modeling is that it can only provide a snapshot of how the building will perform under a very specific set of boundary conditions. Designers can not use CFD models to predict annual energy savings from a hybrid ventilation system or year-long indoor temperatures of a naturally ventilated building.

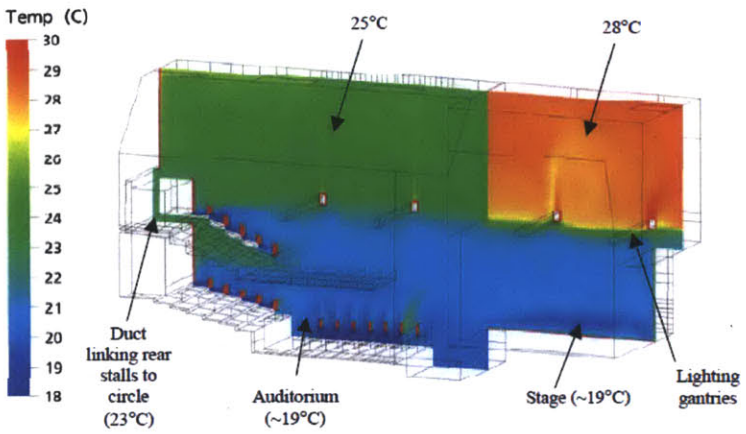

Figure 2-22: Typical use of CFD modeling to predict natural ventilation performance of a space during a single snapshot in time. This auditorium is part of The Lichfield Garrick in Staffordshire, UK and was designed and analyzed by Cook and Short. The outdoor temperature in this simulation is 18 $°C$ [19].

2.6 Summary of Current Natural Ventilation Modeling Techniques

Analytical models are simple, require few computing resources, and are rich in physical meaning. However, they provide little utility unless a simplified geometry sufficiently describes the actual building under consideration and the many assumptions are reasonably met. Empirical models can provide a practical approach to solve well known problems within a confined scope, however they can require significant experimental work or simulations to provide a range of parameters within which the model applies. Empirical models based solely on experimental data and no underlying physics should strictly be used in near replications of the experiments used to determine them.

Small scale models provide a less resource-intensive physical modeling technique than full scale replications. However, boundary conditions must be carefully reproduced in the small scale model and the pertinent dimensionless parameters, in theory, must be equal. In practice, it is nearly impossible to match many dimensionless paramters, such as the Re, Gr, or Ar because of their interdependence. Threshold

values for these parameters have been suggested, above which the model will accurately approximate the full scale prototype even if the parameters do not equal. Although some researchers have proposed an absolute threshold, their justification for such a value is lacking. Specifically, the proposed Gr threshold of $10^6 - 10^9$ should be reconsidered.

Full scale models provide a very accurate modeling technique without many simplifying assumptions. However, they are extremely resource-intensive, which severly limits their use. Full scale modeling of small components within a natural ventilation system can provide helpful insight into those components, but modeling an entire system at full scale is impractical. Although some full scale natural ventilation experiments have been conducted, a more complete data set is needed. Specifically, a higher resolution of temperature measurements and measured airflow rates are needed. Airflow visualization techniques are essential for observing complex airflow patterns undetectable by typical instrumentation. However, many of the currently used visualization techniques introduce artificial density gradients that are inconsequential in inertia-dominated flows, but skew results in buoyancy-dominated flows. Thus, airflow visualization techniques for buoyancy-dominated flows can be improved by eliminating these artificial density gradients.

Airflow network models are significantly more resource efficient than full scale models and can predict the performance of an arbitrary natural ventilation system because of their modularity. However, two major assumptions limit their applicability when momentum effects of the air are important or uneven temperature distributions are expected in the space. They can provide helpful predictions of annual building performance, such as indoor temperatures and building energy use, when coupled with a whole-building simulation program. These annual predictions are essential to the consideration of natural ventilation systems to ensure they can provide comfortable conditions all year and save energy over traditional mechanical systems. Airflow network models can be improved by accounting for momentum effects of the air and non-uniform temperature distributions within the simulated space.

CFD modeling is becoming more widely used in simulating building ventilation.

It has been extensively validated and can accurately model arbitrary geometries, but does not provide annual performance information. It requires a sufficient understanding of fluid mechanics, reasonable computing power, and a detailed geometric input. A further limitation of CFD modeling is that it can only provide a snapshot of how the building will perform under a very specific set of boundary conditions. Designers can not use CFD models to predict annual energy savings from a hybrid ventilation system or year-long indoor temperatures of a naturally ventilated building.

Chapter 3

Small Scale Experimentation of Buoyancy-Driven Ventilation

Small scale experiments are conducted for two primary reasons. First, they provide a flexible physical model that can easily model a variety of flow types. Second, they are used to validate CFD models that provide even greater flexibility in modeling.

3.1 Prototype Building Description

The prototype building is a ten story 7,780 m^2 office building located in downtown Tokyo. The building incorporates an array of energy efficient measures including daylighting systems, occupancy sensors, advanced building controls, and a hybrid ventilation system on floors 3-9 [47]. The first two floors are reserved for commercial tenants and the tenth floor houses executive offices that require mechanical ventilation. An exterior perspective and plan view of the building are shown in Fig. 3-1.

Inlet ducts on the NW facade on floors 3-9 supply outdoor air to the space when the natural ventilation system is in operation. The open floor plan allows air to flow to two ventilation shafts located toward the back of the building. To prevent reverse flow in the upper floors, two shafts (2.8 m^2 each) are used to ventilate floors 3-7 and two separate shafts (2 m^2 each) are used to ventilate floors 8 and 9. Low power fans (500 W and 250 W for shafts 3-7 and 8-9 respectively) atop each chimney leverage the

Figure 3-1: External perspective and plan view of prototype building used in small scale experimentation. This ten story new corporate headquarters building is located in downtown Tokyo.

low airflow resistance of the building to extend the period during which fan-assisted natural ventilation can be used.

3.2 Model Building Description

A 1/4 scale model is constructed of a portion of one of the ventilation shafts to more closely investigate the flow within the shaft. Although this small scale analysis considers only a portion of the ventilation shaft, additional studies have analyzed the airflow in other parts of the building [40] [47]. The model simulates the air flow from three floors connected to a 4 m^2 ventilation shaft. Fig. 3-2 shows a picture and drawing of the model where three take-off ducts represent the connections from three floors. Heaters in each take-off duct generate heat to provide the buoyancy force required to induce natural ventilation through the model. Wind-driven flow is not considered.

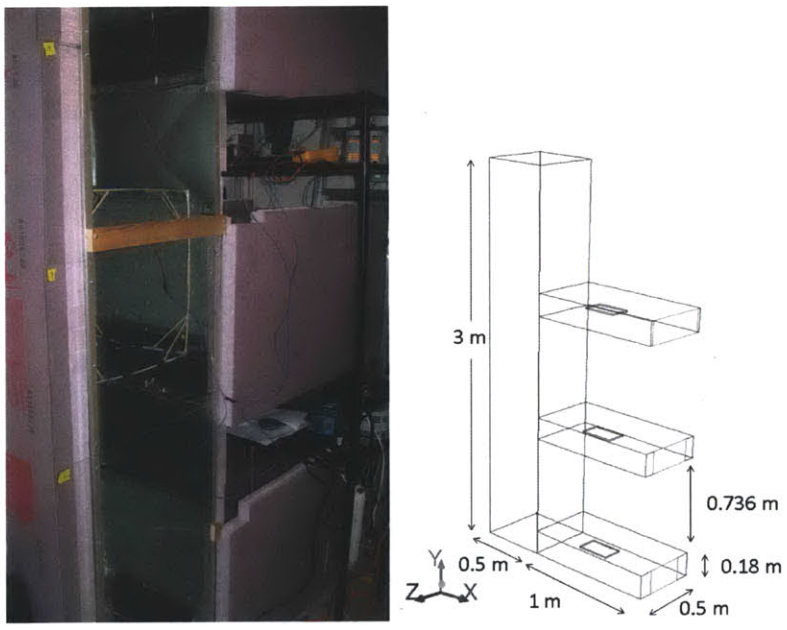

Figure 3-2: Photograph and drawing of 1/4 scale model used to simulate natural ventilation through a ventilation shaft.

3.2.1 Model Construction

The model is constructed of $1/32$ in stainless steel surrounded by 2 in of R$-$10 or 1.76 m^2K/W extruded polystyrene insulation. One side of the ventilation shaft is removed and covered with transparent $3/32$ in OPTIX acrylic sheets to provide a view into the shaft, which can be seen in Fig. 3-2. The ventilation shaft is lined with $1/16$ in black felt to enhance flow visualization techniques. A rectangular resistance heater measuring 10 in by 6 in is placed in each duct, at $x = 0.8$ m, $z = 0.25$ m, and y equal to the midpoint of each duct. Each heater is suspended at the midpoint of each duct using two $1/32$ in strips of stainless steel. The heater power consumption is controled with a Variac variable autotransformer by regulating the voltage to the heater from $0 - 140V$. The resistance of each heater varies no more than 2% over the entire range of supplied voltage, as shown in Fig. 3-3. Power consumption is determined by the product of the measured voltage and current. The voltage supplied to each heater is measured using a Flex-core AVT 150CX5 AC voltage transducer connected to a Campbell Scientific CR1000 datalogger [15][25]. The current is measured using a Fluke 115 multimeter [26].

The model is contained within a sealed test chamber measuring 10 ft wide, 20 ft deep, and 20 ft tall and conditioned with a water-chilled fancoil unit. The model has been arranged within the space such that the jet from the fancoil unit does not interact with the inlet or exhaust openings. Thermocouples measure the inlet temperature at each takeoff duct to ensure uniformity. A typical distribution of inlet temperatures during a test is shown in Fig. 3-4.

3.2.2 Model Instrumentation

The airflow within the ventilation shaft is characterized in three ways through temperature measurements, airflow measurements, and a flow visualization technique. All measurements are made after steady state has been reached, which is defined as the point when temperatures within the shaft vary less than 0.77 $°C$, which is also the accuracy of the temperature measurement system. Between 48 and 72 temperature

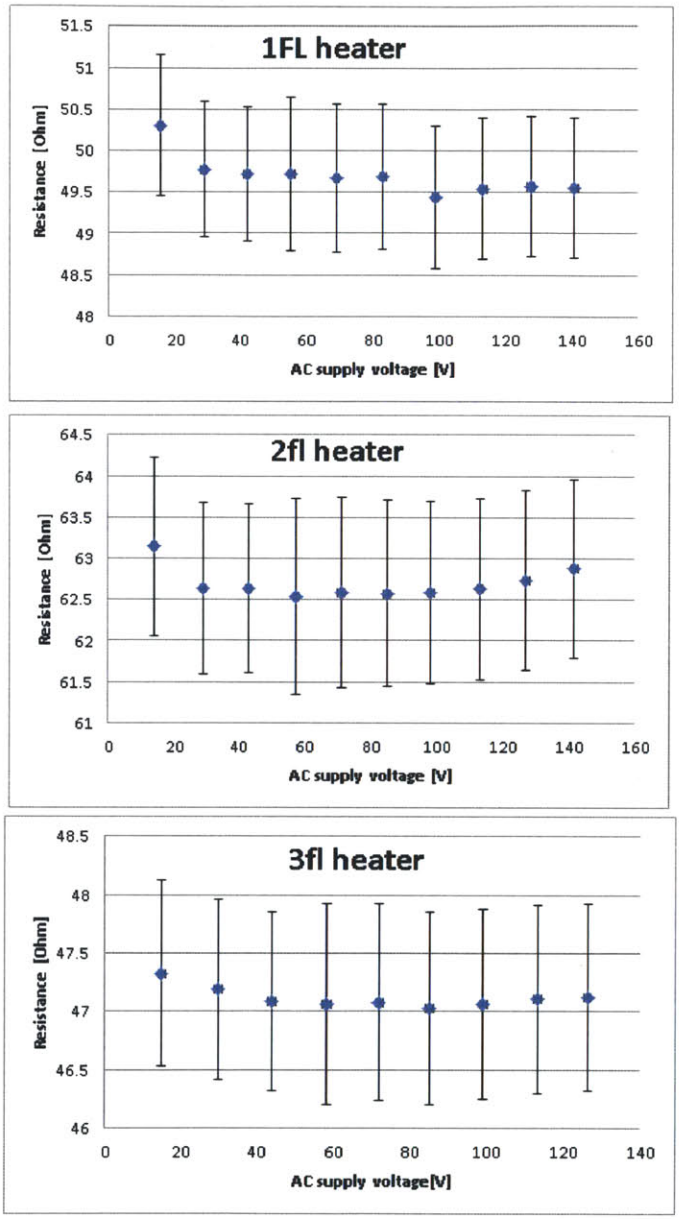

Figure 3-3: Plots of resistance versus voltage for the three heaters used in this experiment, indicating less than a 2% variation in resistance over the entire range of supplied voltages.

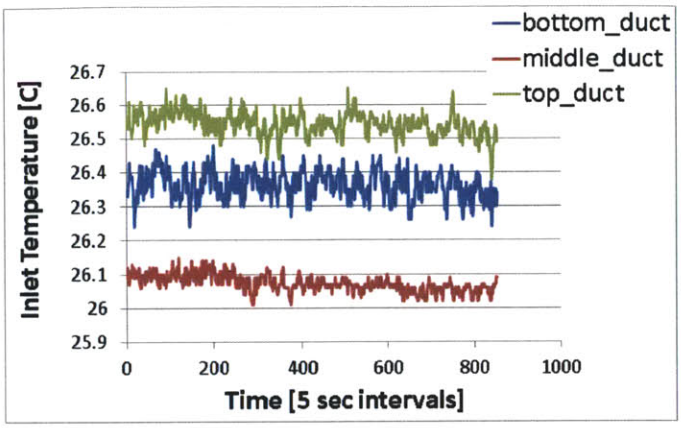

Figure 3-4: Typical inlet temperature distribution measured during a single test, which shows a maximum of roughly 0.5 $°C$ difference between inlets.

measurements are made in the shaft using a thermocouple rake of 24 thermocouples that measures 12 temperatures at two elevations. Omega PR-T-24-SLE type T thermocouple wire is used with a stated accuracy of 0.5 $°C$ or 0.4% in the range of 0 to 350 $°C$ [45]. The 12 thermocouples at each elevation are arranged to provide higher resolution near the entrance to the shaft. Their exact configuration is shown in Fig. 3-5. A Campbell Scientific CR1000 datalogger with an attached AM25T multiplexer is used to acquire temperature measurements every 5 s. The CR1000 has a stated accuracy of 0.12% rdg $+1.5 * resolution + 1.0\mu V$ or 0.07 $°C$ and the AM25T has a stated accuracy of 0.2 $°C$ [15][14].

An ice bath test is performed before the thermocouples are attached to the rake to ensure sufficient precision between the 24 thermocouples. A segment of the test results is shown in Fig. 3-6 where the temperature measurements are shown to fall within 0.15 $°C$ of each other. The slight peaks indicate the response time of the system and were created by temporarily reducing the amount of stirring in the ice bath.

Volumetric flow rates are measured at each inlet in accordance with ASHRAE Standard 111-2008 using the equal area method for the entrance to a rectangular duct [8]. Between 9 and 16 velocity measurements are taken at each inlet using a Graywolf AS-201 hotwire anemometer, which has a stated accuracy of $+/-$ 3% rdg

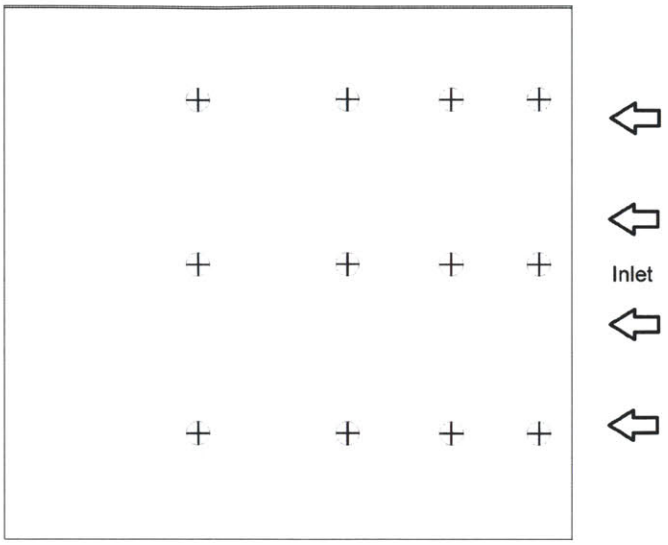

Figure 3-5: Thermocouple arrangement on a single plane of the thermocouple rake that provides higher resolution near the entrance to the shaft, shown on the left side of the diagram. The double-lined side indicates the clear acrylic sheet.

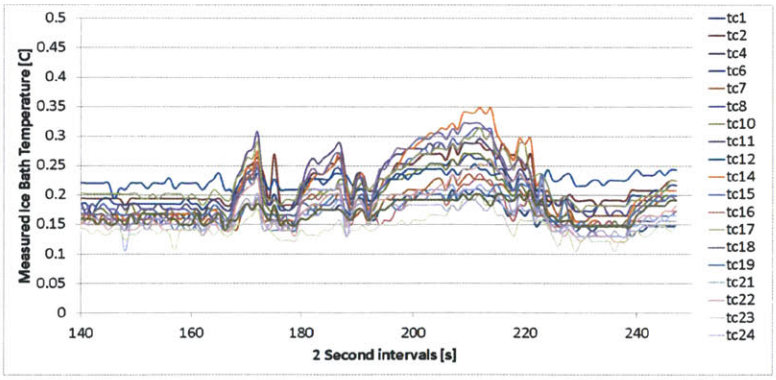

Figure 3-6: Measured temperature of an ice bath using 24 thermocouples to test their precision. Measurements fall within 0.15 $°C$ of each other for all 24 thermocouples. The slight peaks indicate the response time of the system and were created by temporarily reducing the amount of stirring in the ice bath.

$+/-$ 0.015 m/s [29]. The measurements are made flush with the inlets to increase the liklihood of unidirectional flow.

Airflow visualization is provided by neutrally buoyant bubbles photographed by a digital SLR camera. The bubbles are created using the SAI^{TM}Model 5 Bubble Generator, which generates 1/16 in diameter helium-filled soap bubbles. The Model 5 Bubble Generator, shown in Fig. 3-7 has a mini-vortex filtering system that ensures only neutrally buoyant bubbles are introduced into the desired space. This filtering system uses the radial forces from the plug-in head to establish a cyclonic flow in which heavy bubbles sink to the bottom, light bubbles float to the top, and neutrally buoyant bubbles are ejected through the outlet tube [3].

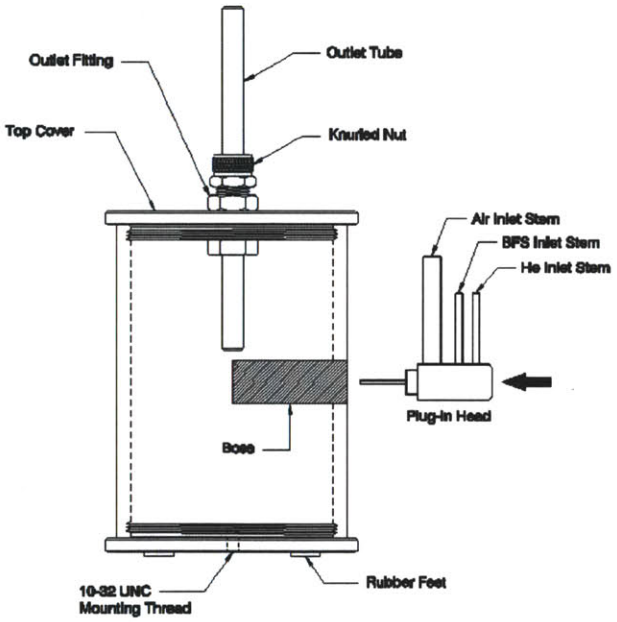

Figure 3-7: Schematic drawing of the mini-vortex filtering system of the SAI^{TM}Model 5 Bubble Generator [3].

Flexible tubing directs the bubbles from the outlet tube to the desired location within a space. In this case, the tube is mounted orthogonally to the inlet airflow to ensure no bubble momentum from the generator is carried into the direction of the flow. The ventilation shaft is lined with 1/16 in thick black felt to accentuate the bubbles in the shaft that are illuminated from above. A digital SLR camera with a

50 mm lens photographs the bubbles using a shutter speed between 1/6 to 1/2 s to create streaks that corresponds to bubble pathlines.

3.3 Small Scale Experimental Procedure

Two configurations of the small scale model are initially tested. The first configuration, shown in Fig. 3-2, simulates the airflow in a ventilation shaft connected to three floors by a small duct on each floor. The second configuation, shown in Fig. 3-8, simulates the airflow in a ventilation shaft resulting from floor-to-ceiling connections on three floors.

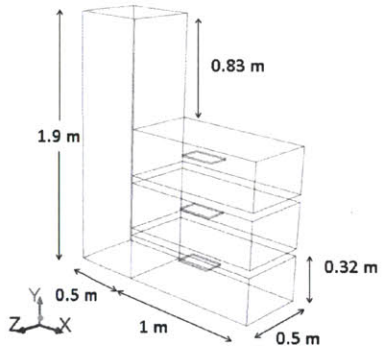

Figure 3-8: Drawing of second configuration of 1/4 scale model used to simulate natural ventilation through a ventilation shaft connected to three floors with floor-to-ceiling openings.

Steady state conditions are assumed to be reached when temperatures within the shaft vary less than 0.77 $°C$, which is also the stated accuracy of the temperature measurement system. All data is collected after steady state conditions are reached. Three tests are run for each configuration. Temperature readings are averaged over the length of the test, which varies from 45 to 130 minutes. Average inlet temperatures for tests run in configuration one are 26.4, 26.2, and 26.8 $°C$ for the bottom, middle, and top ducts respectively. In configuration two, the average inlet temperatures are 22.9, 23.5, and 23.2 $°C$ for the bottom, middle, and top ducts respectively. The thermocouple rake depicted in Fig. 3-5 measures 72 temperatures at six elevations in configuration one and 48 temperatures at four elevations in configuration two. Due

Table 3.1: Measured heater power consumption for both experimental configurations

Takeoff Duct	Config. 1 Heater Power $[W]$	Config. 2 Heater Power $[W]$
Top	$148 +/- 2.6$	$144 +/- 2.6$
Middle	$148 +/- 2.6$	$146 +/- 2.6$
Bottom	$149 +/- 2.6$	$150 +/- 2.6$

to a lack of resolution in the heater control, each heater consumed a slightly different amount of power, though their variation was less than 4% as shown in Table 3.1.

3.4 CFD Model Description

One of the purposes of the small scale models is to validate CFD models. The commercially available CFD software Fluent is used to compare the ability of three turbulence models to simulate the physical experiments. Specifically, the $k\epsilon$, $k\epsilon$ RNG, and large eddy simulation (LES) turbulence models are compared. The exact experimental geometry is used for the CFD simulation with the exception of the thin heater supports. Grid independence tests indicate mesh sizes of 301,000 and 251,000 cells are sufficient for the first and second configurations respectively. The mesh density is increased near the heaters and entrance to the ventilation shaft. Simulations are run under transient conditions, but are assumed to reach steady state when the bulk exhaust temperature varies less than 0.003 $°C$ for the two $k\epsilon$ models and 0.45 $°C$ for the LES model.

Radiation is accounted for using the Surface to Surface radiation model with a residual convergence criteria of 0.001. The enhanced wall function of the $k\epsilon$ and $k\epsilon$ RNG model is used with enhanced thermal effects and full buoyancy effects are also considered. The Smagorinsky-Lilly subgrid-scale model is used in the LES model. Reference and operating temperatures are set to the measured chamber air temperature of 299 K.

Table 3.2: Summary of thermal properties of materials used in small scale model, which are transferred to the CFD model

Material	Density $[kg/m^3]$	Specific Heat $[J/kgK]$	Conductivity $[W/mK]$
Insulation	20	1500	0.029
Acrylic Sheet	1250	1210	0.20

3.4.1 Boundary Conditions

In addition to replicating the exact experimental geometry, much care is given to replicating the experimental boundary conditions. The thermal properties of all materials used in the experimental model are used in the CFD model and summarized in Table 3.2. The duct is assumed to provide negligible thermal resistance compared to the 2 in foam insulation. The external boundary condition for the insulation or acrylic sheet is the "Convection" thermal condition in Fluent, which uses a specified constant heat transfer coefficient of 10 W/m^2K and a specified external temperature of 299 K, the measured air temperature in the test chamber. The heater power consumptions are also matched in the CFD model using a constant heat flux boundary condition. A "pressure-outlet" condition at 0 Pa gauge pressure is used to model the inlet and exhaust openings, which assumes all backflow is normal to the opening. A "porous-jump" condition is also used at each opening to simulate the pressure loss from converging or expanding flow. The porous-jump condition uses a finite thickness medium over which a calculated pressure loss is applied according to

$$\Delta P = -\frac{1}{2} C_2 \rho v^2 \tag{3.1}$$

where C_2 is the dimensionless pressure loss coefficient [6]. Well accepted pressure loss coefficients for this type of converging and expanding flow are 0.5 and 1 respectively [32]. Before assigning a pressure loss coefficient, the CFD model is run with no pressure coefficients to establish a flow direction across each opening. After a flow direction is established, the appropriate pressure loss coefficient is applied to the openings.

3.5 Results from Physical and CFD Models

Experimentally measured temperatures are plotted against simulated temperatures for the three turbulence models in both configurations in Figs. 3-9 through 3-14. The solid line has a slope of one, and the dotted lines represent the bounds of the experimental error, 0.77 $^{\circ}C$.

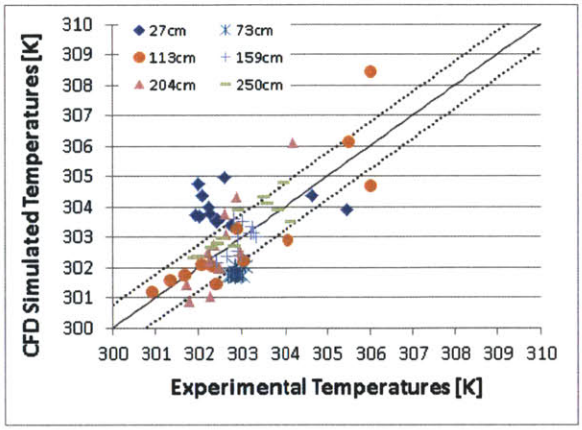

Figure 3-9: Average experimental temperatures plotted against CFD simulated temperatures using the $k\epsilon$ turbulence model for configuration one. The solid line has a slope of one, and the dotted lines represent the bounds of the experimental error, 0.77 $^{\circ}C$. Different symbols indicate from which elevation measurements are taken.

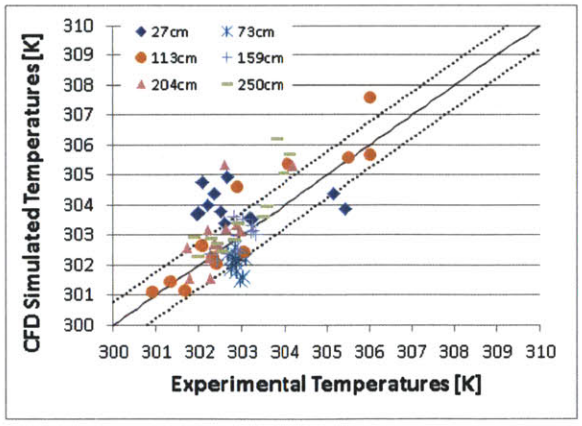

Figure 3-10: Average experimental temperatures plotted against CFD simulated temperatures using the $k\epsilon$ RNG turbulence model for configuration one. The solid line has a slope of one, and the dotted lines represent the bounds of the experimental error, 0.77 $^{\circ}C$. Different symbols indicate from which elevation measurements are taken.

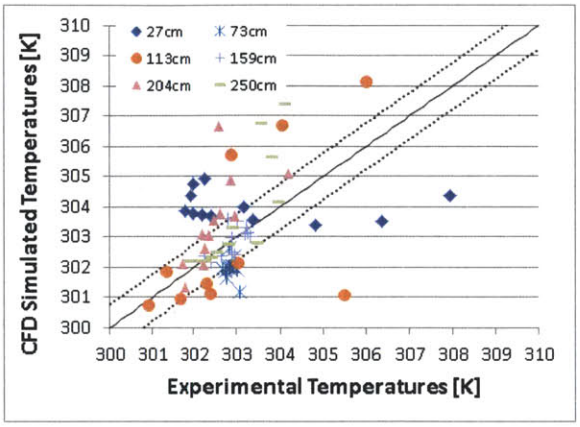

Figure 3-11: Average experimental temperatures plotted against CFD simulated temperatures using the LES turbulence model for configuration one. The solid line has a slope of one, and the dotted lines represent the bounds of the experimental error, 0.77 $°C$. Different symbols indicate from which elevation measurements are taken.

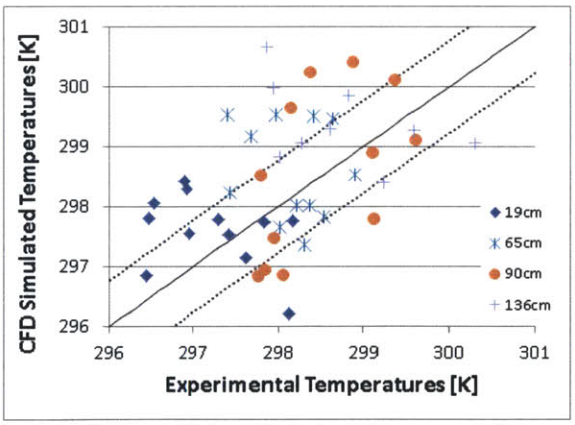

Figure 3-12: Average experimental temperatures plotted against CFD simulated temperatures using the $k\epsilon$ turbulence model for configuration two, which has floor-to-ceiling openings. The solid line has a slope of one, and the dotted lines represent the bounds of the experimental error, 0.77 $°C$. Different symbols indicate from which elevation measurements are taken.

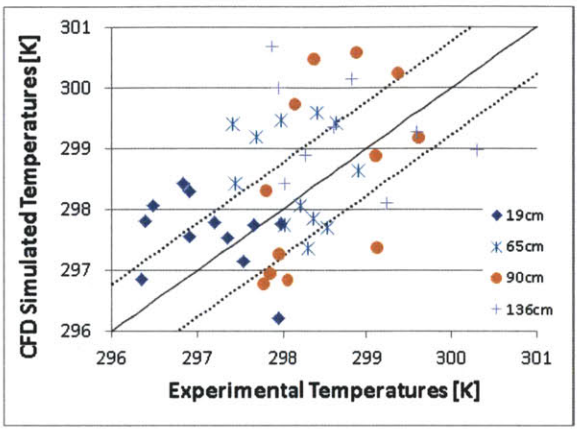

Figure 3-13: Average experimental temperatures plotted against CFD simulated temperatures using the $k\epsilon$ RNG turbulence model for configuration two, which has floor-to-ceiling openings. The solid line has a slope of one, and the dotted lines represent the bounds of the experimental error, 0.77 $°C$. Different symbols indicate from which elevation measurements are taken.

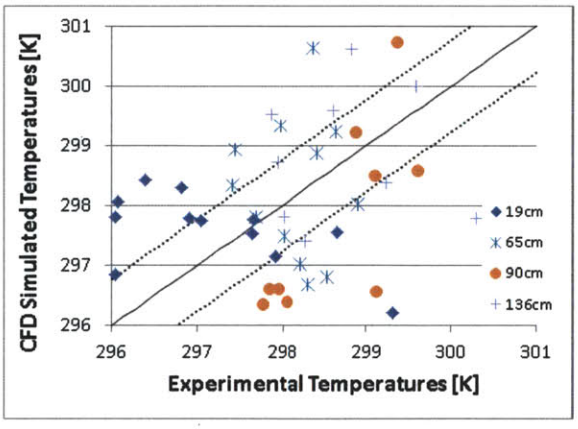

Figure 3-14: Average experimental temperatures plotted against CFD simulated temperatures using the LES turbulence model for configuration two, which has floor-to-ceiling openings. The solid line has a slope of one, and the dotted lines represent the bounds of the experimental error, 0.77 $°C$. Different symbols indicate from which elevation measurements are taken.

Table 3.3: RMSE for three turbulence models in configuration one. All 72 thermocouples (TCs) are included in the first row, but only the upper 48 TCs are considered in the second row. All values are reported in units $[°C]$ and the experimental error is 0.77 $°C$.

# of TCs	$k\epsilon$	$k\epsilon$ RNG	LES
all 72 TCs	1.09	1.03	1.92
upper 48 TCs	0.97	0.89	1.92

Table 3.4: RMSE for three turbulence models in configuration two. All 48 thermocouples (TCs) are included in the first row, but only the upper 24 TCs are considered in the second row. All values are reported in units $[°C]$ and the experimental error is 0.77 $°C$.

# of TCs	$k\epsilon$	$k\epsilon$ RNG	LES
all 48 TCs	1.32	1.38	1.76
upper 24 TCs	1.55	1.65	2.08

Given the large number of temperature measurements, another comparison between experimental and simulated temperatures is made. The root mean square error (RSME) between the measured and simulated temperatures is also calculated for each turbulence model. The RSME is a measure of the magnitude of the mean error between two data sets and is defined as

$$RSME = \sqrt{\frac{\sum_1^n (T_{exp,i} - T_{sim,i})^2}{n}} \tag{3.2}$$

where n is the total number of measurements, $T_{exp,i}$ is the experimental temperature at location i, and $T_{sim,i}$ is the simulated temperature at location i. The RSME for the three turbulence models in configuration one are reported in Table 3.3, where the RSME of the upper 48 thermocouples is also reported. Table 3.4 presents the RSME for configuration two.

A comparison of the measured volumetric flow rates at the three inlets to the simulated flow rates for each of the three turbulence models is shown in Tables 3.5-3.6.

Experimental airflow visualization at the entrance from each takeoff duct to the ventilation shaft for configuration one is provided in Figs. 3-15, 3-19, and 3-23. Sim-

Table 3.5: Measured and simulated airflow rates at each takeoff duct for configuration one. All values are reported in units $[m^3/s]$.

Takeoff Duct	Exp. average	Exp. std. dev.	$k\epsilon$	$k\epsilon$ RNG	LES
Top	0.023 +/− 0.0019	0.00079	0.0212	0.0203	0.0201
Middle	0.027 +/− 0.0017	0.0020	0.0265	0.0272	0.0267
Bottom	0.029 +/− 0.0016	0.0010	0.0316	0.0326	0.0310

Table 3.6: Measured and simulated airflow rates at each takeoff duct for configuration two. All values are reported in units $[m^3/s]$.

Takeoff Duct	Exp. average	Exp. std. dev.	$k\epsilon$	$k\epsilon$ RNG	LES
Top	0.021 +/− 0.0063	0.0016	0.0258	0.0259	0.0263
Middle	0.018 +/− 0.0058	0.00094	0.0225	0.0223	0.0211
Bottom	0.032 +/− 0.0083	0.0041	0.0292	0.0291	0.0278

ulated pathlines are created with the CFD software and overlaid on the experimental images to provide a qualitative comparison between the simulated and experimental airflow paths.

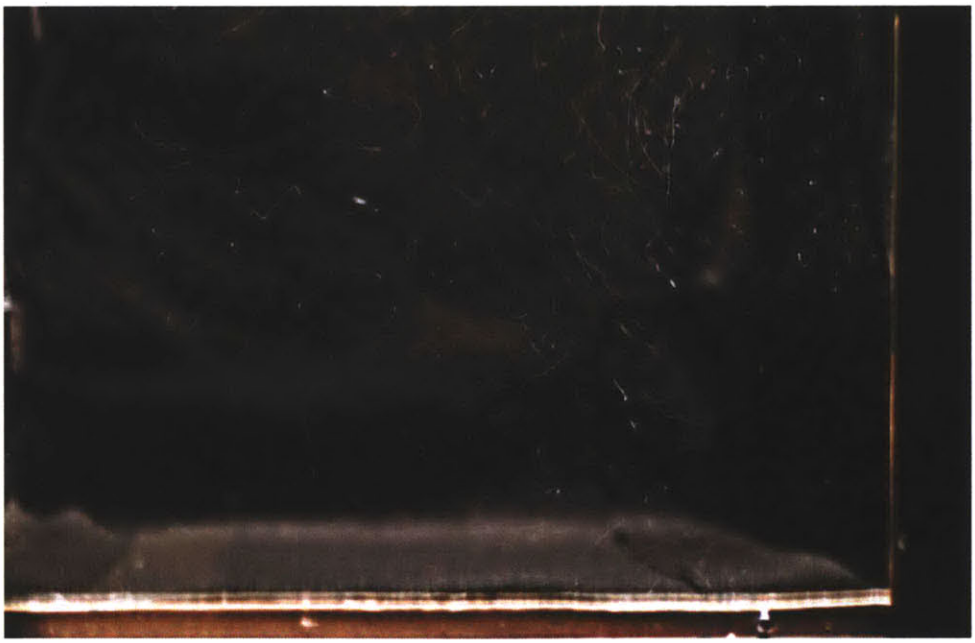

Figure 3-15: Experimental airflow visualization of entrance to model ventilation shaft at the bottom takeoff duct.

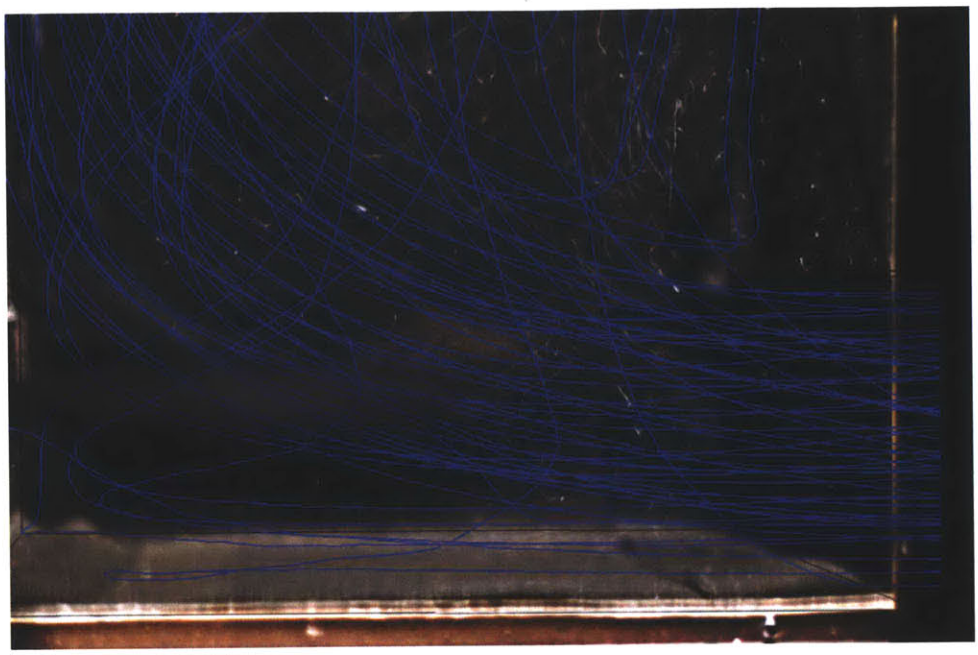

Figure 3-16: Simulated pathlines from $k\epsilon$ model overlaid on experimental airflow visualization of entrance to model ventilation shaft at the bottom takeoff duct.

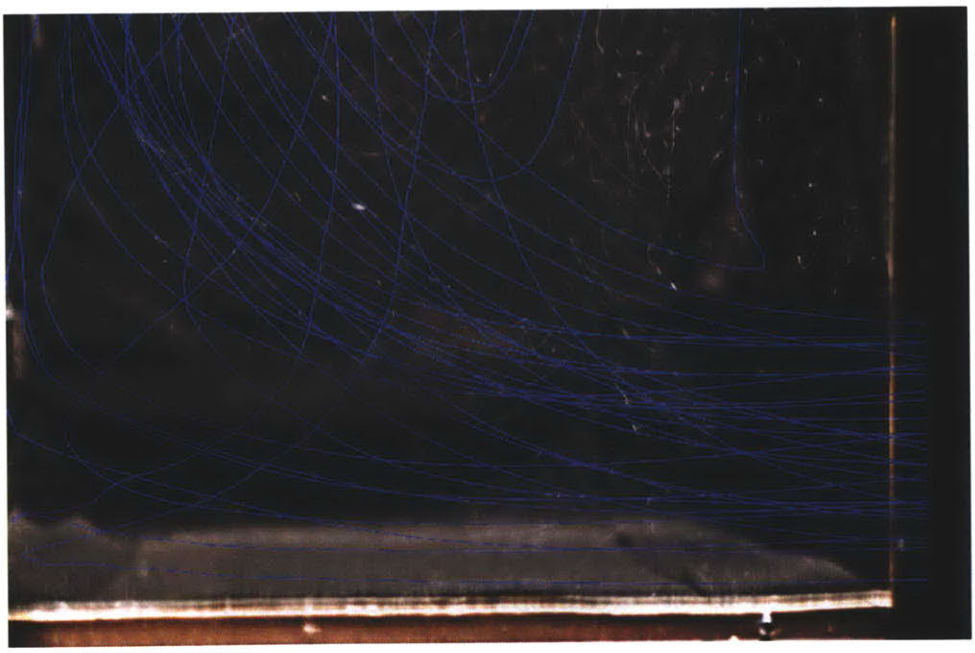

Figure 3-17: Simulated pathlines from $k\epsilon$ RNG model overlaid on experimental airflow visualization of entrance to model ventilation shaft at the bottom takeoff duct.

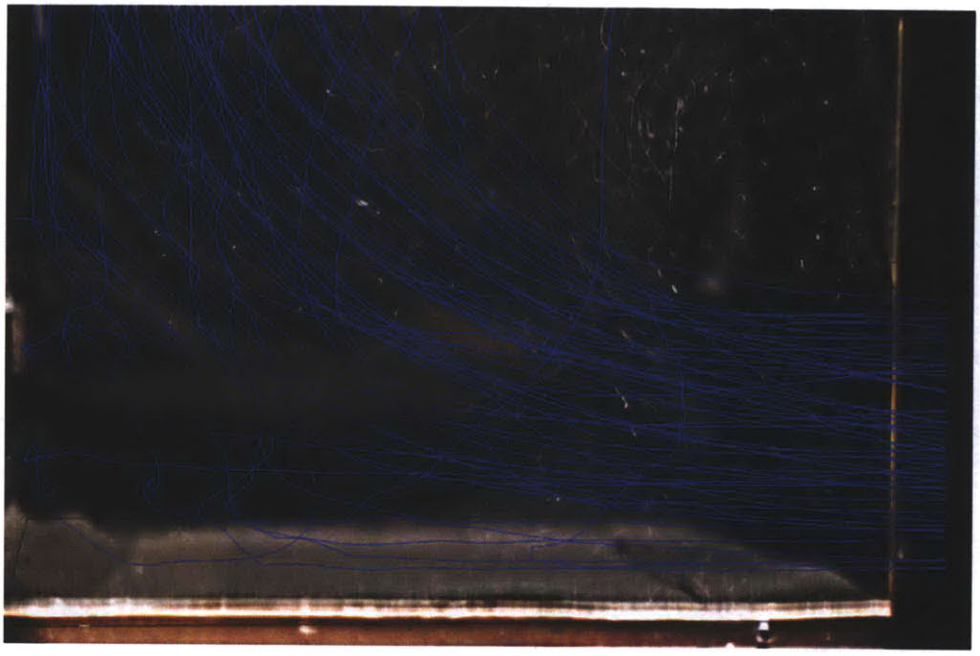

Figure 3-18: Simulated pathlines from LES model overlaid on experimental airflow visualization of entrance to model ventilation shaft at the bottom takeoff duct.

Figure 3-19: Experimental airflow visualization of entrance to model ventilation shaft at the middle takeoff duct.

Figure 3-20: Simulated pathlines from $k\epsilon$ model overlaid on experimental airflow visualization of entrance to model ventilation shaft at the middle takeoff duct.

Figure 3-21: Simulated pathlines from $k\epsilon$ RNG model overlaid on experimental airflow visualization of entrance to model ventilation shaft at the middle takeoff duct.

Figure 3-22: Simulated pathlines from LES model overlaid on experimental airflow visualization of entrance to model ventilation shaft at the middle takeoff duct.

Figure 3-23: Experimental airflow visualization of entrance to model ventilation shaft at the top takeoff duct.

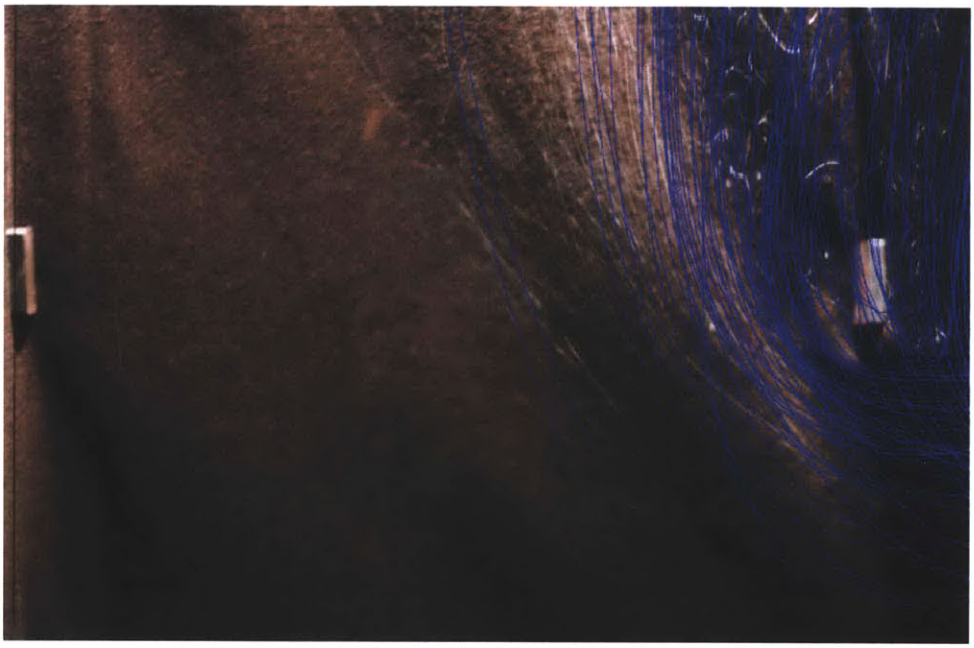

Figure 3-24: Simulated pathlines from $k\epsilon$ model overlaid on experimental airflow visualization of entrance to model ventilation shaft at the top takeoff duct.

Figure 3-25: Simulated pathlines from $k\epsilon$ RNG model overlaid on experimental airflow visualization of entrance to model ventilation shaft at the top takeoff duct.

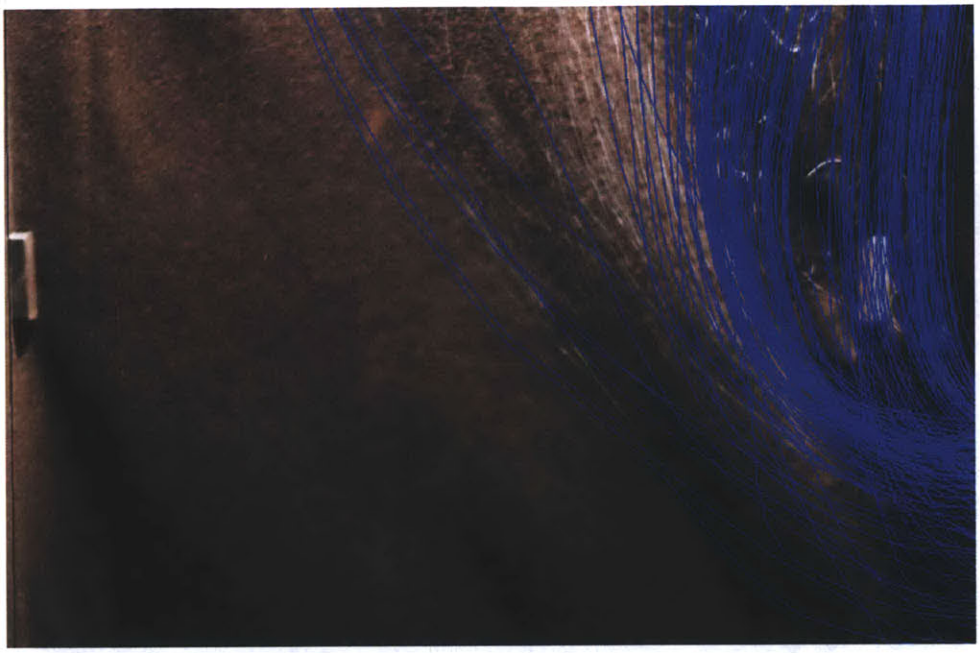

Figure 3-26: Simulated pathlines from LES model overlaid on experimental airflow visualization of entrance to model ventilation shaft at the top takeoff duct.

3.6 Discussion of Physical and CFD Models

3.6.1 Physical and CFD Model Agreement

The correlation between experimental and CFD predicted temperatures, flow rates, and pathlines provides strong evidence for the validation of both $k\epsilon$ and $k\epsilon$ RNG models in configuration one and two. The largest disagreement between experimental and simulated values is found for the LES model in both configurations.

The root mean square error (RMSE) between experimental and simulated temperatures for the $k\epsilon$ and $k\epsilon$ RNG models in configuration one is 1.09 $^{\circ}C$ and 1.03 $^{\circ}C$, which is nearly half of the LES value, 1.92 $^{\circ}C$. The same trend generally holds for configuration two where the RMSE for the $k\epsilon$, $k\epsilon$ RNG, and LES is 1.32, 1.38, and 1.76 $^{\circ}C$ respectively. In configuration one, the largest differences between measured and simulated temperatures for the two $k\epsilon$ models occur in two places. First, large disagreements are observed near the bottom takeoff duct, where the entering air expands to fill the entire shaft. The points corresponding to the 27 and 73 cm

elevations in Figs 3-9 and 3-10 generally fall further from the $y = x$ line than the points in other regions. Near the bottom takeoff duct, very small pressure gradients can significantly affect the flow because there is no other established flow in the shaft. When this region is not included in the RSME calculation, the error decreases. The RSMEs of 1.09 and 1.03 $°C$ for the $k\epsilon$ and $k\epsilon$ RNG models respectively are reduced to 0.97 and 0.89 $°C$ respectively. Large errors are also observed at a few thermocouples near the exhaust plume at the middle and top takeoff ducts. The largest temperature gradients in the shaft are near these plumes, so a slight unsteadiness in the flow can lead to large temperature differences.

The comparison of measured and simulated airflow rates also suggests both $k\epsilon$ models are more accurate, although all three models provide similar results. The simulated results for configuration one agree with experimental values better than the simulated results for configuration two. The larger openings and proximity of takeoff ducts within the ventilation shaft allow smaller pressure gradients to affect the flow more than in configuration one. Thus, small differences in the simulation have a larger affect on the flow in configuration two than in configuration one. A quantitative comparison of the three models in each configuration further illustrates the point. The largest percent difference between the measured and simulated flow rates in configuration one for the $k\epsilon$, $k\epsilon$ RNG, and LES models is 9.2%, 13%, and 14%, respectively. In configuration two, the same comparison for the $k\epsilon$, $k\epsilon$ RNG, and LES models yields errors of 18%, 18%, and 20 %. Furthermore, in configuration one the flow rates through the bottom takeoff duct are overpredicted in each model. The flow rates through the middle duct are quite accurate and differ from experimental values by less than 2 %, while the flow rates through the top duct are under predicted. In configuration two, the flow rate through the bottom takeoff duct is consistently underpredicted, while the flow rates through the middle and top ducts are over predicted.

Simulated pathlines for all three turbulence models sufficiently predict the profile of the airflow entering the shaft from each duct in configuration one. Both experimental images and simulated pathlines show a rapid expansion of the air entering the

shaft through the bottom duct. In the middle duct, the profile is more defined as the air entering through the bottom duct creates a region of relatively high pressure on the left side of the image. This region of high pressure causes the flow to bend more sharply than it does at the bottom duct. The flow entering from the top duct bends even more sharply as the established flow from the bottom two ducts creates a region of higher pressure than at the middle duct. The air entering the shaft through the top duct only occupies half of the ventilation shaft because of the existing flow from lower ducts.

3.6.2 Airflow Rates in Configuration Two

Since no wind is present in the experiment or simulations, the only driving force of the flow is from buoyancy effects. In buoyancy driven flow, the height difference between the inlet and outlet is a crucial parameter in determining the airflow. If all other variables are held constant, a larger height differential leads to larger flow. Recall Eq. 2.5 for the uniform temperature case and Eq. 2.7 for the constant heat flux case. However, both experimental and simulated airflow rates in configuration two yield higher flow rates through the top duct than the middle duct even though all other parameters are nearly constant. The heater powers slightly vary in configuration two, but additional CFD simulations are run with constant heater powers to confirm the same pattern. These observations suggest another important phenomena impacts the flow, which will be discussed in more detail in Chapter 6.

Chapter 4

Utility of Small Scale Models for Buoyancy-Driven Ventilation

As discussed in Chapter 2, small scale models are regularly used to model ventilation in full size buildings. This chapter provides a detailed analysis of the governing equations important in buoyancy-driven flow, reviews the threshold values of the relevant dimensionless numbers, describes the methodology used to explore a Grashof threshold for a simple chimney, and proposes a new Grashof threshold value.

4.1 Dimensional Analysis of Buoyancy-Driven Flows

The governing equations of buoyancy-flows are the conservation of mass, momentum, and energy. Airflow in buildings is considered incompressible, so the conservation of mass is

$$\nabla \cdot \mathbf{v} = 0 \tag{4.1}$$

where $\mathbf{v}$ is the velocity vector. The conservation of momentum is

$$\rho \left\{ \frac{\partial \mathbf{v}}{\partial t} \cdot \nabla \mathbf{v} \right\} = -\nabla p + \mu \nabla^2 \mathbf{v} + \rho \mathbf{g} \tag{4.2}$$

which can be simplified to the steady state form for one dimensional flow where

x is in the vertical direction

$$\rho u\frac{\partial u}{\partial x} = -\frac{\partial p}{\partial x} + \mu\frac{\partial^2 u}{\partial x^2} + \rho g\beta\Delta T \tag{4.3}$$

Finally, the steady state form of the conservation of energy is

$$\rho C_p u\frac{\partial T}{\partial x} = k\frac{\partial^2 T}{\partial x^2} \tag{4.4}$$

As previously shown, these governing equations can be made dimensionless by substituting in the dimensionless variables

$$\bar{u} = \frac{u}{u_{char}}; \bar{v} = \frac{v}{u_{char}}; \bar{x} = \frac{x}{L_{char}}; \theta = \frac{T - T_{char}}{\Delta T_{char}}; \bar{P} = \frac{P}{\rho u_{char}^2} \tag{4.5}$$

Substituting in these dimensionless parameters introduces additional terms, which are collected in dimensionless groups

$$\frac{\partial \bar{u}}{\partial \bar{x}} = 0 \tag{4.6}$$

$$\bar{u}\frac{\partial \bar{u}}{\partial \bar{x}} = -\frac{\partial \bar{p}}{\partial \bar{x}} + \frac{\mu}{\rho u_{char} L_{char}}\frac{\partial^2 \bar{u}}{\partial \bar{x}^2} + \frac{g\beta L_{char}\Delta T}{u_{char}^2}\theta \tag{4.7}$$

$$\bar{u}\frac{\partial \theta}{\partial \bar{x}} = \frac{k}{\rho C_p u_{char} L_{char}}\frac{\partial^2 \theta}{\partial \bar{x}^2} \tag{4.8}$$

These groups are well known and have been previously defined in Chapter 2 as the Reynolds, Archimedes, and Prandtl numbers. Thus, the dimensionless velocity field is a function of the following values [23].

$$u/u_{char} = f\{Re, PrRe, Ar, \bar{x}\} \tag{4.9}$$

In buoyancy-driven flow, u_{char} is generated from a temperature difference. Etheridge and Sandberg introduce a characteristic velocity based on temperature difference that Walker labels as a buoyancy velocity [23] [61]

$$u_{buoyancy} = \sqrt{g\beta L_{char}\Delta T} \tag{4.10}$$

Substituting $u_{buoyancy}$ in for u_{char} in Eq. 4.9 yields

$$\frac{u}{\sqrt{g\beta L_{char}\Delta T}} = f\{\sqrt{Gr}, Pr\sqrt{Gr}, \bar{x}\} \tag{4.11}$$

where the Archimedes number is reduced to unity as shown

$$Ar = \frac{g\beta\Delta T L_{char}}{u^2_{buoyancy}} = \frac{g\beta\Delta T L_{char}}{g\beta\Delta T L_{char}} = 1 \tag{4.12}$$

and the Reynolds number becomes $\sqrt{Gr}$ as shown

$$Re = \frac{u_{char}L_{char}}{\nu} = \frac{\sqrt{g\beta L_{char}\Delta T}L_{char}}{\nu} = \sqrt{\frac{\beta g\Delta T L^3_{char}}{\nu^2}} = \sqrt{Gr} \tag{4.13}$$

If air is used as the working fluid and the left hand side of Eq. 4.11 is multiplied by L^2_{char}/L^2_{char}, the volumetric flow rate $\dot{V}$ appears on the top, and Eq. 4.11 becomes

$$\frac{\dot{V}}{L^2_{char}\sqrt{g\beta L_{char}\Delta T}} = f\{Gr\} \tag{4.14}$$

As Etheridge and Sandberg point out, the requirement for similarity is equal Grashof numbers. However, as previously discussed, equating Gr values is practically impossible for any real model. Thus, recall from Chapter 2 the use of threshold values for the Re and Gr numbers, above which equating the model and prototype values is not important.

4.2 Questionable Origin of Historical Grashof Threshold

The questionable origins of a commonly used Gr threshold of $10^6 - 10^9$ proposed by Etheridge and Sandberg has already been introduced [23]. Baturin's experiment provides justification for this threshold, but his strong language suggesting an absolute

Table 4.1: Measured velocities from Leningrad Institute of Labor Protection used to justify historic Gr threshold [11]

Location	Full-scale velocity $[m/s]$	Predicted full-scale velocity $[m/s]$
door1	1.05	1.29
door2	1.51	1.34
door3	1.37	1.34
door4	1.53	1.29
roof1	1.60	1.34
roof2	1.37	1.38
roof3	1.8	1.47
roof4	1.51	1.57

minimum threshold value is concerning [11]. Working above this Gr value, the author claims, "automatically ensures similarity of the convection pattern" [11]. Not only is an enormous claim made, but the justification for it seems lacking.

The experiment, conducted at the Leningrad Institute of Labor Protection, used a 1/20 scale model to simulate the velocity profiles within a forge measuring 35.5 m long, 17.5 m wide, and 11.1 m tall [11]. The forge used gas fired heating and natural ventilation [11]. One concern arises from the lack of temperature control in the prototype. The prototype heater generated between 576 and 721 kW, resulting in a temperature rise $\Delta T_{prototype}$ between 9.9 and 14 $°C$ [11]. Based on these data the experimenters assumed $\Delta T_{prototype} = 11$, and varied the model heater to create a $\Delta T_{model} = 11.3\ °C$. Their main comparison is made using measured local velocities at eight locations. Four of the velocity measurements are made at the door to the forge, the inlet, and four measurements are made at the roof louvers, the exhaust [11]. The measured full scale velocities are compared to the predicted full scale velocites from the model in Table 4.1.

Although their predicted velocities from the small scale model all agree within 23% of the full scale velocities, their measurements are made rather coarsely and they do not consider the velocity profiles within the forge. They only measured four velocities at both the inlet and exhaust. Furthermore, they only tested a 1/20 scale model under one heater condition, which hardly provides the grounds to establish a

threshold, since they do not show what happens above and below that threshold.

To provide greater confidence in the validity of a Gr value threshold, various scales at various power consumptions must be investigated to show the velocity distributions above and below the proposed Gr threshold. Additionally, a more refined comparison of velocity profiles within the space is needed, rather than a coarse sampling only at the inlet and exhaust. The rest of this chapter describes the methodology used to investigate this Gr threshold and presents the results of this investigation.

4.3 Methodology to Investigate Gr Threshold

The validated CFD models discussed in Chapter 3 are used to simulate a simple chimney at various scales. Temperature and velocity profiles are used to compare the small scale simulations to the full scale simulation to investigate a Gr threshold above which results from small scale simulations resemble full scale results.

The chimney geometry is chosen based on a simplified geometry of the three floor experiment described in Chapter 3. A simple chimney is connected to an entry region in which a rectangular heater heats the air, causing it to rise through the chimney. The exact geometry is shown in Fig. 4-1. Four scales are simulated: full scale, 1/4, 1/10, and 1/20. At full scale, $h_{chim} = 12\ m$, $L_{chim} = 2\ m$, $L_{entry} = 4\ m$, $w_{entry} = 2\ m$, $h_{entry} = 0.72\ m$, the heater length equals 1 m, and the heater width equals 0.59 m. The heater is suspended in the middle of the entrance region. In each of the small scale simulations, these dimensions are multiplied by the appropraite scaling factor, 1/4, 1/10, or 1/20. A range of Grashof numbers is investigated to explore various flows above and below a proposed Gr threshold. Gr values vary between $6.7X10^7$ and $1.4X10^{12}$. The Grashof number is calculated using h_{chim} for the characteristic length because it is the length that most impacts the flow and the temperature difference is taken as the difference in bulk inlet and exhaust temperatures.

The $k\epsilon$ turbulence model is chosen based on its observed accuracy in the small scale experiments and the decreased simulation time compared to the LES model. Grid independence tests indicate the following mesh sizes eliminate differences created from

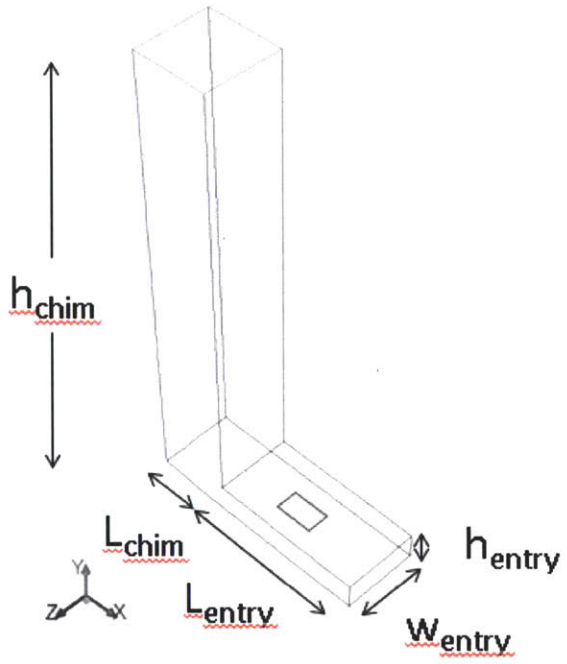

Figure 4-1: Geometry of the simple chimney used to investigate a Gr threshold using CFD simulations. The chimney is based on the three floor experiment previously discussed and contains a rectangular heater in the entry region.

coarse meshes: 140,000 cells for the full scale, 136,000 cells for the 1/4 scale, 138,000 cells for the 1/10 scale, and 138,000 cells for the 1/20 scale model. The mesh density is increased near the heaters and entrance to the chimney. Simulations are run under transient conditions, but are assumed to reach steady state when the bulk exhaust temperature varies less than 0.005 $°C$ for 1000 iterations. Radiation is accounted for using the Surface to Surface radiation model with a residual convergence criteria of 0.001. The enhanced wall function is used with enhanced thermal effects and full buoyancy effects are also considered. Reference, operating, and inlet temperatures are set to 295 K.

4.3.1 Boundary Conditions

All boundaries are modeled as adiabatic surfaces except the inlet, outlet, and heater. A "pressure-outlet" condition at 0 Pa gauge pressure is used to model the inlet and

exhaust openings, which assumes all backflow is normal to the opening. Fluent accounts for the pressure differences that arise from the density gradient over the height of the model. A "porous-jump" condition is also used at each opening to simulate the pressure loss from converging or expanding flow. The same generally accepted pressure loss coefficients of 0.5 and 1 are used for the inlet and outlet respectively [32]. The heater power consumption is simulated using a constant heat flux boundary condition and is varied depending on the desired Gr value.

4.4 Results from Gr Threshold Investigation

One of the major limitations of the study conducted at the Leningrad Institute of Labor Protection is the coarse velocity measurements: only eight are reported, taken at the forge inlet and exhaust [11]. No velocity measurements are made in the occupied space, where velocity distributions are arguably most important because of their direct impact on occupants. In this investigation of a Gr threshold, hundreds of velocities are used in comparing velocity distributions of various models. Furthermore, those velocities are taken from within the chimney, the area of interest in this study.

Velocity distributions are presented in non-dimnesional form as a function of non-dimensional x position within the chimney. Velocities are non-dimensionalized by the appropriate $u_{bouyancy}$ for each case, and the x position is non-dimensionalized by L_{chim}. To illuminate the difference between flows above and below the proposed Gr threshold of $1.2e10$, Figs. 4-2 through 4-4 contain Gr numbers above the treshold and Figs. 4-5 through 4-7 contain Gr numbers below the threshold. The prototype chimney has a $Gr = 7.2e11$, which is included in all figures to provide a comparison.

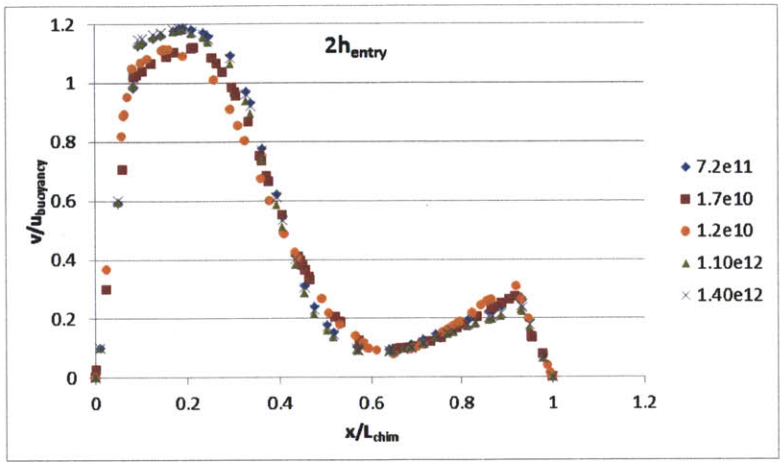

Figure 4-2: Dimensionless velocity plotted against dimensionless x position in the chimney at $z = w_{entry}/2$ and $y = 2h_{entry}$ above inlet for various Grashof numbers above 1.2e10. The full scale prototype chimney has $Gr = 7.2e11$.

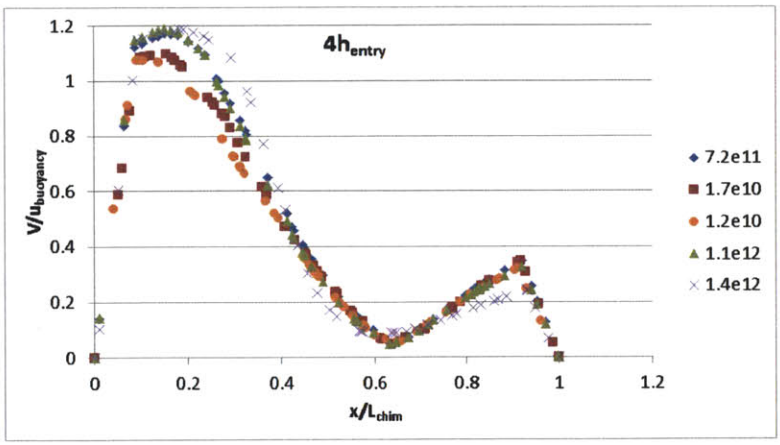

Figure 4-3: Dimensionless velocity plotted against dimensionless x position in the chimney at $z = w_{entry}/2$ and $y = 4h_{entry}$ above inlet for various Grashof numbers above 1.2e10. The full scale prototype chimney has $Gr = 7.2e11$.

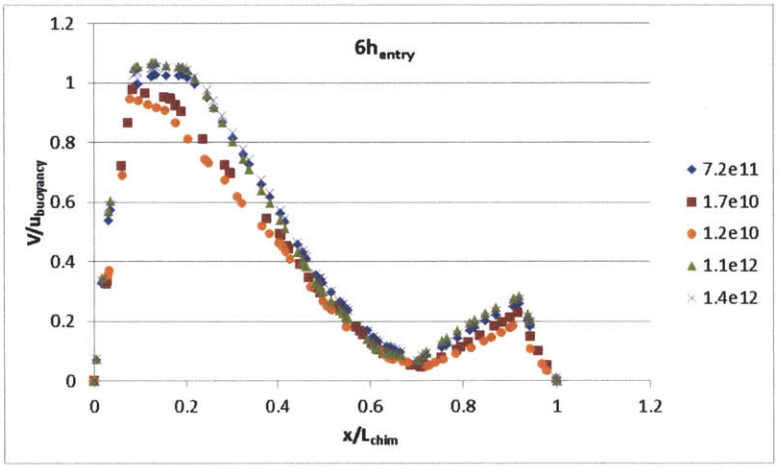

Figure 4-4: Dimensionless velocity plotted against dimensionless x position in the chimney at $z = w_{entry}/2$ and $y = 6h_{entry}$ above inlet for various Grashof numbers above 1.2e10. The full scale prototype chimney has Gr = 7.2e11.

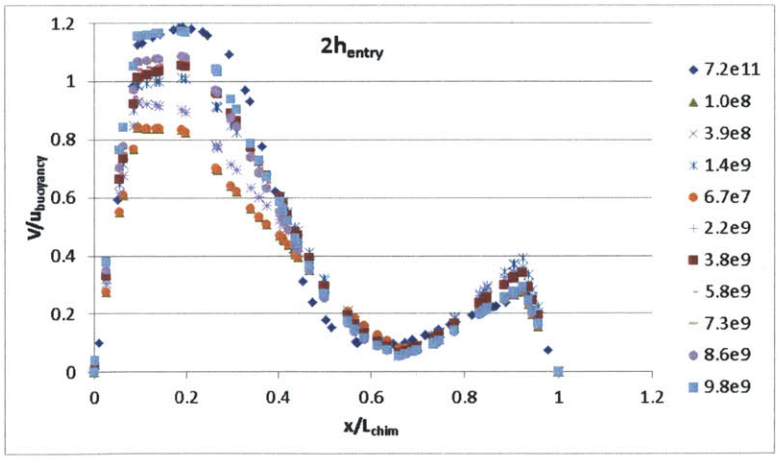

Figure 4-5: Dimensionless velocity plotted against dimensionless x position in the chimney at $z = w_{entry}/2$ and $y = 2h_{entry}$ above inlet for various Grashof numbers below 2.2e9. The full scale prototype chimney has Gr = 7.2e11.

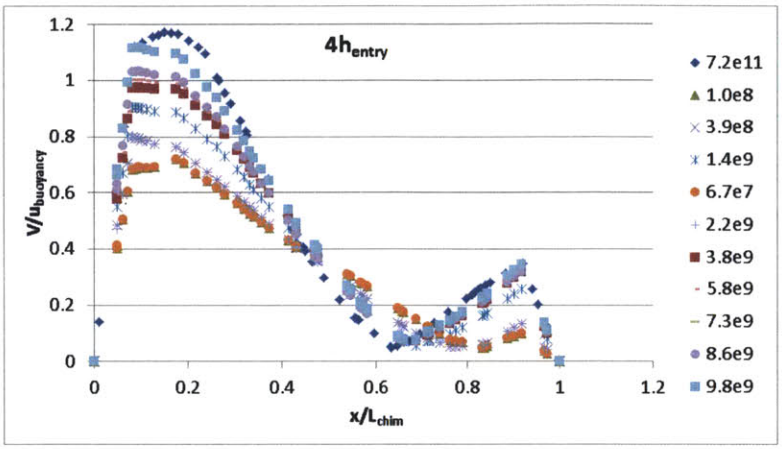

Figure 4-6: Dimensionless velocity plotted against dimensionless x position in the chimney at $z = w_{entry}/2$ and $y = 4h_{entry}$ above inlet for various Grashof numbers below $2.2e9$. The full scale prototype chimney has $Gr = 7.2e11$.

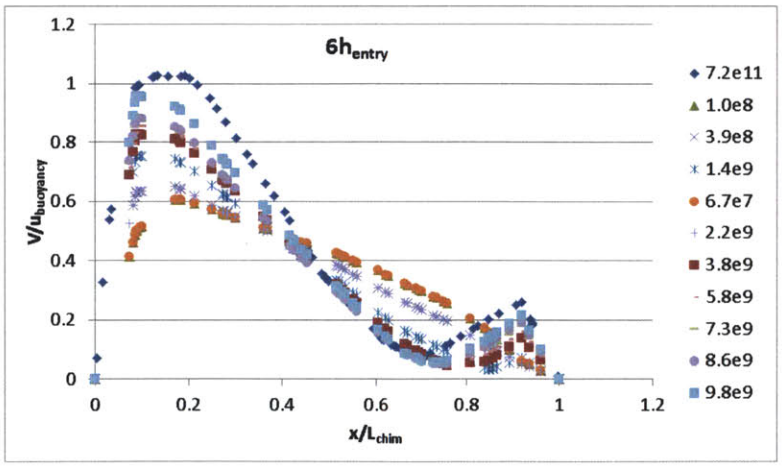

Figure 4-7: Dimensionless velocity plotted against dimensionless x position in the chimney at $z = w_{entry}/2$ and $y = 6h_{entry}$ above inlet for various Grashof numbers below $2.2e9$. The full scale prototype chimney has $Gr = 7.2e11$.

4.5 Discussion of New Proposed Gr Threshold

As shown in Figs. 4-2 through 4-4, the velocity profiles for flows with $Gr > 1.2e10$ all replicate the prototype velocity profile fairly well. The distributions match most closely nearest the inlet to the chimney, and slightly deviate from each other at higher elevations, although all four scale models accurately predict the prototype velocity distribution at $6h_{entry}$ above the inlet to the chimney.

Figs. 4-5 through 4-7 demonstrate that the flows with the smallest five Grashof numbers generate velocity fields that significantly differ from the full scale prototype. The general shape of the curves in Fig. 4-5 seem to mimic the prototype curve, although the model predictions fall significantly below the full scale predictions at some locations. However, the velocity fields diverge even further at higher elevations in the chimney. Fig. 4-7 shows an entirely different profile than the prototype profile. As the Grashof number is increased towards the proposed threshold of $1.2e10$ in Figs. 4-5 through 4-7, the velocity profiles more closely match the full scale profile.

These results provide a strong argument for a Gr threshold of $1.2e10$ for this simple geometry for various reasons. First, velocity predictions are made at a much higher resolution than in previous studies - hundreds of measurements compared to eight in the Leningrad study. Second, velocities are measured within the area of interest instead of only at the boundaries. Third, a wide range of Gr values are considered, $6.7e7 < Gr < 1.4e12$, compared to the single Gr value tested in the Leningrad case. For these reasons, the historical Gr threshold proposed by Baturin of $Gr > 2.8e7$ and suggested by Etheridge and Sandberg is deemed inappropriate for this geometry [11][23].

This threshold value of $Gr > 1.2e10$ should not be taken as an absolute threshold. As Rolloos indicates in his discussion of a Re threshold, the specific geometries and inlet conditions can potentially change this threshold value [49]. Etheridge and Sandberg similarly express their caution to use an absolute threshold value, but advise readers to use the threshold of $Gr > 10^9$ as a conservative value. In the current study, this threshold is not high enough to remove Gr dependence on the flow.

It is therefore recommended that a similar investigation used in this study is conducted for the specific geometry to be used in the scale modelling. If the exact geometry can not be replicated, a simpler, though similar, geometry can be used. If no investigation into the Gr threshold can be conducted, the proposed threshold of $Gr > 1.2e10$ should be used as an absolute minimum threshold value. Further study is needed to see how widely this threshold can be accurately applied to different geometries and inlet conditions.

Chapter 5

Full Scale Experimentation of Buoyancy-Driven Ventilation

CFD modeling has been shown to accurately model a variety of airflow conditions at small scale. This chapter explains the full scale tests conducted at an MIT building that are used both to further validate CFD models and characterize the airflow within a large atrium.

5.1 Motivation for Full Scale Experimentation

Various studies have investigated airflow in atria using CFD models. Awbi conducted a study of a 15 m atrium to evaluate temperature, wind speed, and CO_2 levels within the space [9]. He accounted for solar gains by specifying a constant heat flux on the atrium floor, but failed to compare his CFD model to any experimental data. Gan and Riffat simulated the airflow in a 205 m^2 atrium that is 14.6 m high [28]. Their chief concern was to evaluate the temperatures and airflow rates within the atrium for various opening configurations, but they too provided no experimental verification of their CFD model.

Some recent studies have included experimental comparisons to their CFD models. The full scale experiment at Concordia University mentioned in Chapter 2 was used by Rundle et al. to validate various CFD turbulence models [52]. As previously

discussed, though, the experimental results were quite limited as only nine thermocouple measurements were reported for the entire atrium and boundary conditions were not carefully considered. Streamline trajectories were not measured nor were local velocity measurements made. Furthermore, the atrium was mechanically ventilated through a series of supply and return ducts. This same data was used by Hussain et al. to compare a one-equation model, the Spallart-Allamars, and five two-equation models: $k\epsilon$, $k\epsilon$ RNG, realizable k$-\epsilon$, standard k$-\omega$, and SST k$-\omega$ [31]. They also used data collected from a three story atrium in Ottawa that was mechanically ventilated [35]. Specifically, the first floor was conditioned by four variable air volume ducts, and the second and third floors of the atrium were conditioned by twenty four high velocity supply jets [35]. Hussain et al. found all six models agreed with experimental measurements to within 10%. Very little data is published for full scale atria, so although these results are for mechanically ventilated buildings, they can still help inform the simulation of naturally ventilated atria.

The current full scale experiment seeks to accomplish two purposes. First, it characterizes a large naturally ventilated atrium through temperature readings, airflow measurements, detailed airflow visualization techniques, and particle image velocimetry. Second, these data are used to compare a variety of CFD turbulence models to provide further validation beyond the small scale experiments described in Chapter 3.

5.2 Full Scale Atrium Description

The four story atrium used in this study is the western atrium in the MIT Building E14 and shown in Fig. 5-1. The atrium measures 14.2 m tall, covers an area of 210 m^2, and houses two elevators, which were rarely used during testing. Although the atrium is normally mechanically ventilated, all mechanical systems within the space were shut down during testing. A plan view of the atrium is shown in Fig. 5-2, which highlights the glazed facade in red, elevators in purple, and walls in black. A section view is provided in Fig. 5-3 where the entrance foyer is outlined in blue and the atrium is outlined in green.

Figure 5-1: Photographs of the atrium in building E14 at MIT used in the current full scale experimentation.

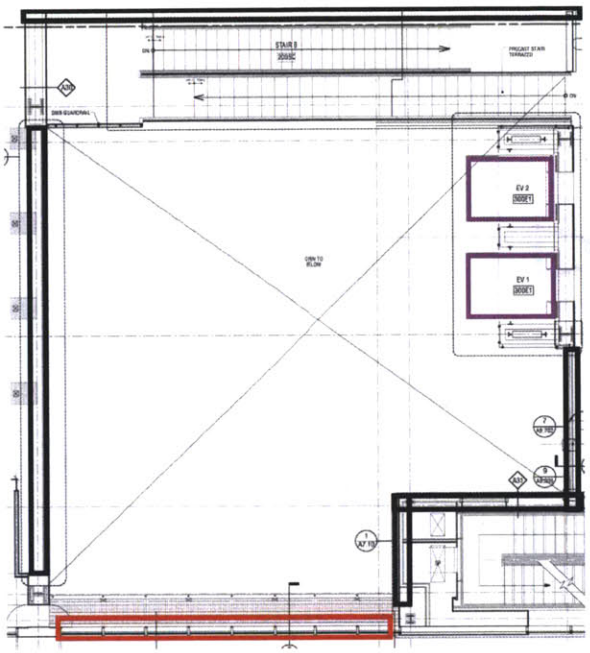

Figure 5-2: Plan view of atrium with glazed facade in red box, elevators in purple boxes, and walls in black boxes.

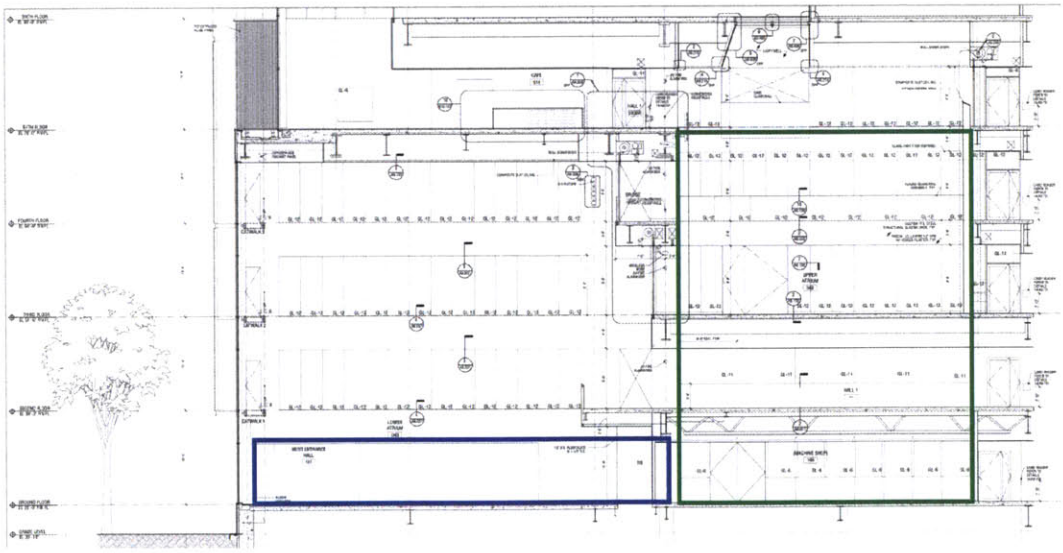

Figure 5-3: Section view of the single-story foyer (blue) and atrium (green).

A door on the ground floor is propped open to provide an opening to the atrium via a foyer, and a doorway on the third floor of the atrium provides a second opening. This doorway eventually leads to the outdoors via a rooftop deck on the sixth floor. Both doorways are shown in Fig. 5-4.

Figure 5-4: Photographs of the two openings into the atrium. (left) A single door on the ground floor is propped open during the experiment and (right) the third floor doorway outlined in green is left open. The fire door highlighted in pink along the ceiling (right) is closed during the experiment.

All other openings to the atrium are sealed off using either fire doors or plastic tarps. Specifically, the fire doors on the third and fourth floors that overlook the atrium were closed. The open fire door on the third floor is shown in Fig. 5-4. Polyethene 4 *mm* thick flame retardent tarps were used for fire safety purposes to block the following openings: first floor SE opening into atrium, first floor NE opening into atrium, second floor railing near staircase, second floor SE corner, and second floor NE corner. Fig. 5-5 shows the mounted tarps.

The atrium is primarily heated by two light banks. A permanently installed bank of 22 lights rated at 38 W each is installed in the foyer, while a temporary bank of

Figure 5-5: Mounted polyethelyne 4 mm flame retardant tarp used to seal various openings to atrium. The NE opening on the first and second floor (left) and SE opening on the first and second floor (right) are shown.

sixty 100 W incandescent bulbs is installed on the ground floor in the middle of the atrium. The bulbs in the temporary bank are hung approximately 0.46 m (1.5 ft) from each other along a total of 5 PVC pipes, which are separated by 0.61 m (2 ft). Both banks of lights are shown in Fig. 5-6.

5.2.1 Atrium Instrumentation

The airflow within the ventilation shaft is characterized in three ways through temperature measurements, airflow measurements, and a flow visualization technique.

Temperature measurements are made at 45 locations within the atrium using sensors created by Schneider Electric and various students of Joseph Paradiso [60]. A detailed description of the development of the temperature sensing network is provided in Ashley Turza's undergraduate thesis [60]. The specific temperature sensor

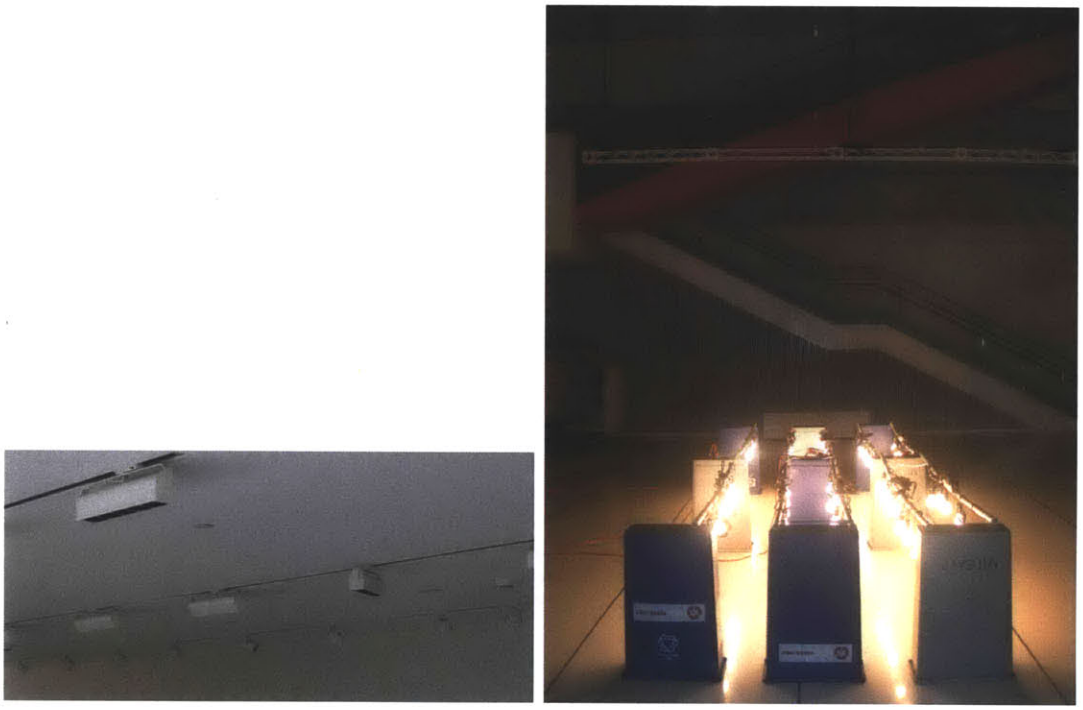

Figure 5-6: (left) Permanent light bank of twenty two 38 W lights installed in the foyer. (right) Temporary light bank of sixty 100 W light bulbs set up in the middle of the atrium.

used is National Semiconductor part number LM35CZ, which has a stated accuracy of 0.5 $°C$ at 25 $°C$ [42]. The temperature sensors are circled in green in Fig. 5-7 and have a sampling rate of 3:40 min.

Volumetric flow rates are measured at the ground floor door in accordance with ASHRAE Standard 111-2008 using the equal area method for the entrance to a rectangular duct [8]. Velocity measurements are to be taken at 42 points at the door using a Graywolf AS-201 hotwire anemometer, which has a stated accuracy of $+/-$ 3% rdg $+/-$ 0.015 m/s. However, the anemometer was damaged during part of the testing and only 27 measurements were made. These velocities are averaged according to ASHRAE standard 111-2008 and used to determine the flow rate. The measurements are made flush with the door opening to increase the liklihood of unidirectional flow.

The same neutrally−buoyancy bubble machine is used as the one mentioned in Chapter 3, the SAI^{TM}Model 5 Bubble Generator. Flexible tubing directs the bubbles from the outlet tube to the desired location within a space and is always mounted or-

Figure 5-7: Photograph of the atrium with some of the 45 temperature sensors circled in green.

thogonally to the bulk direction of the flow under consideration. Bubbles are injected at multiple locations to visualize the airflow throughout the atrium.

5.3 Full Scale Experimental Procedure

The experiment was conducted over night on Friday, August 18, 2011 for two reasons. First, an over night experiment removes solar gains, which neccesitate additional assumptions when modeling the space. Second, the disruptive experimental activities are required to take place when the building is least occupied. Activities like turning off the HVAC system, disarming the fire alarm system, and blocking many hallways with plastic tarps present too large a danger during regularly occupied hours. Me-

chanical and fire-safety technicians monitor the atrium during the entire experiment, which runs for four hours. This time is sufficient to allow temperatures in the atrium to reach quasi-steady values, as will be demonstrated in the results. The ground floor door is closed for the first hour of the experiment to reduce the airflow rate through the atrium and allow a greater temperature difference between indoor and outdoor temperatures. Temperatures are logged at a sampling rate of 3 min and 40 s for the duration of the experiment, while both airflow measurements and visualizations are made at various points after the quasi steady state has been achieved.

5.4 CFD Model Description

The same turbulence models used in the small scale experiment are used to model the full scale atrium. Specifically, the $k\epsilon$, $k\epsilon$ RNG, and large eddy simulation (LES) turbulence models are compared. The atrium geometry is exactly matched in the mesh except for the elevator cars, a small support column at the end of the foyer, and the railing on the first floor ramp, which are all ommitted. The five rows of twelve incandescent bulbs in the 6 kW array are modeled using five bars that are 10 cm wide, 5 cm thick, and 5 m long, which is the measured length of the actual arrays used in the experiment. Fig. 5-8 depicts the geometry used for all CFD simulations. Grid independence tests indicate mesh sizes of 1,140,000 cells are sufficient. The mesh density is increased near the heaters and along the narrow hand rails on the second floor ramp. Simulations are run under transient conditions, but are assumed to reach steady state when the bulk exhaust temperature varies less than 0.138 $^{\circ}C$ for 1000 iterations. Radiation is accounted for using the Surface to Surface radiation model with a residual convergence criteria of 0.001. The enhanced wall function of the $k\epsilon$ and $k\epsilon$ RNG model is used with enhanced thermal effects and full buoyancy effects are also considered. The Smagorinsky-Lilly subgrid-scale model is used in the LES model. Reference and operating temperatures are set to 293 K.

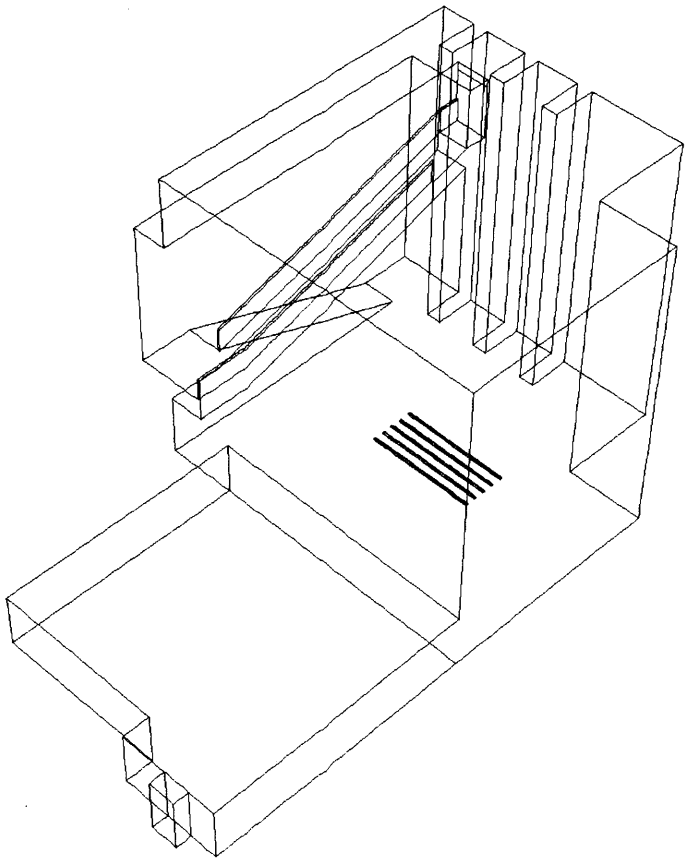

Figure 5-8: Simplified geometry used for CFD simulations of the atrium, which exactly matches the atrium geometry except for the elevator cars, a small support column at the end of the foyer, the railing on the first floor ramp, and the five rows of twelve incandescent bulbs in the 6 kW array.

5.4.1 Boundary Conditions

The thermal properties of all materials used in the experimental model are used in the CFD model and summarized in Table 5.1. The exterior walls are modeled with glass and the external boundary condition in Fluent of "Convection," which uses a specified constant heat transfer coefficient of 10 W/m^2K and a specified external temperature of 296 K. The foyer ceiling is modeled as gypsum board with a constant heat flux boundary condition of 6 W/m^2 to account for the permanent array of lights. The five bars used to model the temporary light array use a constant heat flux boundary condition. Each bar outputs a specified 827 W/m^2 of power, such that the combined

Table 5.1: Summary of thermal properties of materials in used in the atrium CFD simulations

Material	Density $[kg/m^3]$	Specific Heat $[J/kgK]$	Conductivity $[W/mK]$
Dry wall	2320	1138	0.5
Glass	2579	840	1.0
Aluminum	2719	871	202

power output of all twelve bulbs on each array (1.2 kW) is assumed to be evenly distributed across each bar, which is modeled with aluminum in the simulations. The boundary condition at the third floor door is a specfied uniform flow rate of 1.47 m^3/s into the atrium, which is the experimentally measured flowrate into the atrium. More information on this measured flowrate is presented in the Results section. A "pressure-outlet" condition at 0 Pa gauge pressure is used to model ground floor door, where the airflow is observed leaving the space.

5.5 Results from Physical and CFD Models

The measured volumetric flow rate leaving the atrium through the ground-floor door is 1.47 m^3/s +/− 0.087 m/s, which results in 1.78 ACH. Flow visualization confirms the air flows out of the building on the ground floor. Fig. 5-9 shows the atrium temperatures at the begining of the experiment with identifying features of the atrium while Fig. 5-10 shows the evolution of temperatures in the atrium over the course of the experiment. The heat source is turned on at 9 : 30 pm and the quasi steady state temperatures are reached by 1 : 30 am, at which point temperatures vary less than 0.5 $°C$, the stated accuracy of the thermocouples, over 30 minutes.

CFD predicted temperature contours are compared to the quasi steady state experimental temperatures for each of the three turbulence models in Figs. 5-11 through 5-13. Experimental temperatures are carefully located on the predicted contours to correspond to their physical location within the atrium. Brown circles represent temperature sensors that malfunctioned during the experiment.

In addition to predicted temperature contours, predicted velocity fields are also

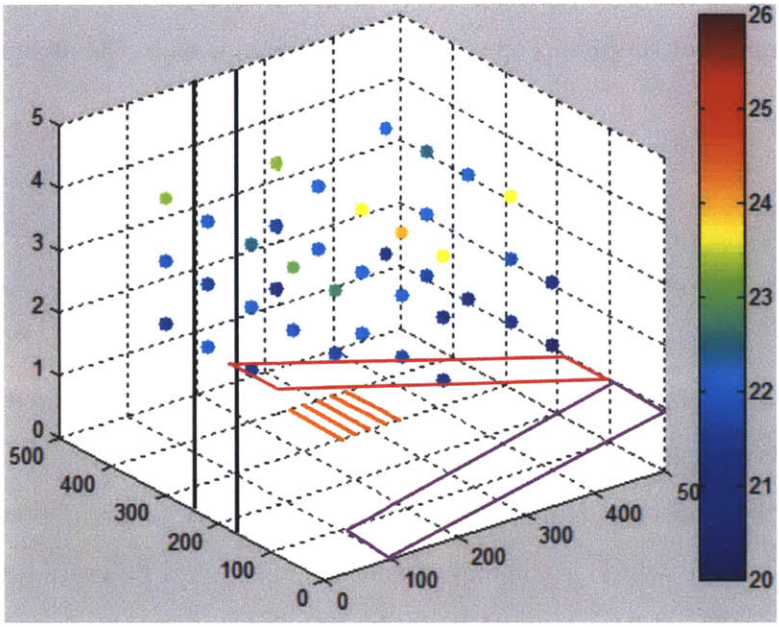

Figure 5-9: Measured atrium temperatures in $°C$ at the beginning of the experiment with identifying features of the atrium. The purple and light pink ramps correspond to the staircases in the atrium, the solid black vertical lines correspond to the elevators, and the five orange lines correspond to the temporary heat source.

presented for each of the turbulence models in Figs. 5-14 through 5-22.

All of the flow visualization is captured in video, and thus can not be easily published in this dissertation. However, to visualize the airflow directly above the heaters, the video has been parsed into a series of still images that are presented in Fig. 5-23. Each consecutive image is separated by 0.04 s and the final image is editted to include arrows that indicate the direction and distance particular bubbles have traveled in 0.2 s. A comparison to these experimentally observed pathlines is provided in Fig. 5-24, which plots the air pathlines as predicted by the LES CFD model.

The experimentally observed bubbles are also used to calculate the velocities of twenty bubbles by tracking the bubble position over time. Fig. 5-25 shows the average velocity of these bubbles in which the first ten bubbles were tracked for 0.9 s and the second ten were tracked for 0.6 s. To minimize the error introduced by bubbles moving away or towards the camera, only bubbles with a constant diameter over tracked time are considered. CFD predictions of air velocities in the same region in

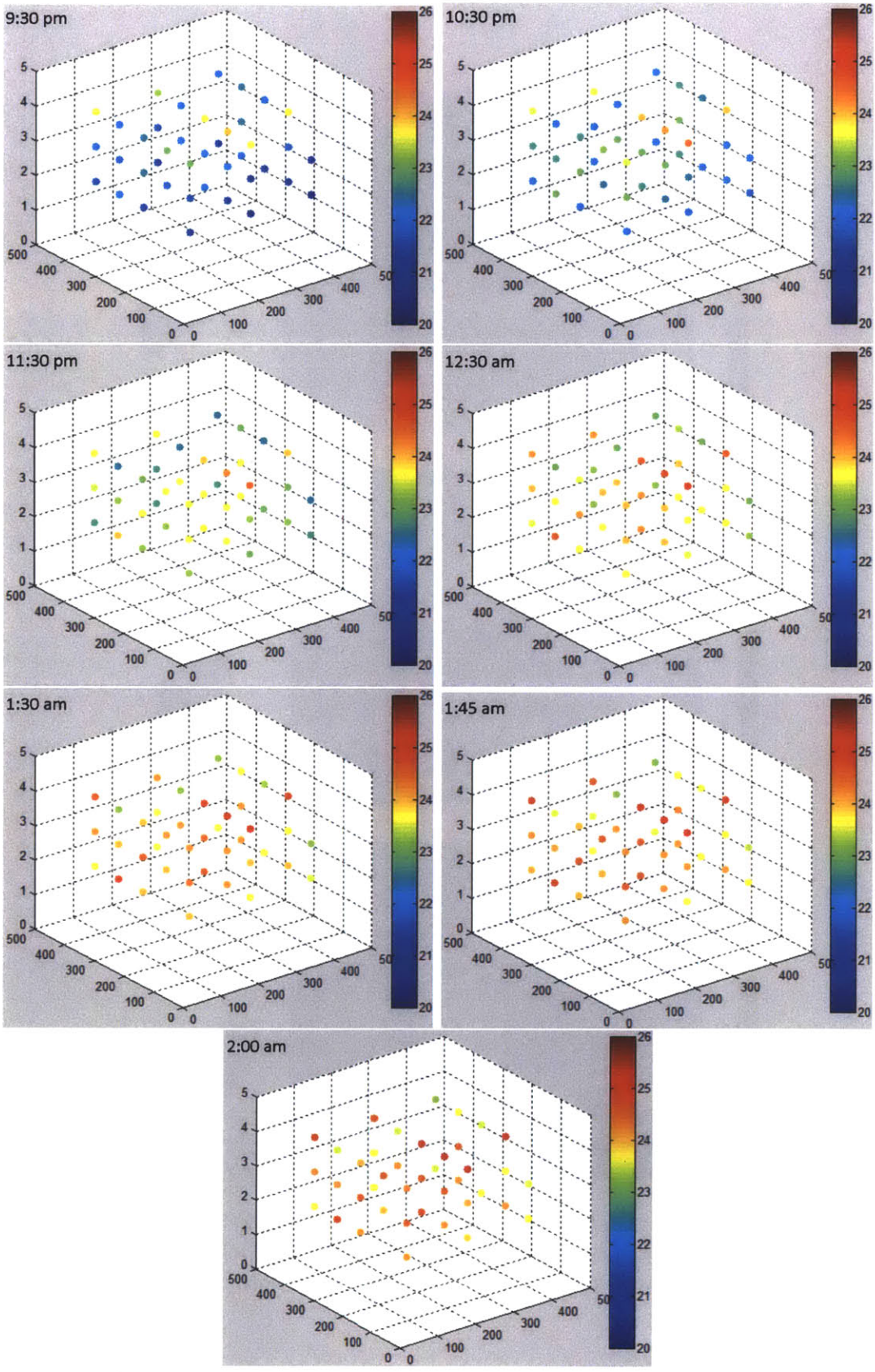

Figure 5-10: Measured atrium temperatures in $/circC$ at various times throughout the experiment.

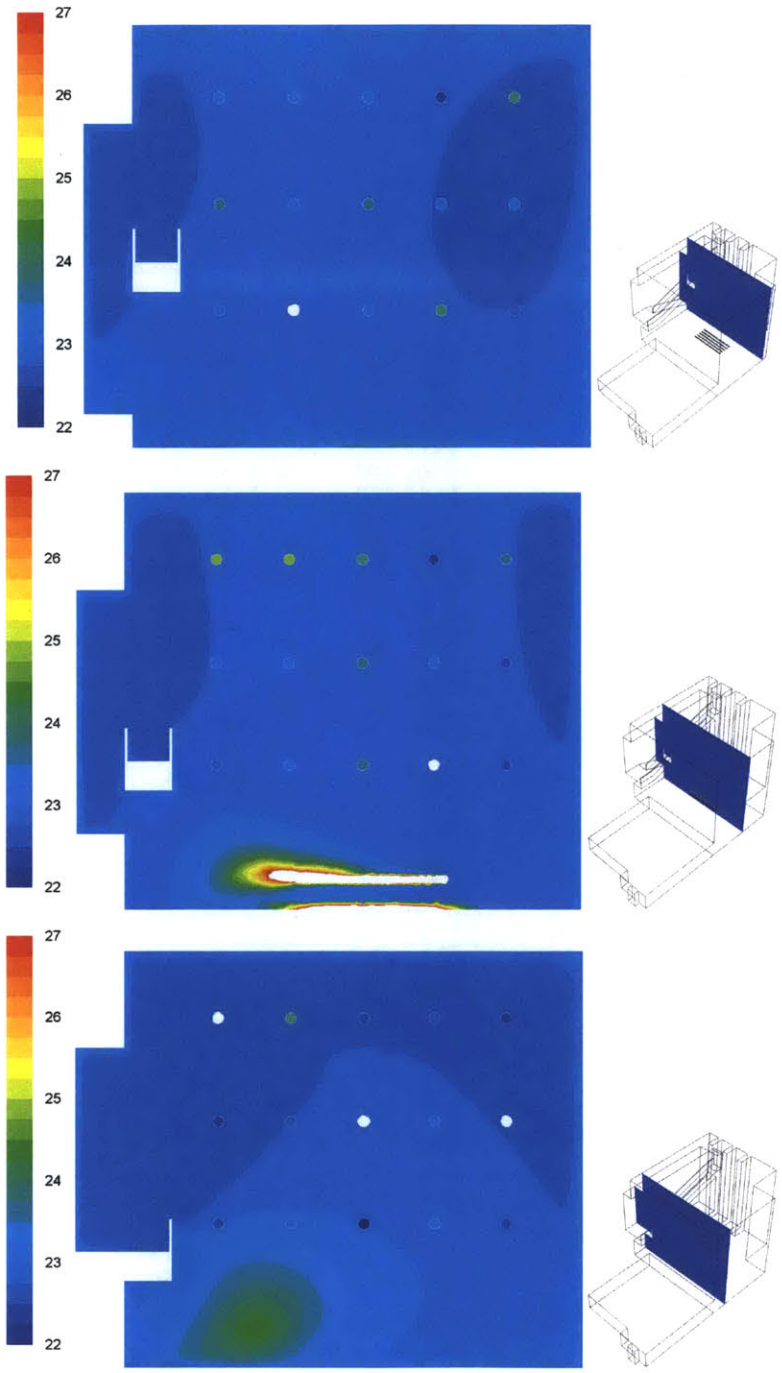

Figure 5-11: Temperature contour for the k-ϵ turbulence model in $°C$ at $z = 5.3, 9$ and 12.8 m for the top, middle, and bottom images respectively. Small circles are shaded according to the measured temperature at that location. White circles correpond to faulty sensors.

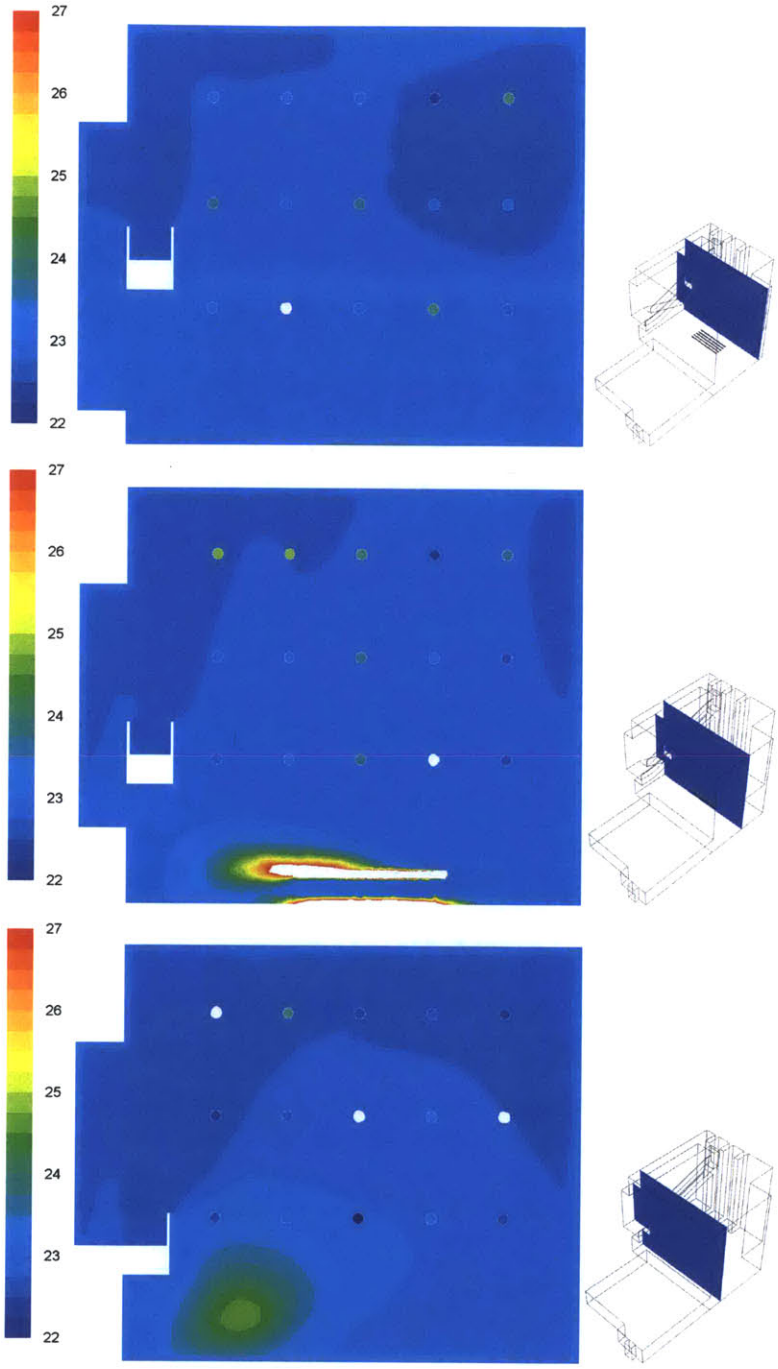

Figure 5-12: Temperature contour for the k-ϵ RNG turbulence model in $^{\circ}C$ at $z = 5.3, 9$ and 12.8 m for the top, middle, and bottom images respectively. Small circles are shaded according to the measured temperature at that location. White circles correpond to faulty sensors.

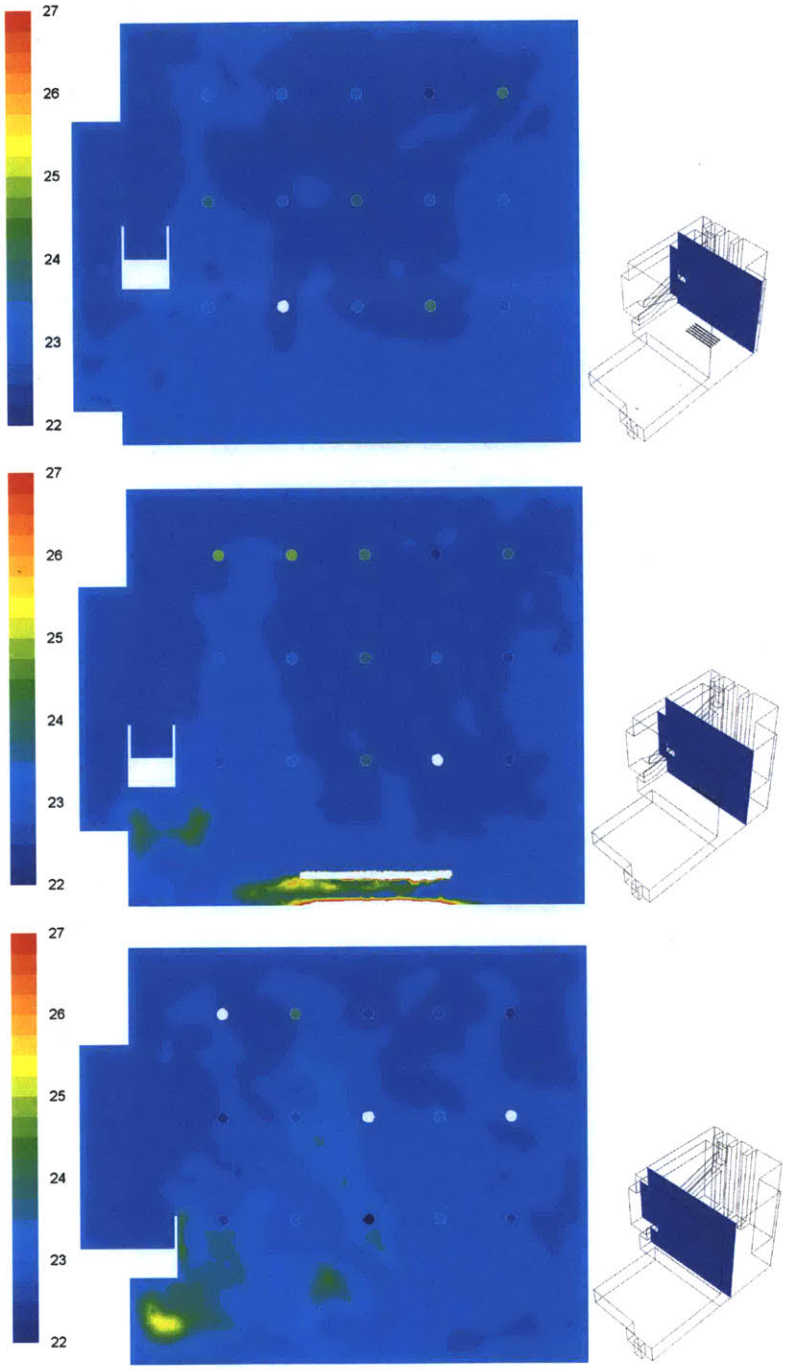

Figure 5-13: Temperature contour for the LES turbulence model in $°C$ at $z = 5.3, 9$ and $12.8\ m$ for the top, middle, and bottom images respectively. Small circles are shaded according to the measured temperature at that location. White circles correpond to faulty sensors.

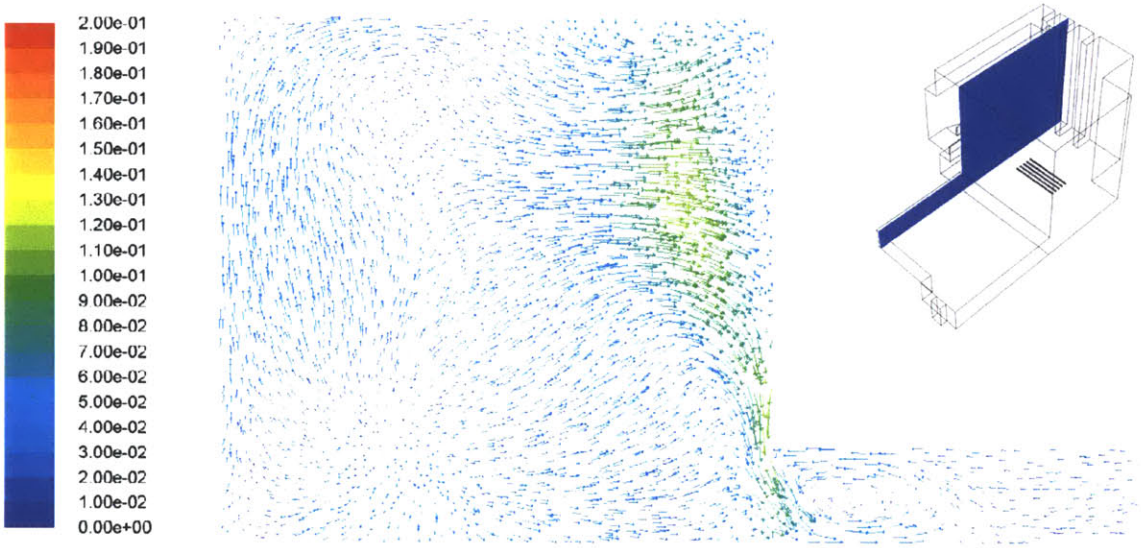

Figure 5-14: Velocity field in m/s at $x = 5$ for the k-ϵ turbulence model.

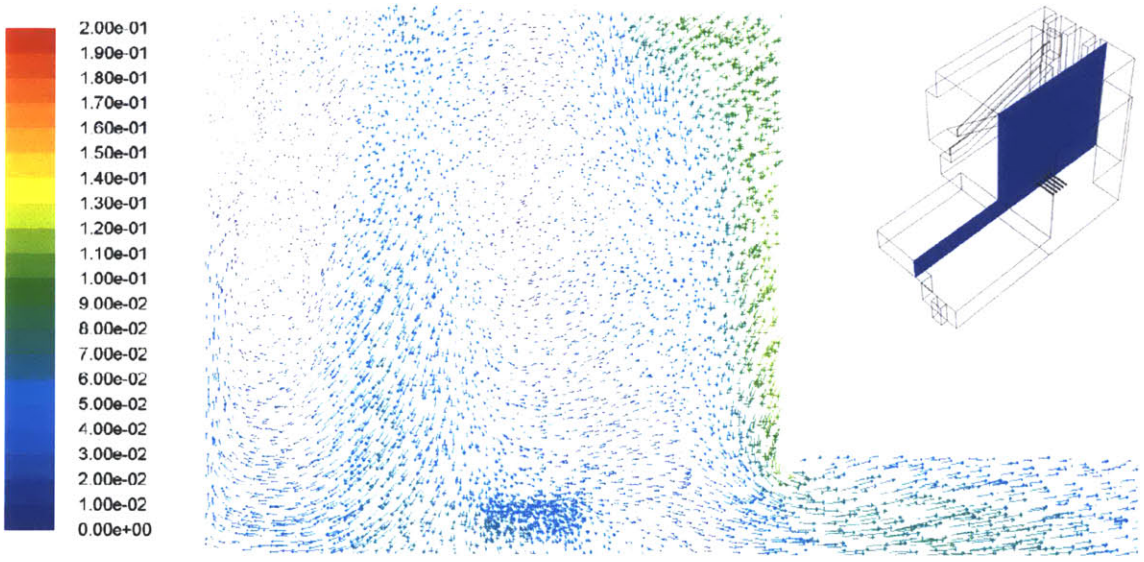

Figure 5-15: Velocity field in m/s at $x = 10$ for the k-ϵ turbulence model.

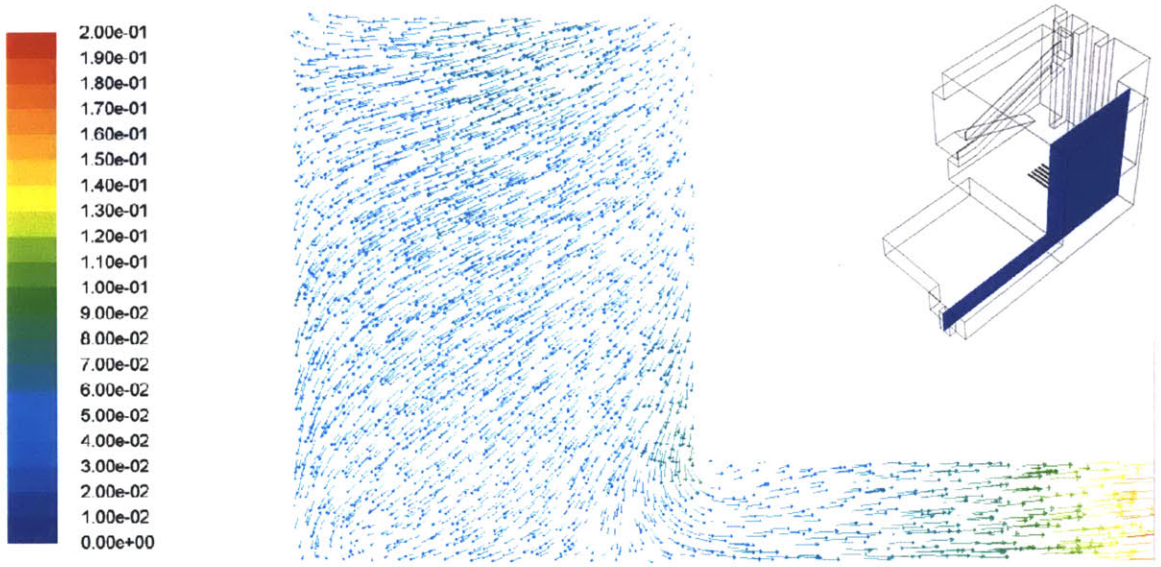

Figure 5-16: Velocity field in m/s at $x = 15$ for the k-ϵ turbulence model.

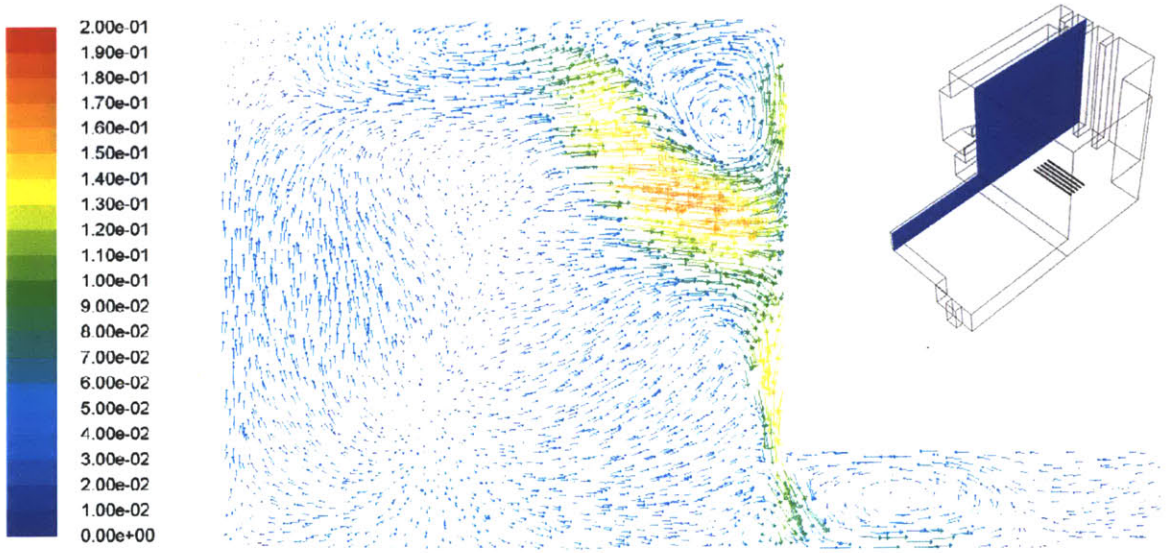

Figure 5-17: Velocity field in m/s at $x = 5$ for the k-ϵ RNG turbulence model.

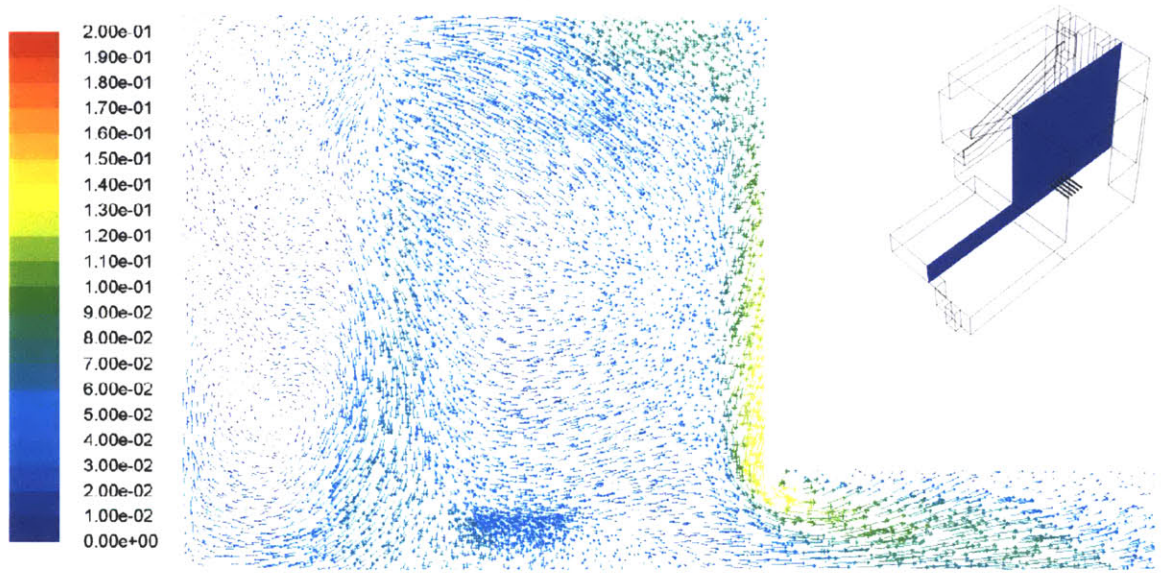

Figure 5-18: Velocity field in m/s at $x = 10$ for the k-ϵ RNG turbulence model.

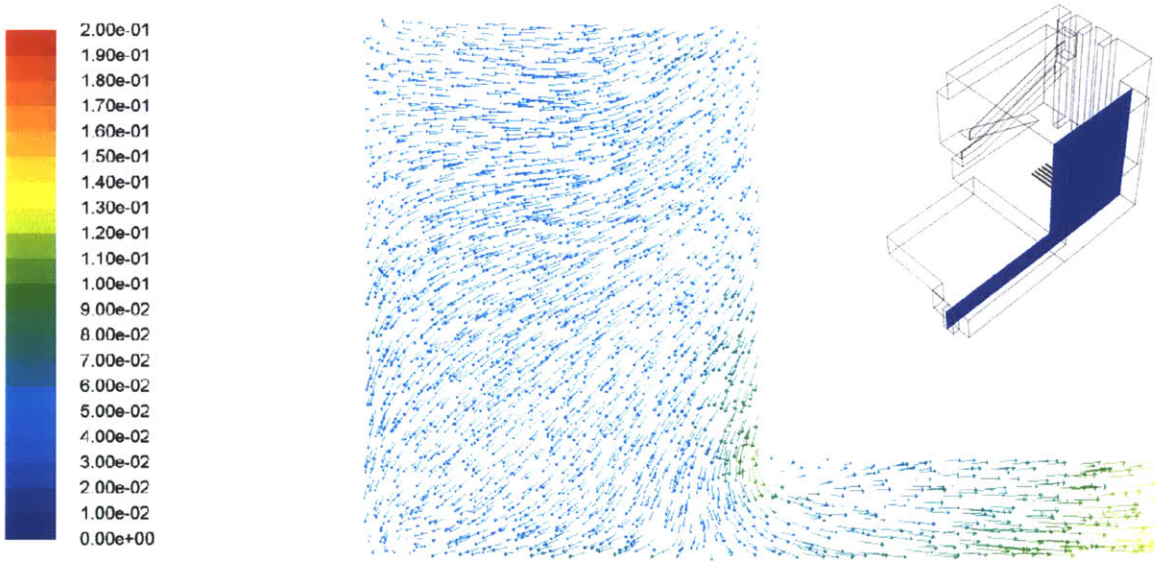

Figure 5-19: Velocity field in m/s at $x = 15$ for the k-ϵ RNG turbulence model.

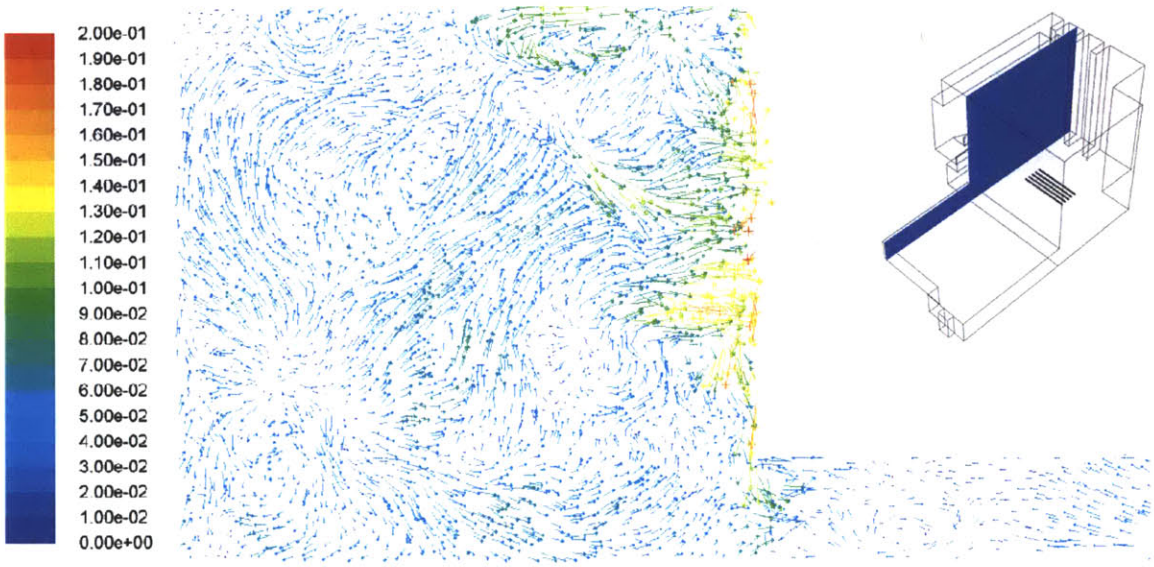

Figure 5-20: Velocity field in m/s at $x = 5$ for the LES turbulence model.

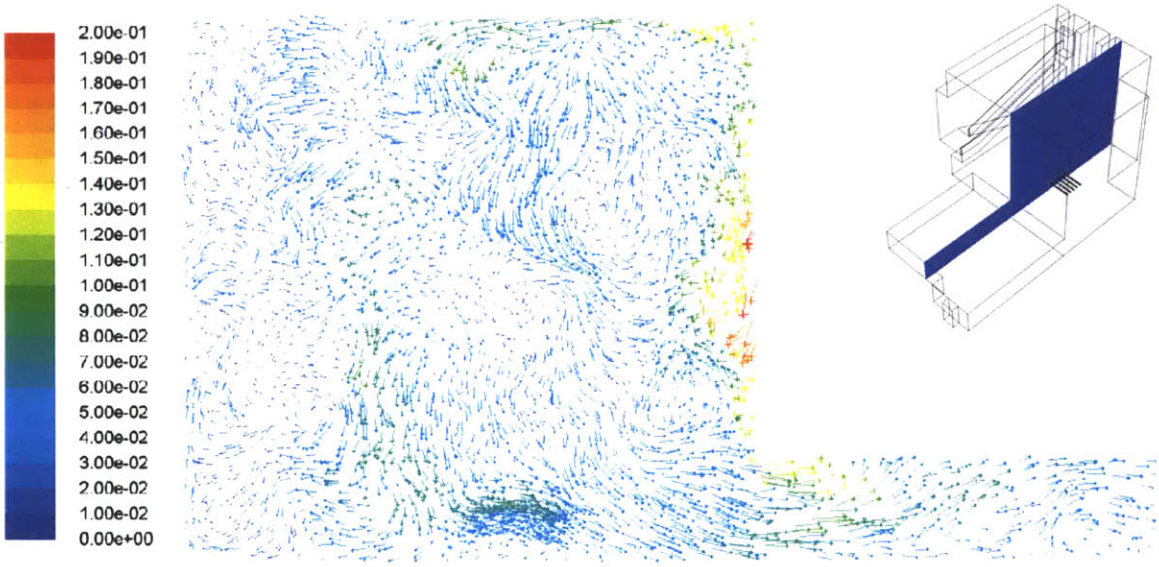

Figure 5-21: Velocity field in m/s at $x = 10$ for the LES turbulence model.

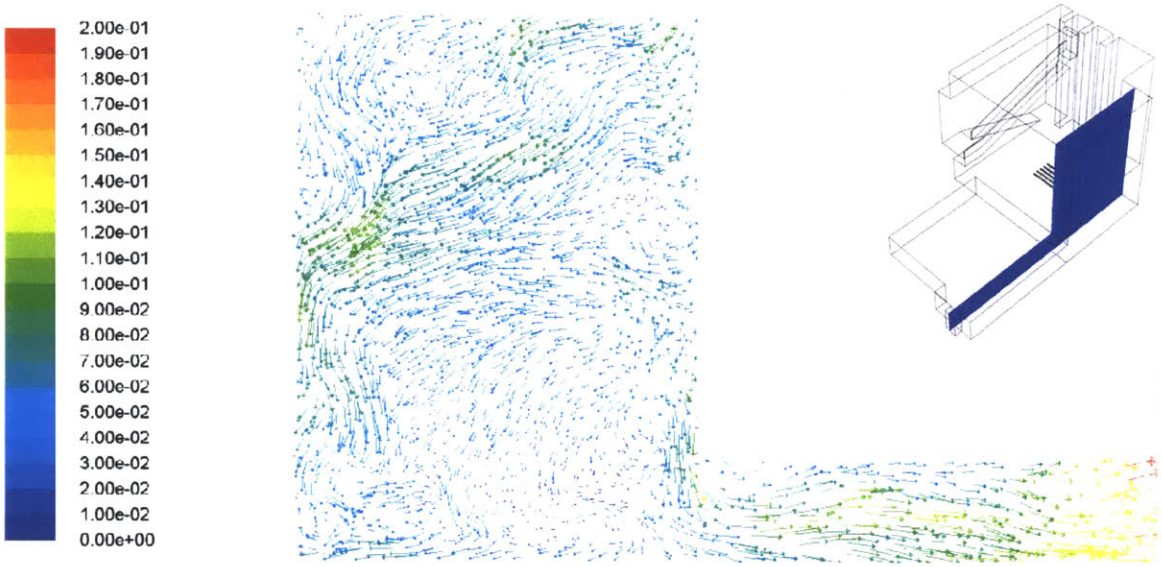

Figure 5-22: Velocity field in m/s at $x = 15$ for the LES turbulence model.

which bubbles are tracked are shown in Fig. 5-26

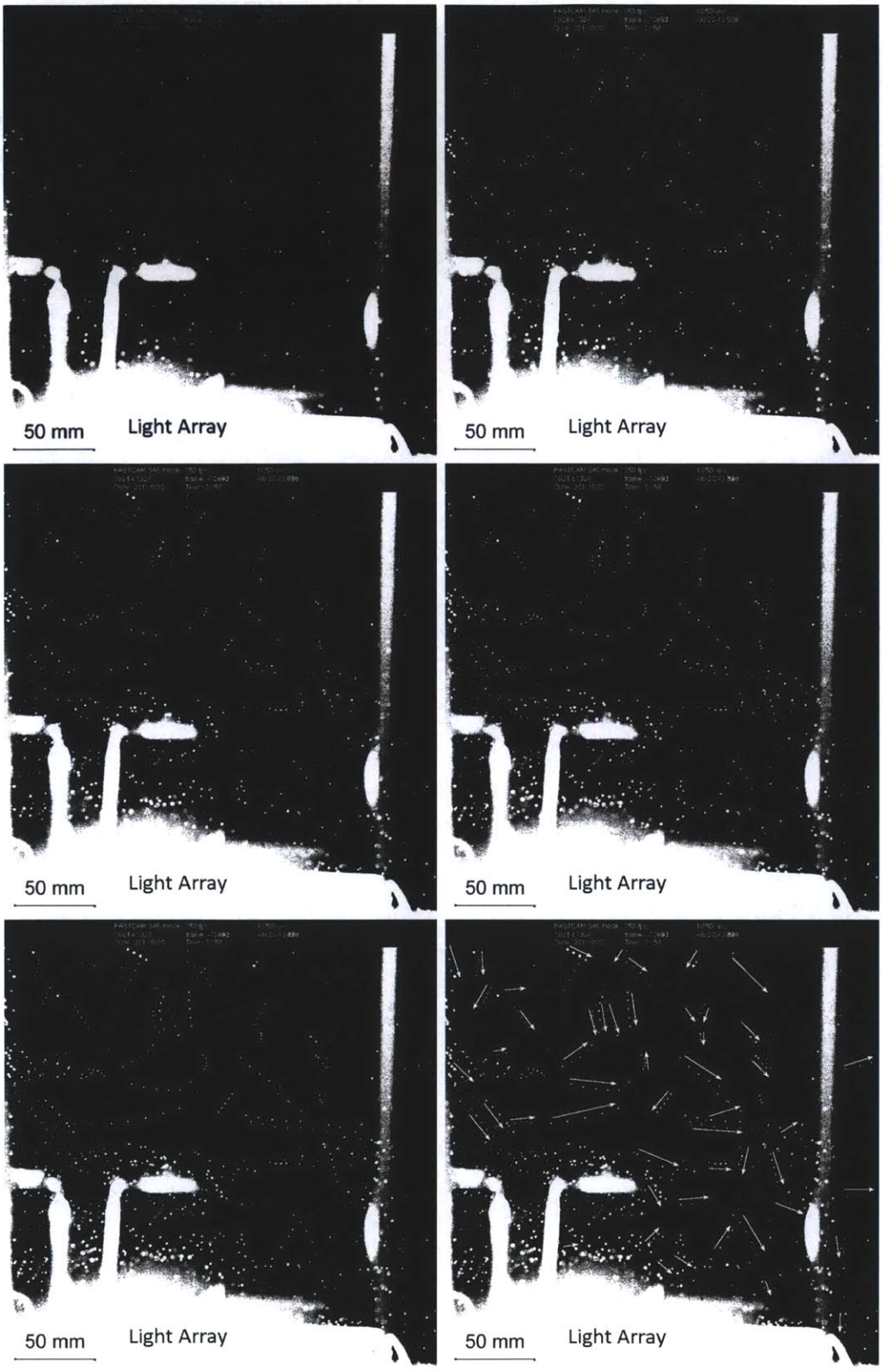

Figure 5-23: Five consecutive images above the middle light array separated by 0.12 s overlaid on each other. Arrows on the final image are drawn to indicate airflow direction and distance by a bubble over 0.48 s. Camera is positioned near stairs facing the glazed facade. Large white areas are artifacts of the video recording process.

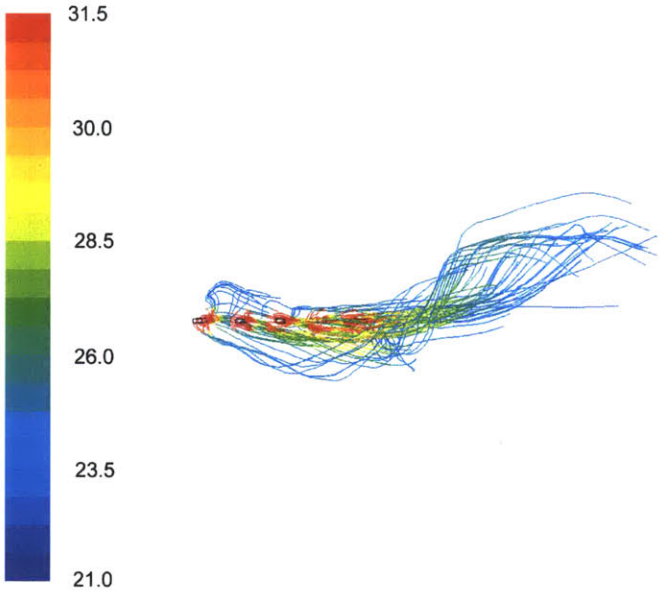

Figure 5-24: Simulated air pathlines near the 6 kW light array from the LES turbulence model colored by temperature in $°C$. The view is oriented similarly to the experimentally measured pathlines such that the glazed facade is behind the array of lights.

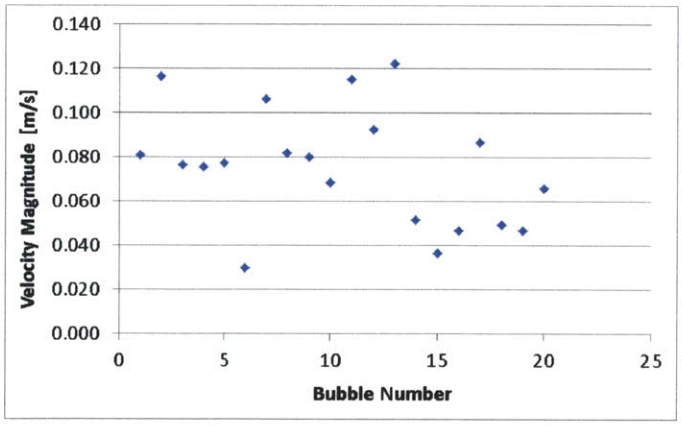

Figure 5-25: Experimentally calculated velocities of neutrally-buoyant bubbles, which provide an approximation for the local air velocities. Bubbles 1-10 are tracked for 0.9 s and bubbles 11-20 for 0.6 and only bubbles with a constant diameter are considered to minimize the error introduced by bubbles moving away from the camera.

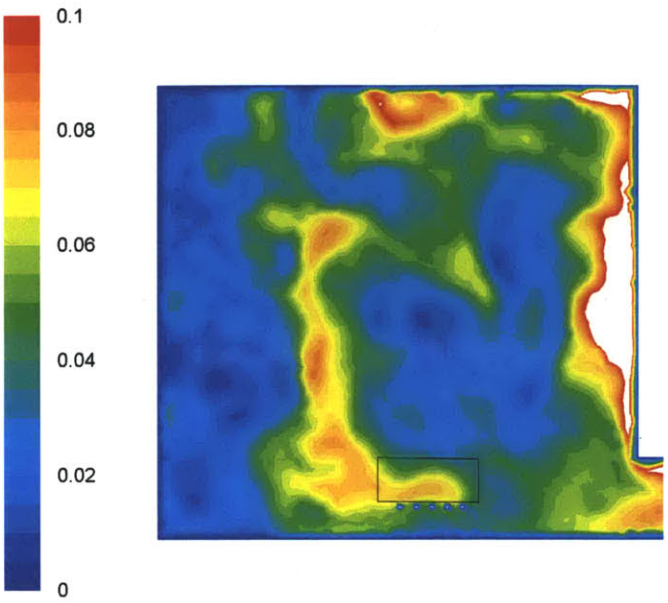

Figure 5-26: Simulated air velocities in m/s above the heater using the LES turbulence model that provide a comparison to measured velocities reported in Fig. 5-25. The black box outlines the general area in which the velocity measurements are made.

5.6 Discussion of Experimental CFD Model Results

A significant result of the experiment is the observed downward flow through the atrium, especially directly above the 6 kW light array. Experimental temperatures in Fig. 5-10 indicate well-mixed conditions within the atrium, with the largest temperature difference between sensors of roughly 2 $°C$. Furthermore, a rising plume does not form over the light array in the middle of the atrium, but rather the interial effects of the air entering through the third floor door overpower the buoyancy effect of the temperature difference created by the lights. CFD simulations predict the same behavior in all three turbulence models. Two factors contributed to this downward flow. First, the openings to the outside on the sixth floor were facing a strong wind during the night of the experiment. This wind created a high pressure at these doors, which helped drive air down through the atrium. Secondly, a wing of the building that is connected to the upper floors of building E14 was air conditioned during the

experiment. Although this wing was outside the control volume of the atrium, the high pressure created by the wind at the sixth floor doors likely drew some of the conditioned air down through the building into the atrium. These two factors led to the use of the specified flowrate boundary condition, which accounts for the flow direction and any mixing between the outdoor and conditioned air. This boundary condition imposes the correct flowrate at the boundary as measured in the experiment, which eliminates the comparison between predicted and measured flowrates as was made in the small scale experiments in Chapter 3. However, comparisons between the measured and predicted temperature distributions and localized airflow directions within the atrium are still made.

The airflow visualization technique was shown to be an effective method for visualizing airflow within a buoyancy-driven naturally ventilated space. Although the SAI^{TM}Model 5 Bubble Generator has been used for numerous other airflow visualizations in buildings, it has not yet been demonstrated in a buoyancy-driven naturally ventilated building [55][34][5][56][48]. The technique clearly demonstrates the downward bulk flow direction through the atrium that allows for proper boundary conditions to be specified. Furthermore, the technique illustrates bubble pathlines as shown in Fig. 5-23 and can be used as a particle image velocimtry (PIV) technique to measure local air speeds as shown in Fig. 5-25.

Another contribution of this work is the full-scale validation of various CFD turbulence models in a buoyancy-driven naturally ventilated atrium. Figs. 5-11 through 5-13 illustrate the agreement between CFD predicted and experimentally measured temperatures. The relatively uniform temperature distribution is also predicted by the CFD models. Local airflow direction is also compared above the heater where both experimental observations and CFD predicted pathlines confirm a downward flow towards the first floor doors as shown in Figs. 5-23 and 5-24. Lastly, the PIV technique is used to measure local air speeds above the heater which varied between 0.030 and 0.123 m/s and agree with the predicted velocity magnitudes shown in Figs. 5-15, 5-18, and 5-21.

Chapter 6

Increased Flowrates from Smaller Ventilation Shafts through the "Ejector Effect"

6.1 Motivation for Investigation of "Ejector Effect"

Recall the results from the small scale experiments that demonstrate upper floors can obtain a higher flow rate than lower floors under the proper conditions. Configuration two, which used floor-to-ceiling openings from each takeoff duct to the chimney and is illustrated in Fig. 3-8, led to a measured flowrate of $0.021 +/- 0.0063\ m^3/s$ on the third floor compared to a flowrate of $0.018 +/- 0.0058\ m^3/s$ on the second floor. CFD simulations predict a similar trend. However, this observation suggests the presence of an important phenomena unaccounted for in analytical models such as Eq. 2.5 and Eq. 2.7, which predicts higher flowrates for lower floors if all other parameters are held constant. This chapter describes the exploration of this phenomena, termed the "ejector effect," using validated CFD models and small scale experiments. A suggested method is also proposed for accounting for the effect in airflow network tools.

6.2 Methodology of Investigation of "Ejector Effect"

To ensure the observed "ejector effect" is not just an artifact of the particular geometry and conditions of the small scale experiments conducted, the investigation begins with CFD simulations of a full scale three story office building. The building is cooled by buoyancy-driven natural ventilation through a single ventilation shaft. CFD simulations are then used to investigate the flow through a single chimney to demonstrate the effect in a simplified geometry. Finally, the physical small scale model described in Chapter 3 is altered to demonstrate this "ejector effect" in additional configurations.

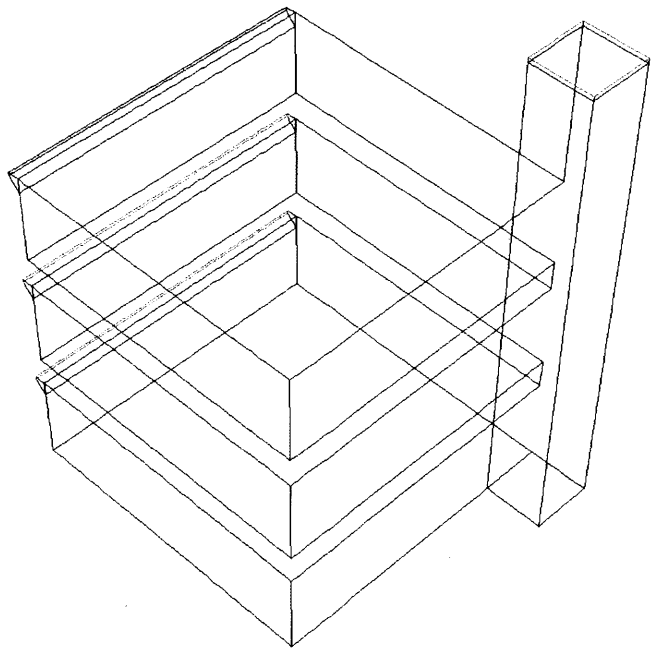

Figure 6-1: Geometry of full-scale office building used in the investigation of the "ejector effect."

6.2.1 Three Floor Office Building

The main objective of simulating a full scale office building is to confirm if the "ejector effect" is predicted to occur in a typical office building and is not simply an artifact of

a small-scale experiment. The building, shown in Fig. 6-1, has three identical floors, each 10 m by 10 m by 4 m high, ventilated through a single ventilation shaft. A drop ceiling of 1 m is used, which limits the actual floor-to-ceiling height to 3 m. A narrow 1 m^2 opening flush with the ceiling on the facade opposite the shaft allows outdoor air to enter the space. Floor-to-ceiling openings from the space to the shaft allow air to exit through the 2 m by 2 m exhaust opening at the top of the shaft. The shaft cross-sectional area is varied throughout the simulations.

CFD Model Description

The same validated CFD modeling procedure is used that has been used throughout this dissertation. The $k\epsilon$ RNG turbulence model is used based on its performance during both the small scale and full-scale experiments. The exact prototype geometry is used for the CFD simulation. The mesh density is increased near the narrow opening and floor-to-ceiling opening on each floor. Heat loads are assumed to be evenly distributed across the ceiling and floor. Simulations are run under transient conditions, but are assumed to reach steady state when the bulk exhaust temperature varies less than 0.003 $°C$ for 1000 iterations. Radiation is accounted for using the Surface to Surface radiation model with a residual convergence criteria of 0.001. The enhanced wall function of the $k\epsilon$ RNG model is used with enhanced thermal effects and full buoyancy effects are also considered. Reference and operating temperatures are set to 21.8 $°C$.

An adiabatic boundary condition is applied to all exterior surfaces except the narrow opening on each floor, exhaust opening at the top of the shaft, and the floor and ceiling of the three floors. The narrow openings are modeled with a "pressure outlet" condition with a specified temperature of 21.8 $°C$. A "porous jump" is modeled just inside the narrow opening to account for the sudden convergence of the ambient air as it enters the opening. The pressure loss over this "porous jump" is calculated using Eq. 3.1 where $C_2 = 0.5$ for converging flow. The exhaust opening at the top of the chimney is also modeled with a "pressure outlet" condition with reverse flow conditions of 21.8 $°C$ although reverse flow through the exhaust opening is never pre-

dicted. The same "porous jump" condition is applied directly beneath the exhaust opening, but a C_2 value of 1 is used to simulate the sudden expansion of the air into the environment after it exits the opening. In both narrow and exhaust openings, the pressure loss of sudden expansions and contractions of the air within the CFD model are accounted for by the simulations. Finally, the floor and ceiling are used to evenly distribute heat loads using a constant heat flux boundary condition of 30 W/m^2.

Five shaft cross-sectional areas are considered: 2 m x 2 m, 2 m x 2.5 m, 2 m x 3 m, 2 m x 3.5 m, and 10 m x 10 m, the last of which models a large atrium. The total exhaust area is 4 m^2 in all five and remains unchanged in the first four. The large atrium case is exhausted by four 1 m^2 openings in the middle of the atrium. In the first four cases, the opening from each floor to the shaft is 6 m^2, while the same opening in the atrium case is 30 m^2. The exact geometry used for each case in presented in Fig. 6-2.

6.2.2 Single Chimney

To expand the investigation into the observed increased flowrates in upper floors, a single chimney is also modeled. Two cross sectional areas are considered. For a constant exhaust opening, lower flowrates are expected as the shaft area increases. Larger shaft areas require the flow to converge as it approaches the smaller exhaust opening, thus creating a pressure drop that will decrease the total flowrate compared to the base case.

A very similar procedure is used to model the single chimney with CFD simulations as is used to model the three story office building. The $k\epsilon$ RNG turbulence model is used with the enhanced wall function, enhanced thermal effects, and full buoyancy effects. Grid independence tests indicate a mesh size of 138,500 cells is sufficient for grid independence. The mesh density is increased near the heater and entrance to the shaft. Simulations are run under transient conditions, but are assumed to reach steady state when the bulk exhaust temperature varies less than 0.003 $°C$ for 1000 iterations. Radiation is accounted for using the Surface to Surface radiation model with a residual convergence criteria of 0.001. The reference and operating

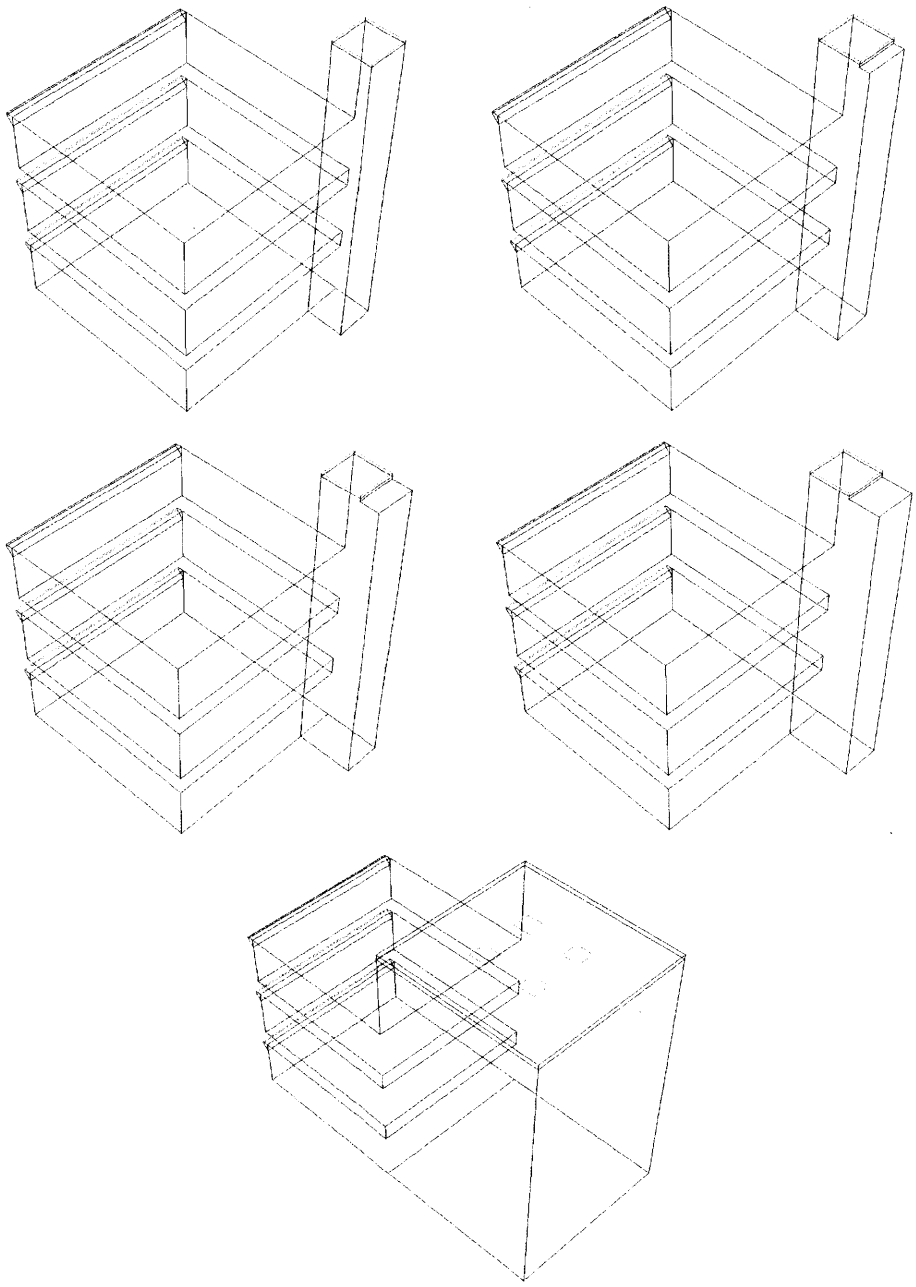

Figure 6-2: Geometry of the five cases of a three story office building simulated with CFD. The upper left image has a ventilation shaft measuring 2 m x 2 m and each progressively larger shaft measures 2 m x 2.5 m, 2 m x 3 m, and 2 m x 3.5 m respectively. The bottom image is used to simulate a large atrium measuring 10 m x 10 m instead of a ventilation shaft. All five cases have an equal total exhaust area of 4 m^2.

temperatures are set to 21.8 $°C$.

An adiabatic boundary condition is applied to all exterior surfaces except the inlet opening, exhaust opening, and the heater. The inlet opening is modeled with a "pressure outlet" condition with a specified temperature of 21.8 $°C$. A "porous jump" is modeled just inside the opening to account for the sudden convergence of the ambient air as it enters the opening and uses a C_2 value of 0.5. The exhaust opening is also modeled with a "pressure outlet" condition with reverse flow conditions of 21.8 $°C$ although reverse flow through the exhaust opening is never predicted. The same "porous jump" condition is applied directly beneath the exhaust opening, but a C_2 value of 1 is used to simulate the sudden expansion of the air into the environment after it exits the opening. The heater has a total area of 1.184 m^2 and a constant heat flux of 8080 W/m^2.

6.2.3 Small Scale Model

Model Construction

Although the small scale physical experiments described earlier in this dissertation initiate this investigation into the "ejector effect," none of them model the same change simulated by CFD models. Thus, additional small scale experiments are conducted to model the impact of expanding the ventilation shaft while retaining the same exhaust opening. The same experimental setup used in Chapter 3 is slightly modified to conduct these experiments. The exact configuration two is used, which has floor-to-ceiling openings, except a wall is inserted in the ventilation shaft, halving the total area to 0.031 m^2 as shown in Fig. 6-3. This case is referred to as the "base case." The wall is then removed to expand the ventilation shaft to a cross sectional area of 0.062 m^2 while the exhaust opening remains unchanged at 0.031 m^2. All material properties are identical to those described in Chapter 3 and the additional wall is constructed of the same insulation that surrounds the entire setup, 2 in of R$-$10 (1.76 m^2K/W) extruded polystyrene insulation.

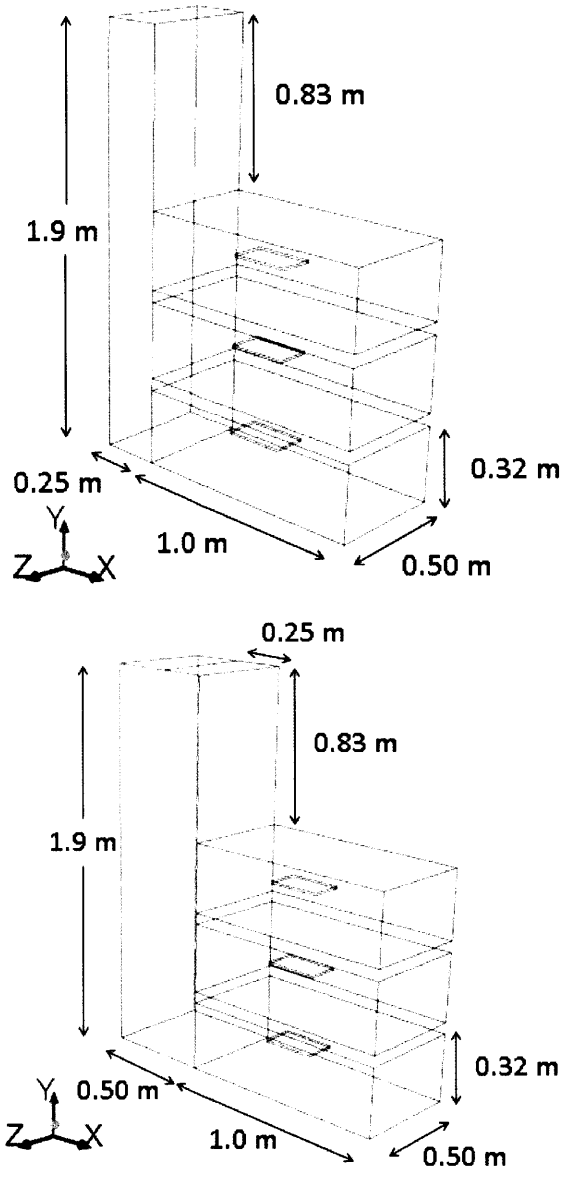

Figure 6-3: Schematic drawing of small scale model used to investigate the "ejector effect." The base case chimney (top) measures 0.25 m by 0.5 m and the expanded chimney (bottom) measures 0.5 m by 0.5 m. Both cases have the same exhaust area of 0.125 m^2.

Model Instrumentation

Volumetric airflow measurements and airflow visualization are provided for both the base case ventilation shaft and expanded shaft. Flow rates are measured at each inlet in accordance with ASHRAE Standard 111-2008 using the equal area method for the entrance to a rectangular duct [8]. Sixteen velocity measurements are taken at each inlet using a Graywolf AS-201 hotwire anemometer, which has a stated accuracy of +/− 3% rdg +/− 0.015 m/s. The measurements are made flush with the inlets to increase the liklihood of unidirectional flow. Three trials are made and the average flowrate for each floor is presented.

Airflow visualization is provided by the same neutrally buoyant bubble system used throughout this dissertation. As before, the ventilation shaft is lined with 1/16 in thick black felt to accentuate the bubbles in the shaft that are illuminated from above. A digital SLR camera with a 50 mm lens photographs the bubbles using a shutter speed between 1/6 to 1/2 s to create streaks that corresponds to bubble pathlines.

6.3 Results of Investigation of "Ejector Effect"

6.3.1 Single Chimney

Temperature contours at the bisecting plane for the 2 m x 2 m and 2 m x 4 m chimneys are presented in Figs. 6-4 and 6-5 respectively. Velocity fields taken at the same plane are presented in Figs. 6-6 and 6-7. The volumetric flowrate through the base case and expanded shaft are 2.018 and 1.850 m^3/s respectively and illustrate the impact of the flow near the exit.

6.3.2 Three Floor Office Building

Simulated flowrates through all three floors for each of the five shaft cross sectional areas are presented in Fig. 6-8. Temperature contours taken from the bisecting plane of the ventilation shaft are presented in Figs. 6-9 through 6-12. The temperature

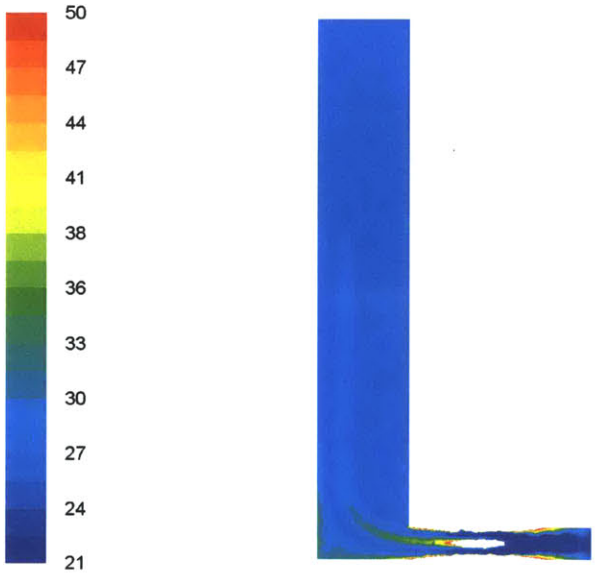

Figure 6-4: Temperature contour in $°C$ taken from the middle of the single chimney measuring 2 m by 2 m.

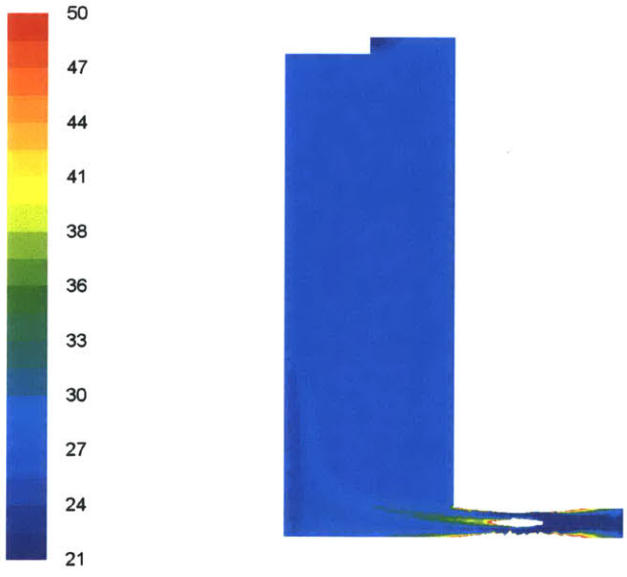

Figure 6-5: Temperature contour in $°C$ taken from the middle of the single chimney measuring 2 m by 4 m.

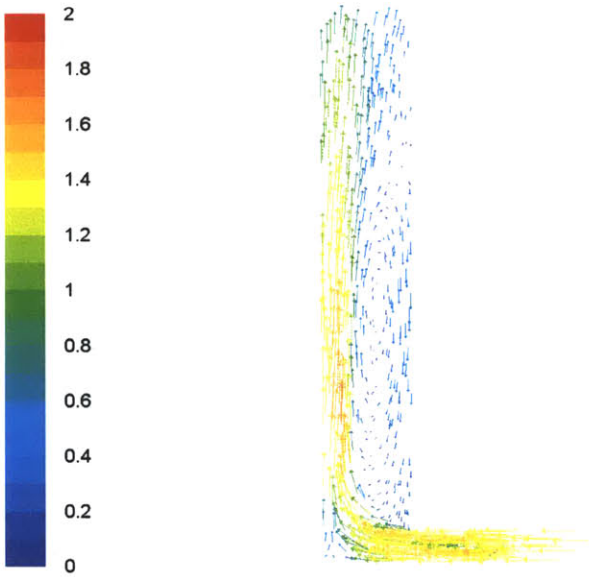

Figure 6-6: Velocity field m/s taken from the middle of the single chimney measuring 2 m by 2 m.

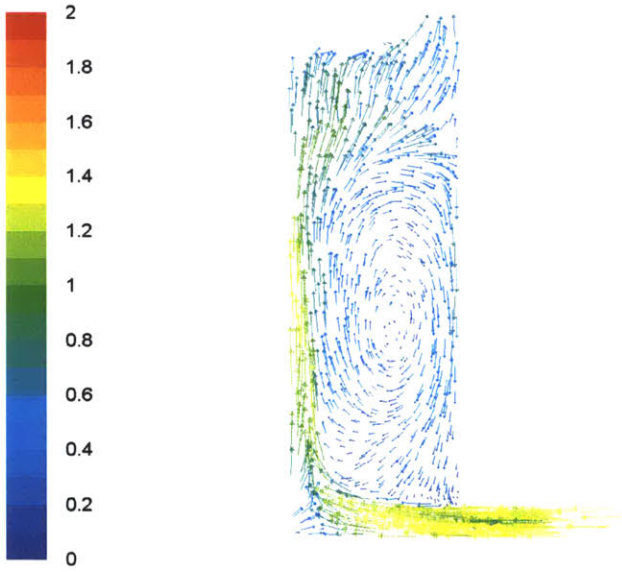

Figure 6-7: Velocity field m/s taken from the middle of the single chimney measuring 2 m by 4 m.

contour within the atrium is taken from the bisecting plane of the nearest two exhaust openings and shown in Fig. 6-13. Velocity fields are taken from the same locations and presented in Figs. 6-14 through 6-18.

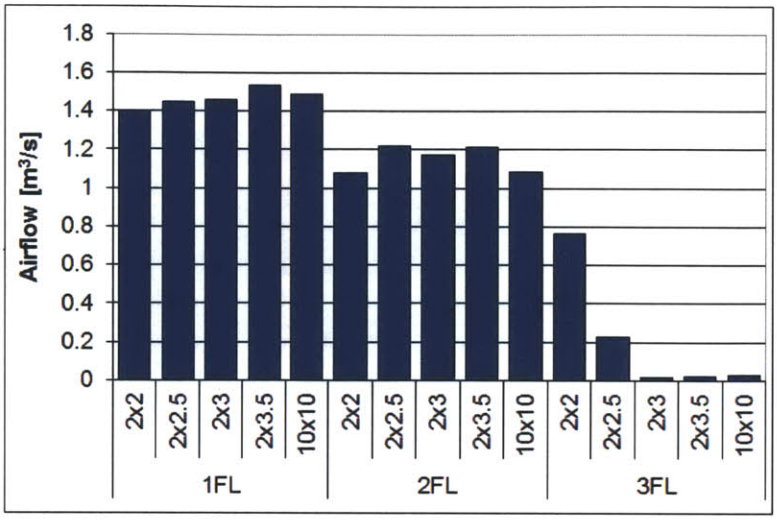

Figure 6-8: Predicted flowrates for the three story office building for each of the five shaft cross sectional areas.

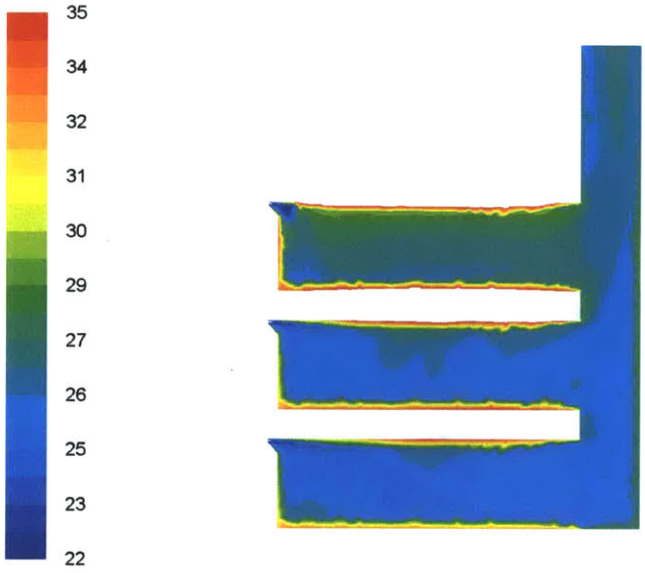

Figure 6-9: Temperature contour in $^{\circ}C$ taken from the middle of the 2 m by 2 m ventilation shaft in the three story office model.

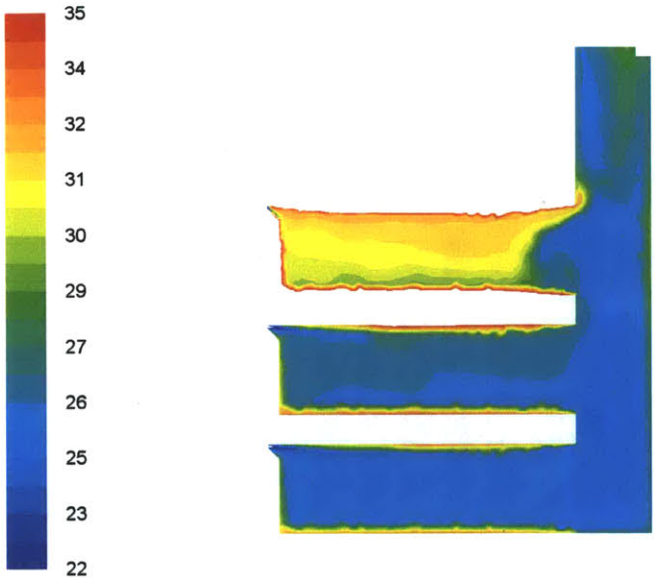

Figure 6-10: Temperature contour in $°C$ taken from the middle of the 2 m by 2.5 m ventilation shaft in the three story office model.

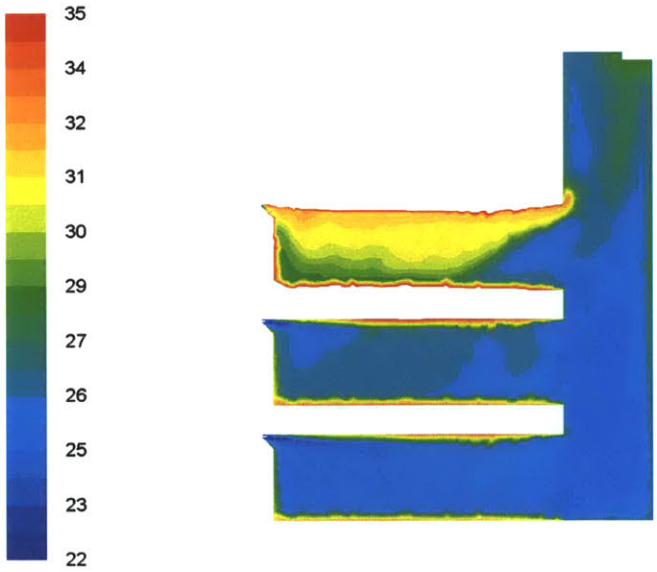

Figure 6-11: Temperature contour in $°C$ taken from the middle of the 2 m by 3 m ventilation shaft in the three story office model.

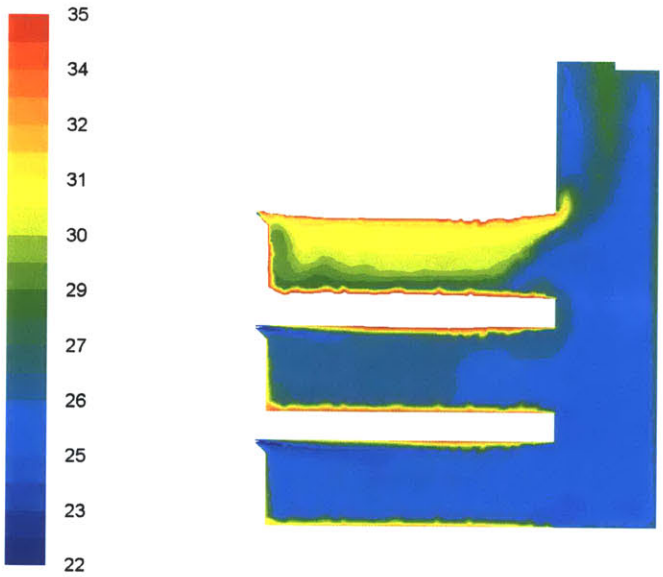

Figure 6-12: Temperature contour in $°C$ taken from the middle of the 2 m by 3.5 m ventilation shaft in the three story office model.

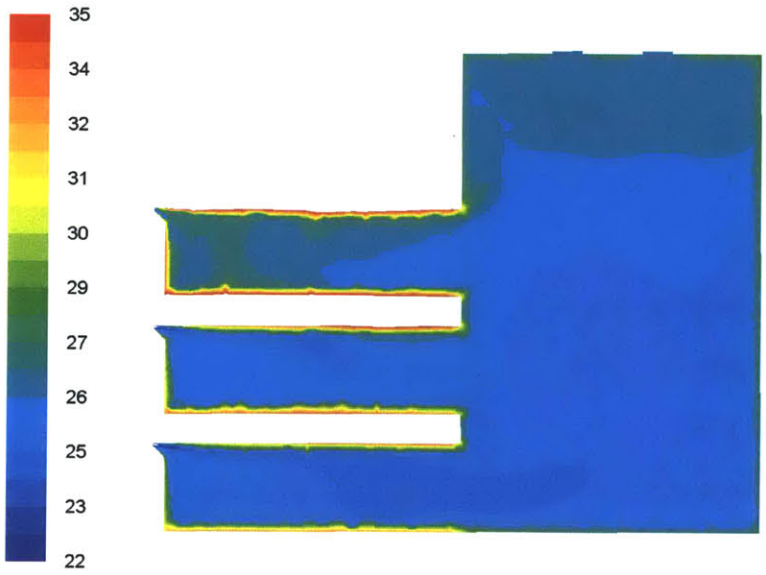

Figure 6-13: Temperature contour in $°C$ taken 6.5 m from the far edge of the 10 m by 10 m atrium in the three story office model. The plane bisects the two nearest exhaust openings in the atrium.

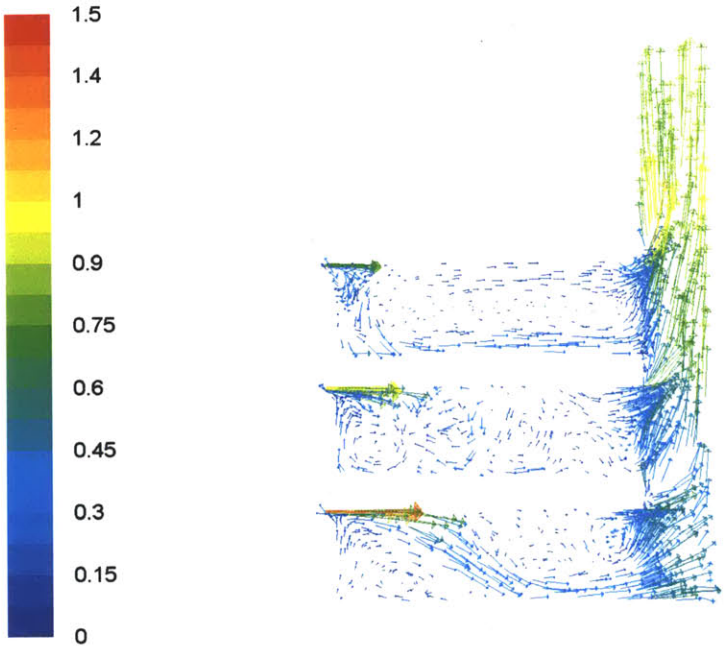

Figure 6-14: Velocity field in m/s taken from the middle of the 2 m by 2 m ventilation shaft in the three story office model.

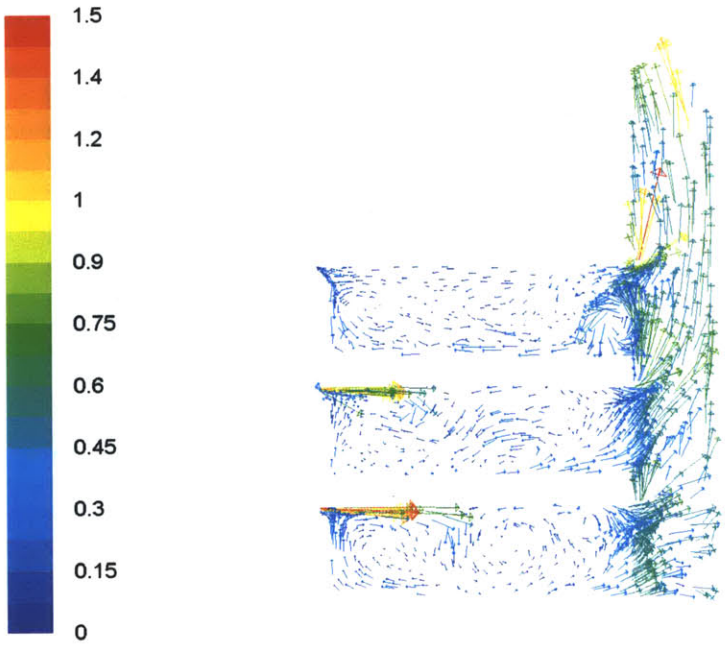

Figure 6-15: Velocity field in m/s taken from the middle of the 2 m by 2.5 m ventilation shaft in the three story office model.

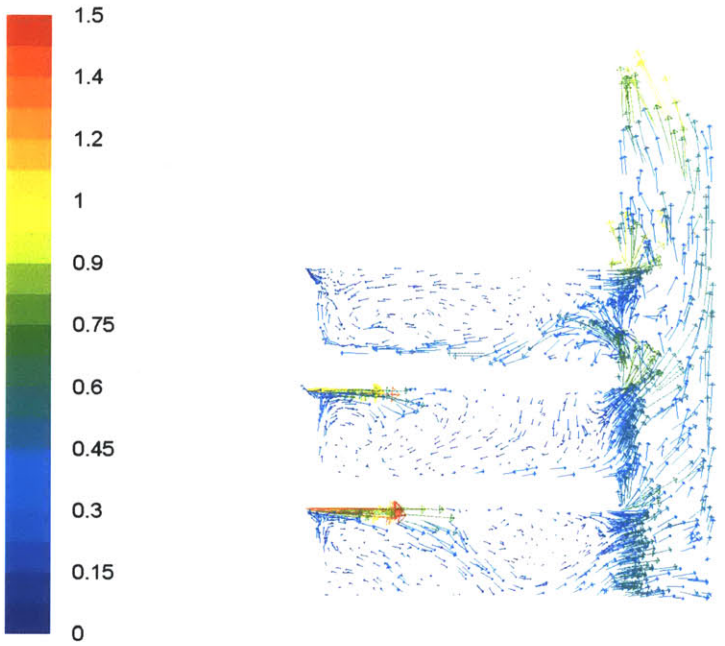

Figure 6-16: Velocity field in m/s taken from the middle of the 2 m by 3 m ventilation shaft in the three story office model.

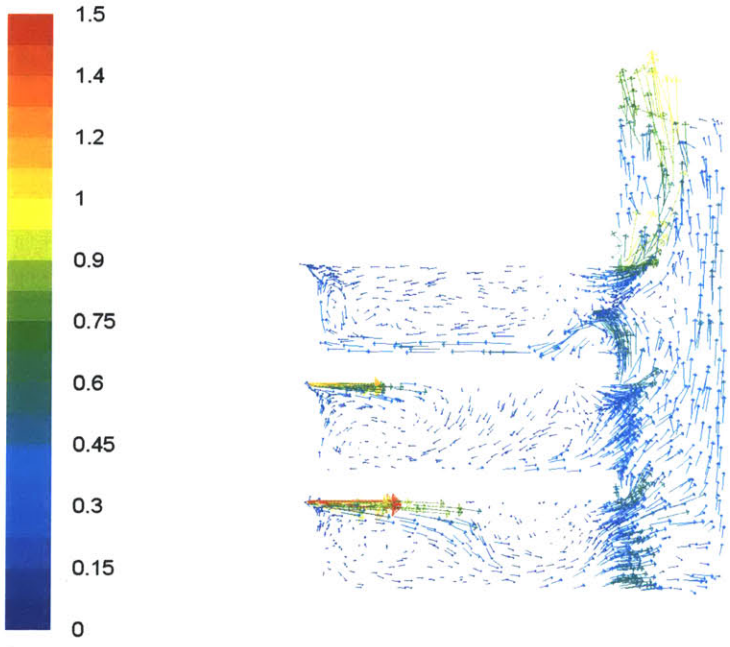

Figure 6-17: Velocity field in m/s taken from the middle of the 2 m by 3.5 m ventilation shaft in the three story office model.

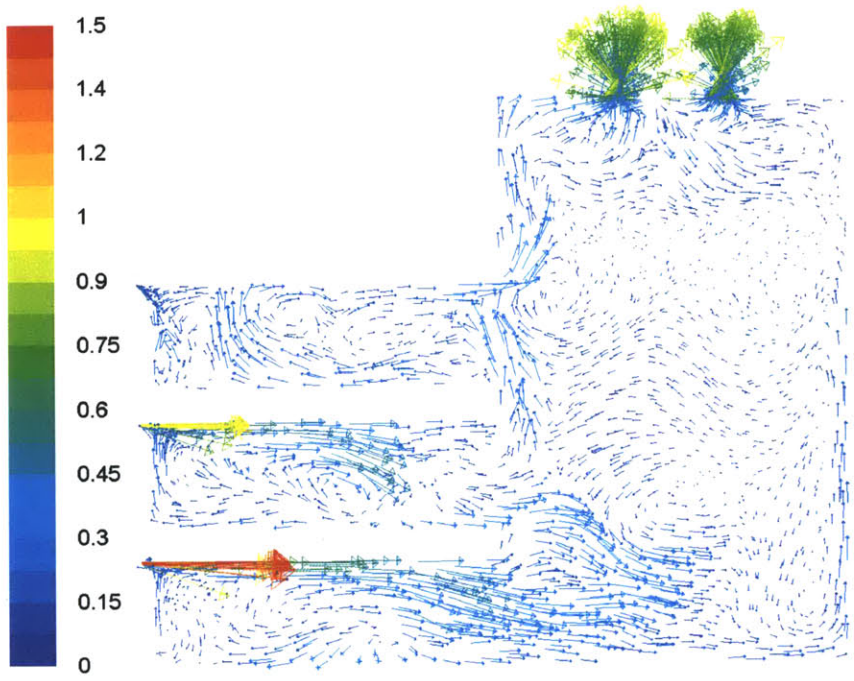

Figure 6-18: Velocity field in m/s taken 6.5 m from the far edge of the 10 m by 10 m atrium in the three story office model. The plane bisects the two nearest exhaust openings in the atrium.

Table 6.1: Averages of measured airflow rates at each takeoff duct for both the base case and expanded ventilation shaft trials. All values are reported in units $[m^3/s]$ and the experimental error is $+/-$ 0.0025 m^3/s .

Takeoff Duct	Base Case	Base Case std. dev.	Expand	Expand std. dev.
Top	0.012	0.00039	-0.0029	0.00027
Middle	0.0090	0.00063	0.011	0.0013
Bottom	0.023	0.0035	0.026	0.0040

6.3.3 Small Scale Building

The measured airflow rates for both 0.5 m x 0.25 m (base case) and 0.5 m x 0.5 m (expanded case) small scale building experiments are presented in Table 6.1. The average volumetric flowrate of three trials is presented along with the standard deviation.

Results from the airflow visualization of the small scale building experiment are presented in Figs. 6-19 through 6-26. Neutrally buoyant bubbles appear as white streaks against a black background. Some extraneous features of the setup are visi-

ble such as rectangular magnets, creases in the black felt, and reflections off acrylic panneling.

Figure 6-19: Experimental airflow visualization of the entrance from the lower duct into the base case ventilation shaft.

Figure 6-20: Experimental airflow visualization of the entrance from the lower (very bottom of image) and middle duct (large opening on right) into the base case ventilation shaft. Bubbles are introduced at the lower duct.

Figure 6-21: Experimental airflow visualization of the entrance from the middle duct into the base case ventilation shaft.

Figure 6-22: Experimental airflow visualization of the entrance from the upper duct into the base case ventilation shaft.

Figure 6-23: Experimental airflow visualization of the entrance from the lower duct into the expanded ventilation shaft.

Figure 6-24: Experimental airflow visualization of the entrance from the middle duct into the expanded ventilation shaft.

Figure 6-25: Experimental airflow visualization of the entrance from the middle and top duct into the expanded ventilation shaft. Bubbles are introduced into the middle duct. The solid gray line across the entire image is added during post processing to eliminate a bright relfection at the boarder of two acrylic pannels.

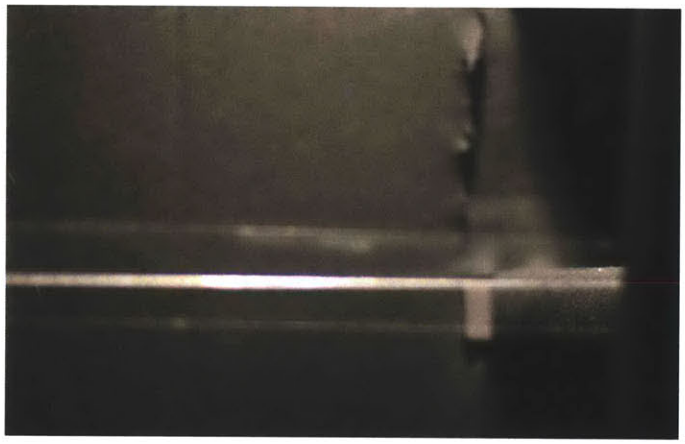

Figure 6-26: Experimental airflow visualization of the entrance from the top duct (shown in the upper 2/3 of the photo) into the expanded ventilation shaft. No bubbles entered through the top duct.

6.4 Discussion of Results from Investigation

Simulated results from the small office building suggest this "ejector effect" impacts the airflow in a full scale building. When a 2 m x 2 m shaft is used, all three floors experience a fairly similar temperature distribution with a mean air temperature of around 26-27 $°C$. When the shaft is expanded to 2 m x 2.5 m, the third floor air temperature jumps to nearly 30 $°C$ due to the reduced airflow through that floow. This same increase is observed in the two other expanded ventilation shafts considered. The airflow rates presented in Fig. 6-8 also confirm this difference in performance by showing the severe reduction in flowrate through the top floor for expanded shafts. What seems like an acceptable design to provide comfortable temperatures to all three floors fails to perform when the ventilation shaft is expanded and the exhaust area is held constant. Although one could argue an expanded shaft should have an expanded exhaust opening, the area is held constant in these simulations to isolate the impact of expanding the ventilation shaft. Furthermore, exhaust openings are constrained by other factors such as the exterior appearance of the building, equipment on the roof, or window louver mechanics and can not be changed so easily.

A partial explanation is provided by an analysis of the pathlines near the exhaust opening shown in Figs. 6-14 through 6-17. The pathlines near the exhaust opening in Fig. 6-14 are completely vertical because no obstructions block the airflow. However, as the shaft is expanded, more of the airflow has to flow around the upper corner of the shaft. The pathlines near this corner in Figs. 6-15 through 6-17 bend towards the exhaust opening, which corresponds with a pressure loss as the flow is diverted from the corner. This pressure loss from the exhaust opening geometry is also confirmed by the single chimney simulations where the simplified geometry reduces the complexities introduced by multiple floors. Even with a single floor, the 2 m x 2 m chimney obtains a higher flow rate of 2.018 m^3/s compared to the flow rate of 1.850 m^3/s obtained by the 2 m x 4 m chimney. A similar comparison of the exhaust openings in Figs. 6-6 and 6-7 shows the vertical pathlines in the 2 m x 2 m chimney and the same change in direction of the pathlines in the 2 m x 4 m case.

Another explanation for this "ejector effect" can be deduced from a comparison between Fig. 6-14 and Figs. 6-15 through 6-17. In the 2 m x 2 m case shown in Fig. 6-14, higher velocities directly above the second floor lead to more vertical momentum in the shaft that helps induce air through the third floor up through the exhaust opening. The expanded shafts increase the cross-sectional area of the shaft, which reduces local velocities and consequently decreases vertical momentum in the shaft. The larger shafts require more expansion of the air from each floor into the shaft, which further reduces vertical velocities and momentum. Pathlines entering the shaft from the first floor in the 2 m x 2 m shaft shown in Fig. 6-14 have larger vertical components than pathlines in the same location in the expanded shafts shown in Figs. 6-15 through 6-17. With less vertical momentum in the shaft, a significant portion of the airflow enters the third floor, which leads to the minimal flowrates shown in Fig. 6-8 and high temperatures in Figs. 6-10 through 6-12.

This same decrease in vertical momentum is also observed in the physical small scale experiments. Comparisons of the airflow visualizations for the base case chimney and the expanded chimney confirm the expansion of air as it enters the expanded chimney, resulting in less vertical momentum. Specific comparisons can be made between Figs. 6-19 and 6-23 for the bottom floor and Figs. 6-21 and 6-24 for the middle floor. The decrease in vertical momentum and additional pressure drop of the expanded chimney is large enough that reverse flow occurs on the third floor as indicated by Fig. 6-26. Bubbles introduced at the entrance of the top duct never enter the chimney.

These two effects, an additional pressure loss from the top of the chimney and decreased vertical momentum from an expanded shaft, do not explain the higher flowrates observed and predicted through the top duct in the small scale experiments of Chapter 3 or the base case small scale experiments described in this chapter. Consider the base case flowrates through the middle and top ducts presented in Table 6.1 where the top flowrate is 33% larger than the middle one. This result seems counterintuitive given the analytical models in Eq. 2.5 and Eq. 2.7 where flowrate is directly proportional to the height difference between openings. These models thus

predict a higher flowrate for lower floors than upper floors if all other paramteres are held constant. However, these models fail to account for the momentum within the shaft. The airflow from the bottom duct flows in the chimney past the entrance of the middle duct. The momentum of this airflow decreases the pressure at that entrance, which in turn increases the airflow through the middle duct compared to the case where no existing airflow in the shaft helps induce flow. Now consider the top duct where alll the airflow from the bottom and middle duct is flowing in the chimney past its entrance. An even larger amount of momentum within the shaft helps induce the flow through the top floor. The floor-to-ceiling openings and relatively short chimney height provide the right conditions in which this flow induction from the momentum of lower ducts increases the flow through the top duct above the flow through the middle duct. This same principle is used in a jet pump shown in Fig. 6-27.

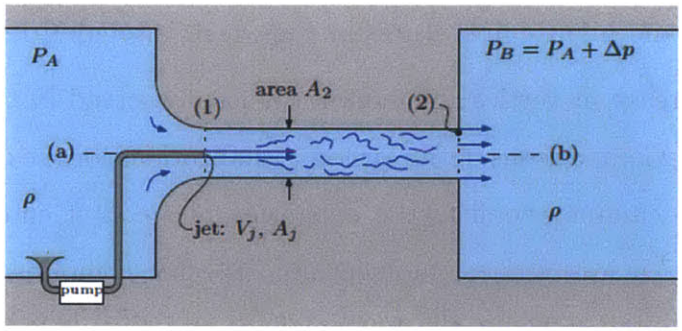

Figure 6-27: Schematic drawing of a jet pump that uses a jet to increase momentum in a channel, therby lowering the pressure at (1) and inducing flow through the channel.

6.5 Improvements to MIT Airflow Network Tool CoolVent

Designers who want to predict the annual performance of a naturally ventilated building typically rely on airflow network models due to their moderate complexity and ability to quickly predict yearly performance. However, as discussed in Chapter 2, none of the current models account for air momentum within the space. As demonstrated earlier in this chapter, the air momentum can have a significant impact on

the airflow rates and indoor temperatures of a naturally ventilated building, and thus should not be neglected in airflow network models. The remainder of this chapter describes the improvements that have been made to the existing airflow network tool developed at MIT called CoolVent.

6.5.1 Description of Improvements made to CoolVent

Both the three-story office building and single chimney modeled with CFD earlier in this chapter are modeled by CoolVent. A rendering of the office building divided into seven zones is shown in Fig. 6-28 as well as a rendering that displays the ten openings within the building. All geometric parameters and boundary conditions are matched, as indicated by the input files shown in Appendix A. Because current airflow network models do not account for the momentum of air, CoolVent in its original form does not demonstrate the "ejector effect." Instead, it predicts flowrates that are quite similar between the four cases of the office building (the atrium is not considered) because all openings, height differences, and heat sources are held constant. These parameters have the biggest impact on the predicted airflow given the current limitations of CoolVent. Similarly, the two cases of the single chimney are expected to have similar flowrates when modeled by the existing CoolVent. A rendering of the single chimney is shown in Fig. 6-29 with labeled openings used in CoolVent.

A major factor in the design of the improvements to CoolVent is their transferability to other airflow network models. Thankfully most airflow network models share numerous prominent features such as a network of nodes, reliance on the Bernoulli equation, and use of a power-law function to calculate flowrates. Furthermore, CoolVent has been demonstrated to accurately predict airflow rates and indoor temperatures of various types of buildings [67]. For these reasons, the improvements do not change the central structure of CoolVent, but instead add a few enhancements to the existing program. Specifically, the effects of air momentum within the shaft and the geometry near the exhaust opening are accounted for by improved discharge coefficients calculated with empirical relationships from an extensive body of Rus-

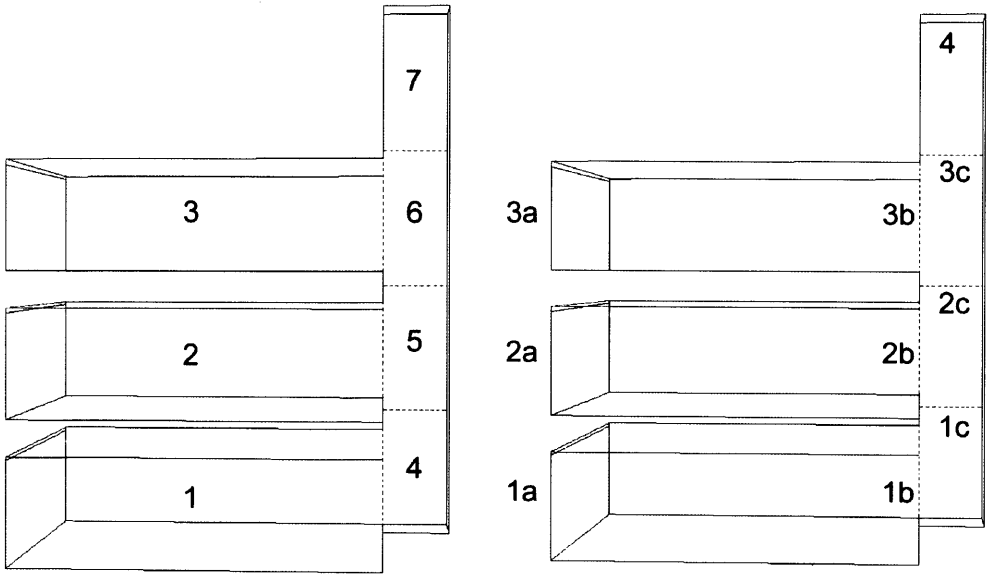

Figure 6-28: Rendering of geometry of three-story office building used in CoolVent (left) labeled with zone numbers and (right) openings. Dotted lines indicate imaginary surfaces used as interior zone boundaries.

sian literature. I.E. Idelchik summarizes much of this literature in his book, which is used as a reference for the specific empirical relationships [32]. The relationships in Idelchik's book provide pressure loss coefficients, k, defined similarly to Eq. 3.1 from Chapter 3 that calculates a pressure loss based on a known bulk valocity. This k, which is based on the total pressure difference, is converted to a k_{eff} that is based only on the static pressure difference using the Bernoulli equation and definition of k.

$$\frac{P_1 - P_2}{\rho} + \frac{v_1^2 - v_2^2}{2} = \frac{k v_1^2}{2} \tag{6.1}$$

where P_1 and P_2 are static pressures. Rearranging Eq. 6.1 in terms of only the static pressure difference provides the definition of k_{eff}

$$P_1 - P_2 = \frac{\rho v_1^2}{2}\left[k - \left(1 - \frac{v_2^2}{v_1^2}\right)\right] \tag{6.2}$$

where k_{eff} is defined as

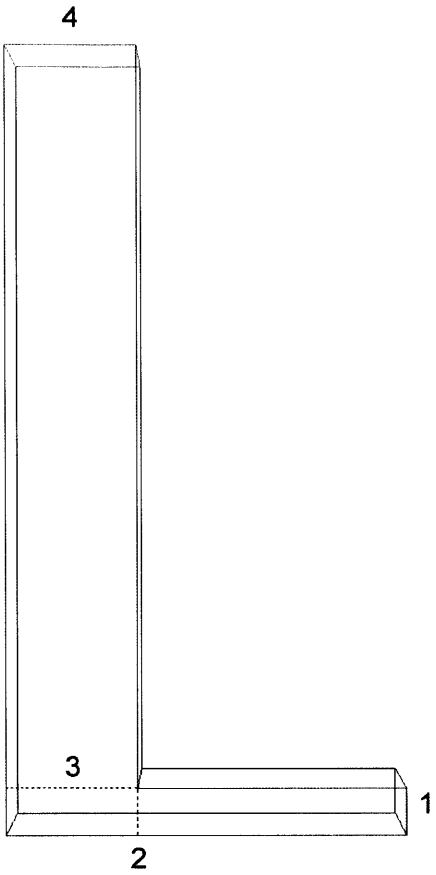

Figure 6-29: Rendering of geometry of single chimney used in CoolVent openings labeled. Dotted lines indicate imaginary surfaces used as interior zone boundaries.

$$k_{eff} = k - \left(1 - \frac{v_2^2}{v_1^2}\right) \tag{6.3}$$

CoolVent uses a discharge coefficient, C_D, defined similarly to Eq. 2.4 from Chapter 2, that calculates an airflow based on a known pressure difference. A simple conversion between k_{eff} and C_D is obtained by equating the static pressure difference for both coefficients and solving for C_D in terms of k_{eff}.

$$\dot{V}_{orifice} = AC_D\sqrt{\frac{2\Delta P}{\rho}} \tag{6.4}$$

$$v^2 = C_D^2\frac{2\Delta P}{\rho} = \frac{2\Delta P}{k_{eff}\rho} \tag{6.5}$$

$$C_D = \frac{1}{\sqrt{k_{eff}}} \tag{6.6}$$

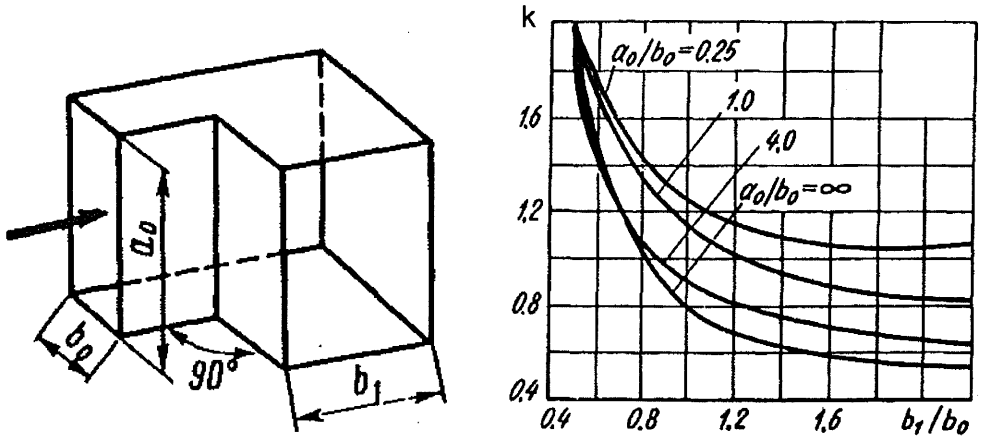

Figure 6-30: Geometry of 90° bend (left) and relationship from Idelchik's Diagram 6.6 to account for the resulting pressure loss from the bend (left). Source [32]

This conversion factor is used to convert the calculated value of k from Idelchik's book to the desired C_D for CoolVent. In the three-story office building, the discharge coefficient for openings 1a, 2a, and 3a is calculated using equation 3.1 for a sudden flow contraction, which is the same value used in the CFD modeling throughout this thesis[32]. Equation 3.1 specifies a k value of 0.5 for the convergence of flow from a large space to a confined area. The discharge coefficient at opening 1b is calculated using Idelchik's Diagram 6.6 for a 90° bend in the flow [32]. This relationship is copied in Fig. 6-30. The momentum effects within the chimney are accounted for in openings 2b and 3b using Idelchik's Diagram 7.4 and openings 1c and 2c using Idelchik's Equation 7.2 for converging wyes at 90° [32]. The relationship from Idelchik's Diagram 7.4 and Idelchik's Equation 7.2 are shown in Eqs. 6.7 and 6.9 respectively. The discharge coefficient for opening 4 is calculated with Idelchik's Diagram 8.1 for a sudden flow restriction [32], which is copied in Eq. 6.10. The discharge coefficients for the single chimney are also changed using these relationships from Idelchik. The same relationship for a sudden contraction, Idelchik's Diagram 8.1, is used when accounting for the top of the single chimney and Idelchik's Diagram 6.6 is also used to account

for the 90° bend in the flow. A complete listing of the old and new C_D values for both the office and single chimney is presented in Appendix B. These changes to CoolVent can easily be made to other airflow network models to account for the momentum effects of the air in the ventilation shaft and the change in exhaust geometry.

$$k = C\left[1 + \left(\frac{v_s}{v_c}\right)^2 - 2\left(1 - \frac{\dot{V}_s}{\dot{V}_c}\right)^2\right]\left(\frac{v_s}{v_c}\right)^2 \tag{6.7}$$

$$C = 0.9 * \left(1 - \frac{\dot{V}_s}{\dot{V}_c}\right) \tag{6.8}$$

$$k = \frac{1 - \left(1 - \frac{\dot{V}_s}{\dot{V}_c}\right)^2 - \left(1.4 - \frac{\dot{V}_s}{\dot{V}_c}\right)\left(\frac{\dot{V}_s}{\dot{V}_c}\right)^2}{\left(1 - \frac{\dot{V}_s}{\dot{V}_c}\right)^2} \tag{6.9}$$

$$k = \left[0.707\left(1 - \bar{f}\right)^{0.375} + 1 - \bar{f}\right]^2 \frac{1}{\bar{f}^2} \tag{6.10}$$

In Equations 6.7 through 6.10, v_s is the bulk velocity through the opening from the adjacent floor, v_c is the bulk velocity through the chimney directly below the opening, $\dot{V}_s$ is the volumetric flow rate through the opening from the adjacent floor, $\dot{V}_c$ is the volumetric flow rate through the chimney directly below the opening, and $\bar{f}$ is the ratio of the exhaust area to the shaft cross sectional area. The pressure loss from friction along the walls of the ventilation shaft is accounted for using the Darcy-Weisbach equation [64]

$$\Delta P = \frac{1}{2} f \frac{L}{D_H} \rho v^2 \tag{6.11}$$

where the friction factor f is calculated using an empirical relationship developed by Haaland for the transitionally rough regime [64]

$$f = \left\{1.8 log\left[\frac{6.9}{Re_d} + \left(\frac{\epsilon}{3.7 D_H}\right)^{1.11}\right]\right\}^{-2} \tag{6.12}$$

where the surface roughness ϵ is assumed to equal 0.04 mm for smooth concrete. An equivalent k value is obtained from Eq. 6.11 by equating it to Eq. 3.1 such that

$$k_{friction} = \frac{fL}{D_H} \tag{6.13}$$

The largest frictional pressure loss coefficient $k_{friction}$ is found at the top of the 2 m by 2 m shaft, where the largest local velocities are predicted to occur in the smallest cross-sectional area. In this region, $k_{friction} = 0.0153$, which is less than 2% of the pressure loss coefficient assuming negligible friction. Thus, the frictional pressure loss is neglected for these simulations and can likely be neglected in most ventilation shafts of modest size.

6.5.2 Results and Discussion from Improved CoolVent

Simulated ariflow rates through the single chimney and office building are presented in Figs. 6-31 and 6-32 respectively.

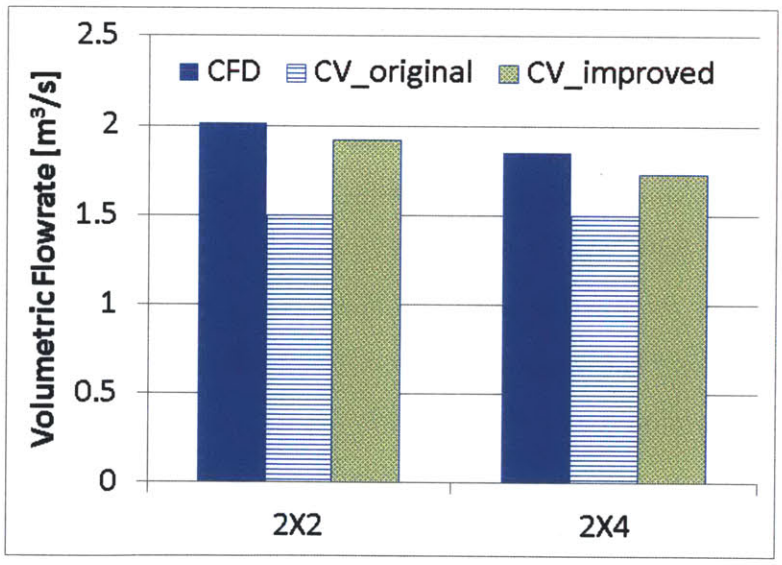

Figure 6-31: Simulated airflow rates through the single chimney predicted using CFD, the original CoolVent, and an improved version of CoolVent. Both chimney geometries are plotted and labeled on the horizontal axis.

As predicted, the original CoolVent predicts identical flow rates for the 2 m x 2 m and 2 m x 4 m chimneys even though the validated CFD model predicts a lower flow rate for the larger chimney because of its larger cross-sectional area and sudden

contraction near the exhaust. Furthermore, the original CoolVent underpredicts the flow rate by 25% in the 2 m x 2 m case. The improved CoolVent accounts for these effects and predicts a similar decrease in flowrate when the chimney expands. Additionally, the improved CoolVent predicts flowrates that agree with the CFD values to within 5% and 7% for the 2 m x 2 m and 2 m x 4 m chimneys respectively.

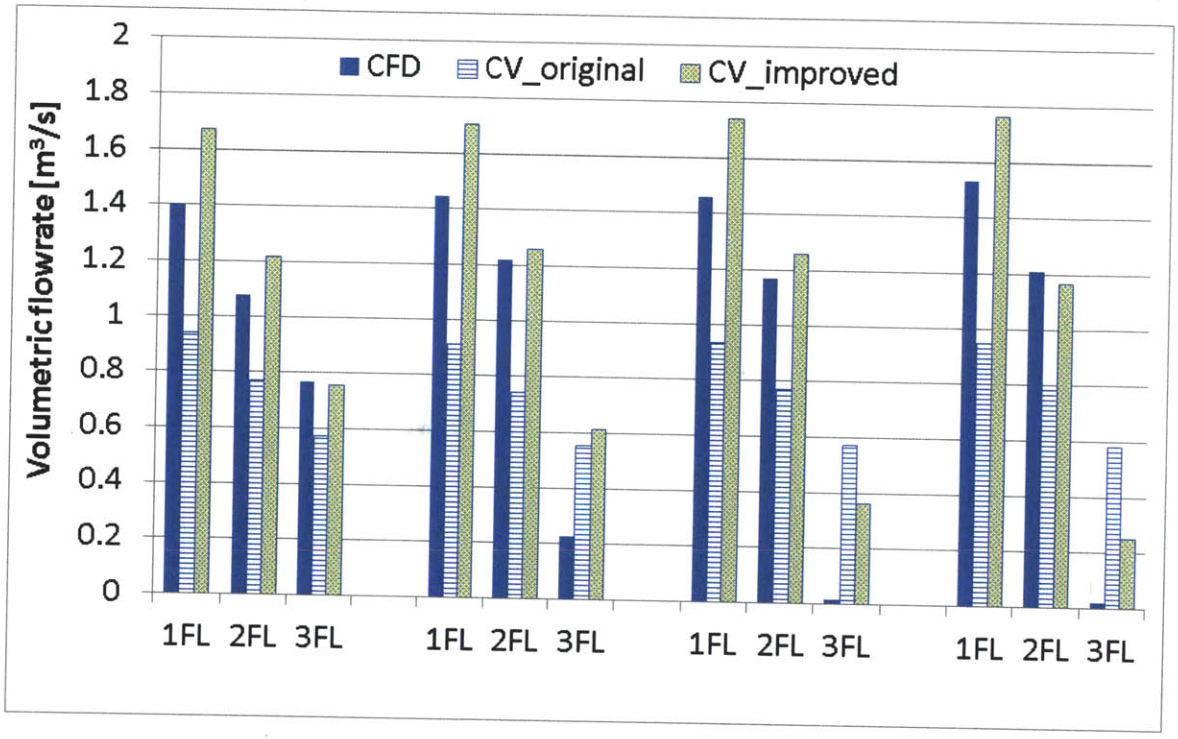

Figure 6-32: Simulated airflow rates through the office building predicted using CFD, the original CoolVent, and an improved version of CoolVent. All four shaft sizes are considered and labeled on the horizontal axis.

Results from the office building simulations also confirm that the original CoolVent predicts the same airflow rates for all four chimney sizes. Thus the significant impact of the "ejector effect" is not accounted for and the general trend of the CFD predicted flow rates is not matched. The original CoolVent underpredicts the CFD values by nearly 40% for the first and second floors, and drastically overpredicts the airflow rate on the third floor for the expanded chimney cases. The improved CoolVent values agree much more closely with the CFD values on the first and second floors, agreeing to within 3% in some cases. The largest disagreement on these two floors is 19% for the first floor of the 2 m X 3 m case. Additionally, the improved CoolVent matches

the trend of decreasing flow rate through the third floor as the chimney is expanded. Although it overpredicts the CFD value, it offers a significant improvement over the original CoolVent by allowing designers to predict the trend rather than suggesting that an increased chimney area has no impact on the flow rate. Given the constraint of not altering the central structure of CoolVent, the close agreement between the improved CoolVent and CFD on the first and second floors and the correct trend on the third floor are found to provide significant and valuable improvements over the original CoolVent.

Chapter 7

Conclusion and Future Work

7.1 Conclusion

Nearly 13% of the primary energy in the United States and most developed countries goes towards cooling and ventilating buildings [2]. Pure and hybrid natural ventilation systems have been shown to save up to 77% of this energy by leveraging wind or buoyancy effects to draw outside air into the building [51]. However, whether a pure or hybrid natural ventilation system is used, architects and developers will not use it unless they can predict that such a system will provide comfortable indoor conditions and be worth the capital cost. Pure natural ventilation systems often require less capital cost than mechanical systems, but their ability to reliably provide comfortable conditions throughout the year is heavily depends on the local climate. In order to predict indoor comfort conditions and properly run advanced control systyems, numerous modeling techniques are required.

Hybrid ventilation, on the other hand, ensures the same level of comfort provided by a mechanical system because of its ability to use mechanical cooling when needed. A key criterion to using hybrid ventilation is whether the capital cost of installing both a mechanical and natural system is offset by reduced energy costs and other incentives. Thus, modeling techniques are required to predict the reduction in energy costs before major design decisions have been made.

Current modeling techniques of naturally ventilated buildings fall into five cat-

egories: analytical/empirical, small scale, full scale, airflow network, and computational fluid dynamics (CFD). Each category has its unique advantages and limitations, which provide ample room for improvements. Analytical/empirical models are too simple to use in most real-world situations. Small scale models require careful replication of the full scale building and rely on threshold values of nondimensional numbers that are often vaguely defined and can vary with geometry. Full scale models are resource intensive and often lack sufficient measurements, particularly acurate airflow visualization. Airflow network models make simplifying assumptions that can neglect important phenomena. CFD models have been shown to accurately simulate natural ventilation systems, but generally require long run times and do not provide annual results or the energy use associated with the system.

This thesis enables designers and engineers to make more informed decisions on the expected comfort conditions and energy savings of naturally ventilated buildings by enhancing current modeling techniques. Specific contributions are summarized below.

- CFD models can be used with more confidence after they have been validated with small scale and full scale experiments.

- Small scale models relying on buoyancy-driven natural ventilation will more accurately model the full scale building because the threshold value of the nondimensional Grashof number is refined.

- Greater detail can be extracted from a full scale data set because a full scale experiment has been conducted with more detail than any published work to date.

- Intricate flow characteristics can now be observed using a novel flow visualization technique for in-situ flow visualization in full scale buildings.

- Airflow network models will better account for the significant impact of the exhaust pathway cross section.

- Designers can incorporate natural ventilation into a wider range of buildings because an "ejector effect" has been demonstrated in exhaust shafts that increases the total airflow through naturally ventilated buildings while requiring less space for the system.

- Only modest duct cross-sections are needed to provide for buoyancy driven natural ventilation in multi-story buildings.

A 1/4 scale model of a ventilation shaft uses air as its working fluid to validate various CFD turbulence models. Seventy-two temperature measurements within the shaft agree with predicted temperatures with an RMSE of 1.09 C, 1.03 C, and 1.92 C for the $k\epsilon$, $k\epsilon$ RNG, and LES turbulence models respectively. The largest percent difference between measured and simulated flowrates is 9.2%, 13%, and 14% for the $k\epsilon$, $k\epsilon$ RNG, and LES models respectively. Experimental pathlines are created within the shaft using a novel flow visualization technique that uses neutrally buoyant soap bubbles photographed with a long exposure. The profile of these experimental pathlines agrees well with the simulated pathlines from each of the three turbulence models.

Small scale experiments of buoyancy driven natural ventilation can not exactly match the nondimensional Grashof number with the prototype building. Experimenters have worked around this problem by developing a threshold Grashof number. Historically this threshold has been between $10^6 - 10^9$ [23]. The experimental basis for this range is crude and thus a more detailed study of a simple ventilation chimney has been conducted. Validated CFD simulations are used to model four different scales of a simple chimney to suggest a Grashof threshold of $1.2e10$. This new threshold does not gaurantee similtude in every flow configuration, but demonstrates that the previous threshold is inadequate for the ventilation shaft considered.

A full scale experiment is conducted in the four-story atrium of MIT building E14 to provide further validation of the three CFD turbulence models. Forty-eight thermocouple measurements throughout the atrium, measured airflow rates at the boundary, and flow visualization techniques are used to show close agreement between

CFD predictions and measured results.The same neutrally buoyant bubbles are used to demonstrate an effective in-situ flow visualization process that can be used in full-scale buoyancy-driven flows.

In the small scale three story building with floor to ceiling openings, higher flowrates are observed through the third floor than the second even though all other parameters are held constant. This observation of what has been termed the "ejector effect" suggests a significant limitation in the simple analytical models typically used to model buoyancy-driven natural ventilation. CFD simulations of a full scale three story office building and simple chimney are used to further investigate the "ejector effect." Simulations of the three story office building reveal that a 2 m x 2 m chimney leads to the highest total and most evenly distributed flowrate when compared to a 2 m x 2.5 m, 2 m x 3 m, or 2 m x 3.5 m chimney and even a 10 m x 10 m atrium. In all five cases, the total exhaust area is held constant and all other parameters are fixed. For the expanded chimney cases, very little air flows through the third floor, resulting in temperatures approaching 30 $°C$. This increased flow through the 2 m x 2 m chimney results from two main reasons. First, there is a smaller pressure drop at the top of the chimney in the 2 m x 2 m case because there is no reduction in cross-sectional area as the flow approaches the exhaust opening. Second, the small cross-sectional area allows for high momentum within the shaft that helps induce flow through upper floors, which is called the "ejector effect."

Finally, CoolVent is used as a representative airflow network tool to show that this "ejector effect" has not been previously accounted for in such models. The momentum of air within each zone is excluded. Careful design has allowed for the basic structure of airflow network tools to remain untouched while accounting for the "ejector effect" with empirical relationships to calculate pressure loss coefficients. The original CoolVent underpredicts the flowrate through a simple chimney by 25% and predicts no change when the chimney is expanded, even though a 9% decrease is observed. The improved CoolVent predicts flowrates that agree to within 3% and 7% for the 2 m x 2 m and 2 m x 4 m chimneys respectively. When the three story office building is modeled, the original CoolVent underpredicts the CFD values by

nearly 40% for the first and second floors, and drastically overpredicts the airflow rate on the third floor for the expanded chimney cases. Furthermore, the original CoolVent predicts a minimal difference between the different size chimneys, although substantial differences are predicted with the validated CFD models. The improved CoolVent values agree much more closely with the CFD values on the first and second floors, agreeing to within 1% in some cases. The largest disagreement on these two floors is 25% for the second floor of the 2 m x 3.5 m case. Additionally, the improved CoolVent matches the trend of decreasing flow rate through the third floor as the chimney is expanded.

7.2 Future Work

This research will be continued in the immediate future through a post doctoral researcher who will monitor a newly finished ten story Japanese office building in central Tokyo. Full building measurements of temperature, air velocities, plug loads, humidity, and a weather station on the roof will allow for an even more complete dataset of a buoyancy-driven naturally ventilated building. This dataset will be used to further validate the CFD and airflow network models.

Additional future work can be conducted by exploring the minimum chimney area in which the ejector effect dominates over the frictional losses along the sides of the shaft. As shown in Chapter 6, the frictional losses in a 2 m x 2 m shaft within the simulated office building are less than 2% of the pressure loss coefficient that accounts for the ejector effect. As the shaft area decreases, higher velocities will lead to larger frictional pressure losses that will eventually dominate over the ejector effect. This transition point is important for designers and should be identified for various types of shaft materials.

The empirical models introduced into CoolVent are applicable to other airflow network tools and can be incorporated to leverage the capabilities of integrated airflow network models in whole building simulation tools, such as EnergyPlus.

Lastly, the in-situ airflow visualization technique demonstrated in both small scale

and full scale experiments can be used to observe airflow patterns in more full scale buoyancy-driven naturally ventilated buildings.

Appendix A

CoolVent Input File

Table A.1: Input file for three story office building simulation in CoolVent. The $*$ indicates chimney width, which is changed with each case. All other inputs are held constant.

Input Values
21.8
1
0.15
0
0
45
90
138
1
3
10
2*
10
4
5.3
1
4
6
22
60
0
0.1
0.9
1
0
10
10
0
0
0
0
12
0
15

Table A.2: Input file for single chimney simulation in CoolVent. The * indicates chimney width, which is changed with each case. All other inputs are held constant.

Input Values
21.8
1
0.15
0
0
45
90
138
1
1
4
2*
2
0.72
11.6
1.43
4
6
24
1010
0
0.1
0.9
1
0
10
10
0
0
0
0
12
0
15

Appendix B

Old and New CoolVent Discharge Coefficients

Table B.1: Old and new discharge coefficients used in CoolVent for the three-story office building with a 2 m x 2 m shaft.

Opening	Old C_d	New C_d	Idelchik Diagram
1a	0.65	1.40	3.1
2a	0.65	1.40	3.1
3a	0.65	1.40	3.1
1b	1	0.767	6.6
2b	1	0.275	7.4
3b	1	0.162	7.4
1c	1	0.513	7.2
2c	1	0.901	7.2
3c	1	10.0	-
4	0.85	1.00	8.1

Table B.2: Old and new discharge coefficients used in CoolVent for the three-story office building with a 2 m x 2.5 m shaft.

Opening	Old C_d	New C_d	Idelchik Diagram
1a	0.65	1.40	3.1
2a	0.65	1.40	3.1
3a	0.65	1.40	3.1
1b	1	0.857	6.6
2b	1	0.341	7.4
3b	1	0.177	7.4
1c	1	0.521	7.2
2c	1	1.05	7.2
3c	1	10	-
4	0.85	0.806	8.1

Table B.3: Old and new discharge coefficients used in CoolVent for the three-story office building with a 2 m x 3 m shaft.

Opening	Old C_d	New C_d	Idelchik Diagram
1a	0.65	1.40	3.1
2a	0.65	1.40	3.1
3a	0.65	1.40	3.1
1b	1	0.933	6.6
2b	1	0.416	7.4
3b	1	0.209	7.4
1c	1	0.532	7.2
2c	1	1.05	7.2
3c	1	10	-
4	0.85	0.639	8.1

Table B.4: Old and new discharge coefficients used in CoolVent for the three-story office building with a 2 m x 3.5 m shaft.

Opening	Old C_d	New C_d	Idelchik Diagram
1a	0.65	1.40	3.1
2a	0.65	1.40	3.1
3a	0.65	1.40	3.1
1b	1	0.990	6.6
2b	1	0.493	7.4
3b	1	0.245	7.4
1c	1	0.541	7.2
2c	1	1.06	7.2
3c	1	10	-
4	0.85	0.518	8.1

Table B.5: Old and new discharge coefficients used in CoolVent for both configurations of the single chimney.

Chimney	Opening	Old C_d	New C_d	Idelchik Diagram
2X2	1	0.65	1.40	3.1
2X2	2	1	1.20	6.6
2X2	3	1	10	–
2X2	4	0.85	1	8.1
2X4	1	0.65	1.40	3.1
2X4	2	1	1.24	6.6
2X4	3	1	10	–
2X4	4	0.85	0.35	8.1

Bibliography

[1] Buildings energy data book. http://buildingsdatabook.eren.doe.gov/.

[2] Energy information administration search : Us energy consumption sector. http://usasearch.gov/search?input-form=simple-firstgov&v%3Aproject=firstgov&query=us+energy+consumption+sector&affiliate=eia.doe.gov&x=0&y=0.

[3] SAI model 5 console. http://www.sageaction.com/MD5.htm.

[4] San francisco federal building | arup | a global firm of consulting engineers, designers, planners and project managers. http://www.arup.com/Projects/San_Francisco_Federal_Building.aspx.

[5] Soap bubbles - reveal internal flows in industrial plants. *New Scandinavian Technology*, 6:26–27, 1994.

[6] Ansys. *Fluent Users Manual*, 2011.

[7] ASHRAE. *Standard 55-2010: Thermal Environmental Conditions for Human Occupancy.* ASHRAE, Atlanta, GA.

[8] ASHRAE. *Standard 111-2008: Measurement, Testing, Adjusting, and Balancing of Building HVAC Systems.* ASHRAE, Atlanta, GA, 2008.

[9] H.B. Awbi. Air movement in naturally-ventilated buildings. Presentation at World Renewable Energy Congress in Denver, USA, June 1996.

[10] J Axley. Multizone airflow modeling in building: history and theory. *HVAC&R Research*, 13(6):907–28, 2007.

[11] V. Baturin. *Fundamentals of Industrial Ventilation.* Pergamon, Oxford, third edition, 1972.

[12] A. Blomsterberg and T. Johansson. Use of multi-zone air flow simulations to evaluate a hybrid ventilation system. In *Nin International IBPSA Conference, Montreal, Canada*, 2005.

[13] E. Buckingham. On physically similar systems; illustrations of the use of dimensional equations. *Physical Review*, 4(4):345–376, October 1914.

[14] Campbell Scientific. *AM25T Solid State Multiplexer Instruction Guide*, 1/10 edition, 2010.

[15] Campbell Scientific. *CR1000 Specifications*, 2011.

[16] G Carrilho da Graca, P. Linden, and M. Brook. Design of the natural ventilation system for the new san diego children's museum. Montreal, Canada, August 2005.

[17] T. Chenvidyakarn and A. Woods. Multiple steady states in stack ventilation. *Building and Environment*, 40(3):399–410, March 2005.

[18] Youngjun Cho, Hazim Awbi, and Taghi Karimipanah. Theoretical and experimental investigation of wall confluent jets ventilation and comparison with wall displacement ventilation. *Building and Environment*, 43(6):1091–1100, June 2008.

[19] Malcom Cook and Alan Short. Natural ventilation and low energy cooling of large, Non-Domestic buildings four case studies. *International Journal of Ventilation*, 3(4), 2005.

[20] Richard J. DeDear and Gail S. Brager. Developing an adaptive model of thermal comfort and preference. *ASHRAE Technical Data Bulletin*, 14(1):27–49, 1998.

[21] Wenting Ding, Yuji Hasemi, and Tokiyoshi Yamada. Natural ventilation performance of a double-skin faade with a solar chimney. *Energy and Buildings*, 37(4):411–418, April 2005.

[22] United States DOE, editor. *EnergyPlus Engineering Reference.* US Department of Energy, 2010.

[23] David Etheridge and Mats Sandberg. *Building Ventilation: Theory and Measurement.* John Wiley & Sons, 1996.

[24] Shaun Fitzgerald and Andrew Woods. The influence of stacks on flow patterns and stratification associated with natural ventilation. *Building and*, 43(10):1719–1733, October 2008.

[25] Flex-Core. *AVT 150CX5 AC Voltage Transducer Specifications*, 2011.

[26] Fluke. *Multimeter 115 Users Manual*, 01 edition, 2006.

[27] J. Furbringer, C.-A. Roulet, and R. Borchellini. Evaluation of comis. Technical report, Annex 23, 1996.

[28] Guohui Gan and Saffa B. Riffat. CFD modelling of air flow and thermal performance of an atrium integrated with photovoltaics. *Building and Environment*, 39(7):735–748, July 2004.

[29] Graywolf Sensing Solutions. *AdvancedSense Product Specifications*, 2011.

[30] P. Haves, P. F. Linden, and G. Carrilho Da Graca. Use of simulation in the design of a large, naturally ventilated office building. *Building Services Engineering Research & Technology*, 25(3):211–221, 2004.

[31] Shafqat Hussain, Patrick H. Oosthuizen, and Abdulrahim Kalendar. Evaluation of various turbulence models for the prediction of the airflow and temperature distributions in atria. *Energy and Buildings*, 48(0):18–28, May 2011.

[32] I.E. Idelchik. *Handbook of Hydraulic Resistance.* Jaico Publishing House, Mumbai, 3 edition, 2001.

[33] Chris J. Koinakis. Combined thermal and natural ventilation modeling for long-term energy assessment: validation with experimental measurements. *Energy and Buildings*, 37(4):311–323, April 2005.

[34] X. Wang G. Riskowski L. Christianson L. Zhao, Y. Zhang. Measurement of airflow patterns in ventilated spaces using particle image velocimetry. Number 994156. ASAE Annual International Meeting, 1999.

[35] Abdelaziz Laouadi and Morad R. Atif. Comparison between computed and field measured thermal parameters in an atrium building. *Building and Environment*, 34(2):129–138, March 1998.

[36] Pei-Chun Liu, Hsien-Te Lin, and Jung-Hua Chou. Evaluation of buoyancy-driven ventilation in atrium buildings using computational fluid dynamics and reduced-scale air model. *Building and Environment*, 44(9):1970–1979, September 2009.

[37] Zhiwen Luo, Jianing Zhao, Jun Gao, and Lixia He. Estimating natural-ventilation potential considering both thermal comfort and iaq issues. *Building and Environment*, 42:2289–2298, 2007.

[38] M.-A. Menchaca-Brandan and L. Glicksman. Coolvent: A multizone airflow and thermal analysis simulator for natural ventilation in buildings. In *Simbuild 2008 IBPSA-USA National Conference*, 2008.

[39] Maria-Alejandra Menchaca-Brandan, Leon R Glicksman, and Fukuda Masa. The importance of accounting for radiative heat transfer in room airflow simulations. In *Roomvent 2011*, Trondheim, Norway, 2011.

[40] Maria-Alejandra Menchaca-Brandan, Stephen Ray, and Leon R Glicksman. Design of practical hybrid ventilation building in central Tokyo. In *ASHRAE 2012 Winter Conference*, Chicago, USA, 2012.

[41] E Mouriki. *Solar-assisted hybrid ventilation in an institutional building.* M. sc., Concordia University, Montreal, 2009.

[42] National Semiconductor. *Temperature Sensor LM35CZ Product Information*, 2011.

[43] need to fill. Technical report, HULIC, 2009.

[44] Peter Nielsen. Airflow in a world exposition pavilion studied by scale-model experiments and computational fluid dynamics. *ASHRAE Transactions: Symposia*, 101:1118–1126, 1995.

[45] OMEGA. *OMEGA Thermocouple Product Guide*, 2012.

[46] Chen Qingyan. Ventilation performance prediction for buildings: A method overview and recent applications. *Building and Environment*, 44(4):848–858, April 2009.

[47] Stephen Ray, Leon R Glicksman, and Fukuda Masa. Case study of hybrid ventilation system with exhaust shafts. In *Roomvent 2011*, Trondheim, Norway, 2011.

[48] Lobutova-E. Rank R. Mller D. Putze T. Resagk, C. and H.-G. Maas. Measurement of large-scale flow structures in air using a novel 3d particle tracking velocimetry technique. Lisbon, Portugal, 2006. 13th Int. Symp. On Appl. Laser Techniques to Fluid Mechanics.

[49] M. Rolloos. Possibilities and limitations for the prediction of air flow patterns, temperatures, and velocities in large halls using scale models, heat exchangers, air conditioning. Technical report, Refrigeration Science and Technology International Institute of Refrigeration. Yugoslavia, 1977.

[50] P.G. Rousseau and E.H. Mathews. A new integrated design tool for naturally ventilated buildings. *Energy and Buildings*, 23:231–236, 1996.

[51] David Rowe. Pilot study report: Wilkinson building the university of sydney, sydney, australia. Technical report, University of Sydney, 2002.

[52] C.A. Rundle, M.F. Lightstone, P. Oosthuizen, P. Karava, and E. Mouriki. Validation of computational fluid dynamics simulations for atria geometries. *Building and Environment*, 46(7):1343–1353, July 2011.

[53] C Alan Short. Exploiting a hybrid environmental design strategy in a US continental climate. *Building research and information*, 35(2):119–143, 2007.

[54] MW Simons and BJ Moloney. Comfort and acoustic monitoring in a large naturally ventilated technically advanced building. *International Journal of Ventilation*, 2(1):1–14, 2003.

[55] L.M. Staley. The use of zero buoyancy bubbles to measure air flow in swine buildings. Number 811-209, Ontario, Canada, 1981. 61st Annual AIC Conference.

[56] Y. Sun and Y. Zhang. Development of a stereoscopic particle image velocimetry system for full-scale room airflow studies, part ii: Experimental setup. *ASHRAE Transactions*, 109, 2003.

[57] Y Takemasa, M Hiraoka, and H Tsukamoto. Application of an Unsteady-State model for predicting vertical temperature distribution to an existing atrium. *ASHRAE Transactions*, 102(1), 1996.

[58] Yuichi Takemasa, Masaya Hiraoka, Masahiro Katoh, Katsuhiro Miura, Shinji Kasai, and Tsuyoshi Oya. Natural ventilation with dynamic facades. *International Journal of Ventilation*, 8:287–298, 2009.

[59] Per Olaf Tjelflaat. Pilot study report: Media school grong, norway. Technical report, Norwegian University of Science and Technology, 2000.

[60] Ashley K Turza. Dense, low-power environmental montiroing for smart energy profiling. Master's thesis, Massachusetts Institute of Technology, 2010.

[61] Christine Walker. *Methodology for the Evaluation of Natural Ventilation in Buildings Using a Reduced-Scale Air Model.* PhD thesis, Massachusetts Institute of Technology, 2006.

[62] Christine Walker, Gang Tan, and Leon Glicksman. Reduced-scale building model and numerical investigations to buoyancy-driven natural ventilation. *Energy and Buildings*, 43(9):2404–2413, September 2011.

[63] George Walton and W. Stuart Dols. Contam user guide and program documentation. Technical Report NISTIR7251, NIST, 2010.

[64] F.M. White. *Fluid Mechanics.* The McGraw-Hill Companies, 1999.

[65] Nyuk Hien Wong and Sani Heryanto. The study of active stack effect to enhance natural ventilation using wind tunnel and computational fluid dynamics (CFD) simulations. *Energy and Buildings*, 36(7):668–678, July 2004.

[66] Runming Yao, Baizhan Li, Koen Steemers, and Alan Short. Assessing the natural ventilation cooling potential of office buildings in different climate zones in china. *Renewable Energy*, 34(12):2697–2705, December 2009.

[67] Jinchao Yuan. *Transition Dynamics between the Multiple Steady States in Natural Ventilation Systems: From Theories to Application in Optimal Controls.* PhD thesis, Massachusetts Institute of Technology, 2007.

[68] John Zhai, Moncef Krarti, and Mary-Hall Johnson. Assess and implement natural and hybrid ventilation models in Whole-Building energy simulations. Technical Report TRP-1456, University of Colorado at Boulder, September 2009.